UNIVERSITÀ DEGLI STUDI DI PADOVA

Dipartimento di Ingegneria Civile, Edile e Ambientale

Department Of Civil, Environmental and Architectural Engineering

Master's degree in Mathematical Engineering

Master's thesis

Numerical Analysis of the Aortic Root Anatomy based on the Topology Optimization approach

Supervisor: Prof. Paolo Peruzzo

Co-supervisor: Chiar.mo Prof. Stefano Lanzoni

Student: Gianmarco Boscolo 2029060

Academic year 2022/2023

Contents

List of Figures

List of Tables

Chapter 1

Introduction

The aortic root anatomy and physiology role are widely developed topics in the biomechanics literature [1, 2, 3, 4, 5, 6, 7]. Despite that, the hemodynamics within the Valsalva sinuses and the function of their epicycloidal shape are still not completely understood.

Studied firstly by Leonardo Da Vinci (1512-13), arriving to nowadays *in-vivo* 4D-MRI studies [8], its flow's vortical structure has been supposed to play a fundamental role in the aortic valve closure dynamics. Nonetheless, the aortic root design demonstrated to be crucial in preventing severe health problems as the valve stenosis or regurgitation, being the "anatomical bridge between the left ventricle and the acending aorta" [5].

The aortic root anatomy consists of the aortic valve, made up by three leaflets and three aortic sinuses, which are three bulges originating from the leaflets hingelines (see Figure 1.1).

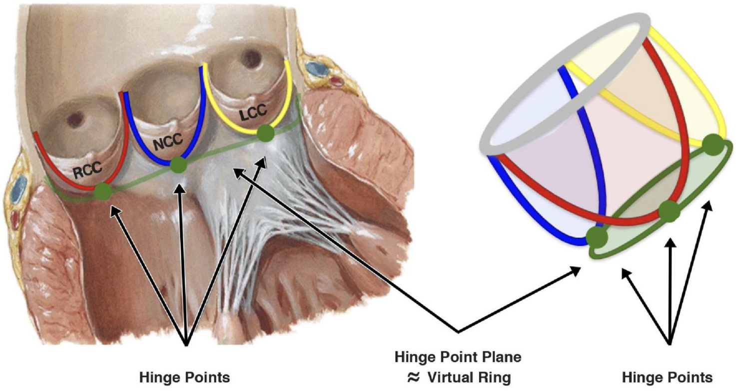

Figure 1.1: Aortic Root Anatomy Description. Image from [9].

Developing from the *ventriculo-arterial* to the *sino-tubular* junction, the aortic root forms a functional district of perfect complexity, which can withstand pressure differences up to 100 mmHg during the diastole, i.e., when the aortic valve is closed [1]. The most popular hypothesis regarding the role played by the sinuses is to be part of a "fluid control mechanism" that prevents the aortic cusps to touch the aortic walls and traps the vortices, which facilitate the valve closure reducing the reverse flow time.

Nonetheless, *Fukui et al.* showed the presence of multiple vortices in each sinus in recent numerical simulations [10]. These vortices change shape and intensity by varying the aortic root morphology, and thus suggesting that the natural configuration could also play an active role in the sistolic phase, i.e., the phase of flow ejection through the aortic valve. This hypothesis seems to be confirmed in a recent study by Toninato et al. [6], where measurements over different surgical configurations of aortic valve implantation highlighted that the physiological configuration is associate with the minimum energy loss over the entyre cardiac cycle. However a physically-based explanation of the role of the Valsalva sinuses is still elusive. To cover this bridge of knowledge we want to apply the Topology Optimization approach to investigate the possible natural criteria leading to the formation of the aortic sinuses (see Figure 1.2).

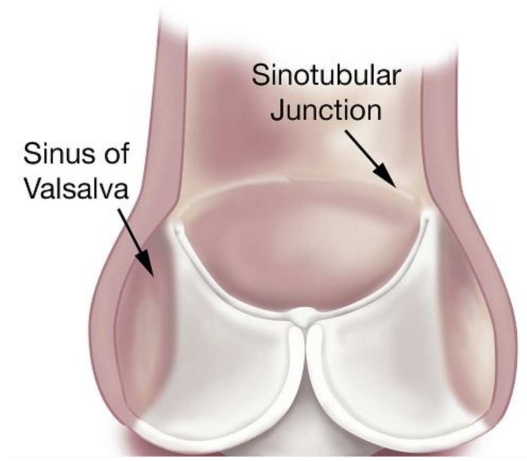

(a) Image from [11]

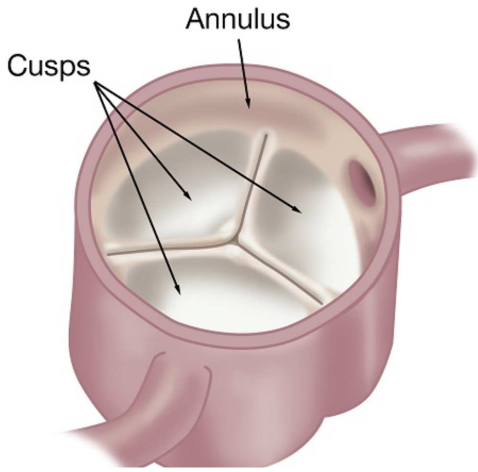

(b) Image from [11]

(c)

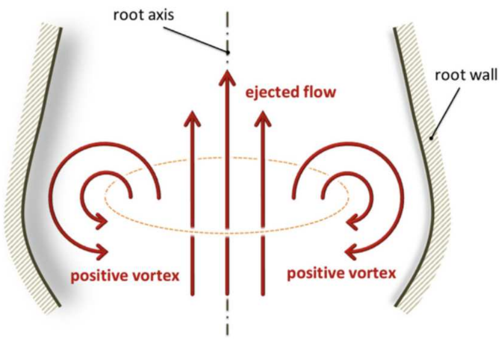

(d) Image from [6]

Figure 1.2: Aortic Sinuses Overview. a) sinuses of Valsalva; b) annulus and valvular cusps; c) aortic root model geometry; d) aortic root vortices scheme.

The topology optimization is widely used in several engineering fields, allowing the design of optimal domain structures, disregarding any topological classification of the initial condition [12]. The optimization procedure has the goal of minimizing/maximizing a given functional that constrains the variables of the mathematical model associated to the considered phenomena. In this work, we adopt the density method approach, which considers the domain a porous material whose porosity can locally change. In fluid dynamics simulation, this leads to the formation of preferential flow paths of high permeability (see for more details, the seminal works of Bendsøe and Sigmund in [13], [14]).

The mathematical technique to solve this kind of problems requires the use of advanced formulations and tools, such as the solutions of the Navier-Stokes's adjoint PDEs, as treated by Hinze et al. [15].

The topology optimization development lays its foundations on the works of Sigmund and Bendsøe [12], and Deng et al. [16]. Moreover, the bibliographic research on the state of the art relies on the works of Dbouk [17] and Alexander et al. [18].

The present objective functional formulation is based on the minimization of the energy dissipation, which depends on the strain rate tensor and the material permeability effect.

Since some authors argued that eddies within the sinuses have a pivotal role in the aortic valve dynamics, for the first time, also the vorticity has been take into account in a 3D model topology optimization study.

In order to investigate on the optimality conditions leading to the aortic root shape, some preliminary case studies have been developed. The purpose is carried out a sensitivity analysis to tune the optimization parameters, the functional weights, and to analyze the inertia effects on the final aortic root shape.

Finally, a series of multi-scenarios analysis has been performed, with the idea to critically discuss the results and identify the criteria leading Nature to promote the actual shape of the Valsalva sinuses.

Chapter 2

Topology Optimization

The optimal distribution of resources has always played a critical role dealing with real world problems. This is why, since its first development by Bendsøe in 1988 [19], layout optimization has become a widely popular approach to study and solve engineering problems (see the review studies [14] and [20].

Three approaches belong to the family of layout optimization, namely, the size, shape, and topology optimization (see Figure 2.1). The purpose of the size optimization is to find the best value of the geometrical parameters describing a given structure or domain. The shape optimization goal is to find the optimal shape of a given topological structure. In the topology optimization method, instead, the topological structure is free to change during the optimization procedure, i.e., the number of holes in the domain structure can be different from the initial one. Therefore, this method has the advantage to weakly depend on the initial guessed conditions.

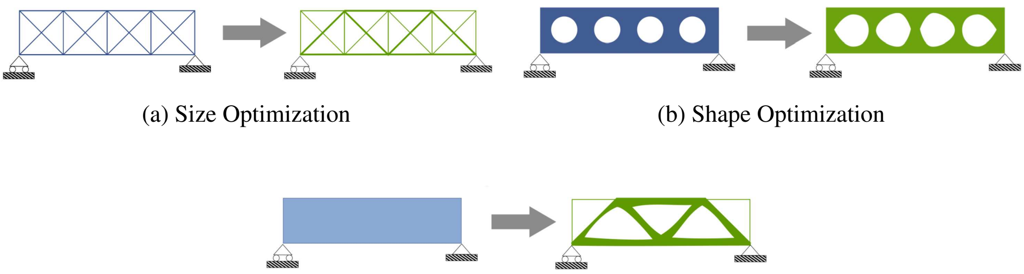

(a) Size Optimization

(b) Shape Optimization

(c) Topology Optimization

Figure 2.1: Size,Shape and Topology Optimization. Image from [21].

The topology optimization lays its foundations in the field of solid mechanics and it was developed in order to deal with material distribution problems. However, its fundamental methodology has demonstrated to be suitable to treat any kind of partial differential equations governing a mathematical model. This is the reason why, since the 2000s, it has been applied to a broad number of physics problems. Among those, pure fluid dynamics or coupled problems, as the heat transfer or the optimal transport problems, are the most challenging processes to face with. Indeed, when fluid dynamics is the main driver of the considered physics *"the optimization problem becomes a question of where to enforce relevant boundary conditions for the fluid problem"* [18].

The most used optimization approaches are the evolutionary techniques, the density method, and the level set method (see Figure 2.2). The evolutionary techniques are heuristic-based methods suitable to solve problems that are too hard to be solved using direct theoretical methods, i.e., whose computational complexity is more than polynomial. The density method selects the path where the fluid should flow, simulating the presence of a porous media by introducing a fictitious forcing in the governing equations. The level-set method, instead, finds the optimal configuration propagating a given initial interface, i.e., a level set.

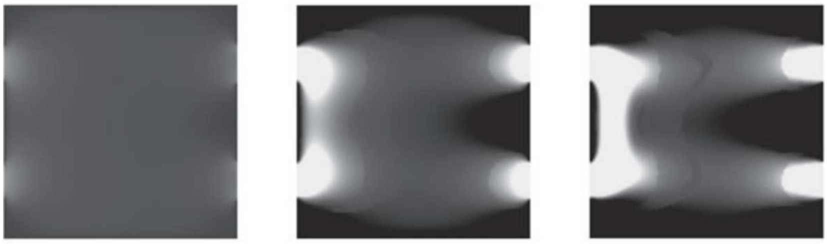

(a) Density Method

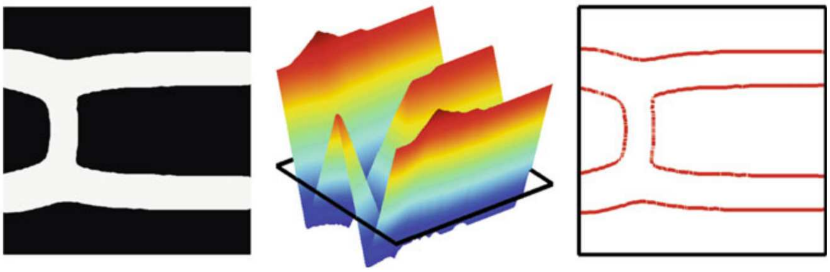

(b) Level set Method

Figure 2.2: Comparison between the Density and Level set methods. Images from [16]

Finally, according to the preferred discretization strategy in the literature, the Finite Element Method (FEM) has been chosen to solve the PDE systems. The FEM has indeed the advantage to adopt linear shape functions, which can be easily used to approximate the parameters that define the optimal design. [16], [17], [18].

2.1 Problem Formulation

2.1.1 Problem Definition

The general topology optimization problem can be formulated as a continuous-constrained non-linear problem that reads:

$$\begin{cases} \min\limits_{h,\gamma} J(h,\gamma) & \\ \text{subject to:} & \int_\Omega \gamma(\mathbf{x}) d\Omega - \beta|\Omega| \leq 0, \\ & 0 \leq \gamma(\mathbf{x}) \leq 1, \\ & \text{Governing PDEs.} \end{cases} \tag{2.1}$$

Using the standard notation for optimization problems, J is the objective functional, γ and h are the decision variables, and the equalities or inequalities they must satisfy are the constraints. The volume constraint is an operational bound, which permits the fluid to occupy no more than a prescribed fraction of the domain. This further requirement is needed to prevent the achievement of trivial solutions.

The theoretical design optimization problem is based on a discrete formulation, with $\gamma \in \{0, 1\}$; however, the fastest algorithms adopts a continuous formulation, such as the Method of Moving Asymptotes (MMA) [22] and the Generalized Optimality Criteria (GOC) [23]. In these methods, the functional is assumed convex and is minimized through the gradient analysis with respect to the design variable that define the functional itself.

Therefore, γ is considered a piece-wised linear continuous function in the space, which interpolate the nodal values with the same shape functions used to solve the velocity field in the FEM.

The physics is governed by the classical incompressible and time-dependent Navier-Stokes equations, with Dirichlet and Neumann boundary conditions, i.e.,

$$\begin{cases} \rho\partial_t\mathbf{u} - \nabla\cdot(\mu\nabla\mathbf{u}) + \rho(\mathbf{u}\cdot\nabla)\mathbf{u} + \nabla p = \mathbf{f} & in\ [0,T]\times\Omega \\ \nabla\cdot\mathbf{u} = 0 & in\ [0,T]\times\Omega \\ \mathbf{u} = \mathbf{u}_D, & on[0,T]\times\Gamma_D \\ \mathbf{u}|_{t=0} = \mathbf{u}_0, \qquad p = p_0 & in\ \Omega \\ \Big(p\mathbb{I} - \mu\nabla\mathbf{u}\Big)\cdot\mathbf{n} = \mathbf{g}, & on\ [0,T]\times\Gamma_N. \end{cases} \tag{2.2}$$

where Ω is the fluid domain, $\partial\Omega = \Gamma_D \cup \Gamma_N$ is the boundary, with Γ_D and Γ_N the edges where the Dirichlet and Neumann conditions are applied respectively. In (2.2), $\mathbf{u}$ is the velocity field, p is the pressure, ρ is the fluid density, μ is the fluid dynamic viscosity, $\mathbf{f}$ is the forcing, $\mathbf{u}_D$ is the prescribed value of the velocity at the boundary, $\mathbf{u}_0$ and p_0 are the velocity and pressure initial values, $\mathbf{n}$ is the normal outward direct unit vector, and g is the prescribed flux at the boundary. The general optimization problem can be rewritten substituting (2.2) into (2.1).

2.1.2 The Density Method

For the purposes of this work, it is required a technique with a solid theoretical background, with the ability to change the design sensitivities throughout the domain. In this frame, the density method represents the best alternative [12], [16]. In force of that, a design variable, γ, has been introduced to describe the domain regions in which the fluid flow can or can not pass. The role of γ is taken into account introducing a friction force, $\mathbf{f}_\alpha$, owing to the presence of a porous media and proportional to the fluid velocity, $\mathbf{u}$.
The additional forcing term into the NS-equations reads as:

$$\mathbf{f}_\alpha = -\alpha\mathbf{u}, \qquad \text{with } \alpha(\mathbf{x}) = \frac{\mu}{k(\mathbf{x})}. \tag{2.3}$$

Here, $k(\mathbf{x})$ is the local permeability of the medium at the position $\mathbf{x} \in \Omega$. For practical purposes α is defined in order to depend only on the design variable, γ, and a tuning parameter, q, according to the following relationship:

$$\alpha(\gamma) = \alpha_q(\gamma) := \alpha_{min} + (\alpha_{max} - \alpha_{min})\frac{q\gamma}{q + 1 - \gamma} \tag{2.4}$$

where α_{min} and α_{max} are the boundary values for α. An ideal impermeable wall would then correspond to $\alpha \to \infty$. However, for a good numerical analysis it is sufficient to set α_{max} large enough to determine a velocity $\mathbf{u}$ negligibly small. While this approximation has minor effects on the global optimization procedure, locally unwanted streamlines can be detected within the supposed impermeable domain in the visualization of the results.

Introducing the above definition for the forcing term, the incompressible Navier-Stokes equations can be written as:

$$\begin{cases} \rho\partial_t \mathbf{u} - \nabla\cdot(\mu\nabla\mathbf{u}) + \rho(\mathbf{u}\cdot\nabla)\mathbf{u} + \nabla p = \tilde{\mathbf{f}} & in\ [0,T]\times\Omega \\ \nabla\cdot\mathbf{u} = 0 & in\ [0,T]\times\Omega \\ \mathbf{u} = \mathbf{u}_D, & on[0,T]\times\Gamma_D \\ \mathbf{u}|_{t=0} = \mathbf{u}_0 & in\ \Omega \\ \Big(p\mathbb{I} - \mu\nabla\mathbf{u}\Big)\cdot\mathbf{n} = \mathbf{g}, & on\ [0,T]\times\Gamma_N. \end{cases} \tag{2.5}$$

with

$$\tilde{\mathbf{f}} := \mathbf{f}_\alpha + \mathbf{f}. \tag{2.6}$$

By (2.5), it is easy to see that, for a given value of γ, the solution of the governing equations, i.e., the field of $\mathbf{u}$ and p, is uniquely defined. Accordingly, the pair $(\mathbf{u}, p)$ turns out to be implicit functions of the design variable: $(\mathbf{u}_\gamma, p_\gamma)$.

Finally, performing the sensitivity analysis of J with respect to γ, i.e., $dJ/d\gamma$, leads to:

$$\frac{d}{d\gamma}J(\mathbf{u}_\gamma, p_\gamma, \gamma) = \frac{\partial J}{\partial \gamma} + \frac{\partial J}{\partial \mathbf{u}} \cdot \frac{\partial \mathbf{u}}{\partial \gamma} + \frac{\partial J}{\partial p} \cdot \frac{\partial p}{\partial \gamma}. \tag{2.7}$$

Since $\mathbf{u}_\gamma$ and p_γ are implicit, the direct evaluation of their derivatives, $\partial \mathbf{u}/\partial \gamma$ and $\partial p/\partial \gamma$, is not trivial. To deal with this drawback, Hinze et al. proposed a theoretical formulation [15], then applied by Deng et al. [16], with the adoption of the so-called *adjoint variables method*, to substitute the unknown derivatives in (2.7). As it will be developed with more details in section 2.2, this strategy requires the computation of the adjoint variables of $\mathbf{u}$ and p, relatively to the optimization problem (2.1).

2.1.3 Optimization Algorithm

The optimization problem algorithm can now be formulated as in [12] and [16]:

1. Choose an initial value for γ;
2. Solve the governing equations (2.2) for $\mathbf{u}$ and p with a FEM algorithm;
3. (a) Compute derivative of the objective functional and the constraints with respect to gamma;

   (b) Solve the adjoint problem of (2.5) to substitute the partial derivatives of the implicit dependencies from the formulation;

   (c) Compute the gradient of the objective functional;

4. Use a continuous optimization method (MMA or GOC) to update γ's value minimizing J, based on the past iterations history and the gradient analysis;

5. Check γ convergence.

   If converged, end the process, otherwise restart from step 2.

The most computational-cost step of the algorithm is the solution of the governing equations. In fact, at every iteration, a system of non-linear partial differential equations must be solved.

2.2 Adjoint System

Since the finite element method works with the weak formulation of the considered PDEs and the solution of the NS equations (2.2) is uniquely determined by the knowledge of γ, the optimization problem (2.1) becomes:

$$\begin{cases} \min\limits_{\gamma} J(u, p, \gamma) & \\ \text{subject to:} & \int_{\Omega} \gamma(\mathbf{x}) d\Omega - \beta|\Omega| \leq 0, \\ & 0 \leq \gamma(\mathbf{x}) \leq 1, \\ & e(\mathbf{u}, p; \gamma) = 0; \end{cases} \tag{2.8}$$

with $e(\mathbf{u}, p; \gamma)$ the weak operator of the NS PDEs as formulated in (2.5). Furthermore, accordingly to the general formulation in [16] and [24], the objective functional, J, is defined as the sum of a volume and boundary integral terms, respectively $A(\mathbf{u}, \nabla\mathbf{u}, p; \gamma)$ and $B(\mathbf{u}, p; \gamma)$, i.e.,:

$$\begin{aligned} J(\mathbf{u}, p; \gamma) = & \int_0^T \int_{\Omega} A(\mathbf{u}, \nabla\mathbf{u}, p; \gamma)) d\Omega dt \\ & + \int_0^T \int_{\partial\Omega} B(\mathbf{u}, p; \gamma) d\Gamma dt \end{aligned} \tag{2.9}$$

2.2.1 The Navier-Stokes weak formulation

To develop some notes on the adjoint optimization theory, it is necessary to define the weak formulation of the NS equations. For now on the solution of the NS weak formulation will be assumed such that $(\mathbf{u}, p) \in \mathcal{U}_{\Gamma_D} \times \mathcal{Q}$, with

$$\begin{aligned} \mathcal{U}_{\Gamma_D} &= \left(\mathscr{L}^2([0,T]) \times \mathscr{H}^1_{\Gamma_D}(\Omega)\right)^d \\ \mathcal{Q} &= \mathscr{L}^2([0,T]) \times \mathscr{L}^2(\Omega), \end{aligned} \tag{2.10}$$

as discussed in [25], where

$$\mathscr{H}^1_{\Gamma_D}(\Omega) \coloneqq \{v \in H^1(\Omega) \mid v = 0 \; in \; \Gamma_D \subseteq \partial\Omega.\}$$

Multiplying by test functions $v \in \mathcal{V}$ and $q \in \mathcal{Q}$, the integration over Ω by also applying the Gauss theorem yields to the classical weak forms for the momentum equation, i.e.,

$$\begin{aligned} &\int_0^T \int_\Omega \rho(\partial_t \mathbf{u}) \cdot \mathbf{v} d\Omega dt + \int_0^T \int_\Omega \mu \nabla \mathbf{u} : \nabla \mathbf{v} d\Omega dt + \int_0^T \int_\Omega \rho(\mathbf{u} \cdot \nabla \mathbf{u}) \cdot \mathbf{v} d\Omega dt \\ &- \int_0^T \int_\Omega p \nabla \cdot \mathbf{v} d\Omega dt = \int_0^T \int_\Omega \tilde{\mathbf{f}} \cdot \mathbf{v} d\Omega dt + \int_0^T \int_{\Gamma_N} \mathbf{g} \cdot \mathbf{v} d\Gamma dt \end{aligned} \tag{2.11}$$

while the continuity equation reads

$$\int_0^T \int_\Omega q \nabla \cdot \mathbf{u} dt = 0 \tag{2.12}$$

$\forall \mathbf{v} \in \mathcal{U}_{\Gamma_D}$ and $\forall q \in \mathcal{Q}$.

The Dirichlet boundary conditions are implicitly assumed in the above weak formulation and they will be imposed applying the lifting function technique directly in the linear system. Using the linear operators notation, equations (2.11)–(2.12) read as

$$
\begin{aligned}
(\rho\partial_t \mathbf{u}, \mathbf{v}) + n(\mathbf{u}, \mathbf{u}, \mathbf{v}) + a(\mathbf{u}, \mathbf{v}) + b(\mathbf{v}, p) = \tilde{F}(\mathbf{v}) + G(\mathbf{v}) \quad \forall \mathbf{v} \in \mathcal{V}, \\
b(\mathbf{u}, q) = 0 \quad \forall q \in \mathcal{Q},
\end{aligned}
$$

with

$$
\begin{aligned}
(\mathbf{v}, \mathbf{w}) &:= \int_\Omega \mathbf{v} \cdot \mathbf{w} d\Omega & n(\mathbf{v}, \mathbf{w}, \mathbf{z}) &:= \int_\Omega \rho(\mathbf{v} \cdot \nabla \mathbf{w}) \cdot \mathbf{z} d\Omega \\
a(\mathbf{v}, \mathbf{w}) &:= \mu \int_\Omega \nabla \mathbf{v} : \nabla \mathbf{w} d\Omega & b(\mathbf{v}, q) &:= -\int_\Omega q \nabla \cdot \mathbf{v} d\Omega \\
\tilde{F}(\mathbf{v}) &:= \int_\Omega \tilde{\mathbf{f}} \cdot \mathbf{v} d\Omega & G(\mathbf{v}) &:= \int_{\Gamma_N} \mathbf{g} \cdot \mathbf{v} d\Gamma.
\end{aligned}
$$

Therefore, the residual operator for the NS-equations can be defined, as:

$$
\begin{aligned}
e(\mathbf{u}, p; \gamma) := (\rho\partial_t \mathbf{u}, \mathbf{v}) + n(\mathbf{u}, \mathbf{u}, \mathbf{v}) + a(\mathbf{u}, \mathbf{v}) + b(\mathbf{v}, p) + \\
- b(\mathbf{u}, q) - \tilde{F}(\mathbf{v}) - G(\mathbf{v}),
\end{aligned}
\tag{2.13}
$$

where the weak formulations for the momentum and continuity equations are added together.

Moreover, to deal with the non-linear convective term implementation, a Picard iterative approach has been developed, as described in [25] and [26]. For more details, see Appendix A.

2.2.2 Adjoint System Formulation

Thanks to the results of Zowe [27], on assuming the Robinson's regularity condition [28], Hinze et al. derived the corresponding of the Karush-Kuhn-Tacker (K.K.T.) conditions for PDE constrained optimal control problems [15], which results

$$
\begin{gathered}
e(\mathbf{u}, p; \gamma) = 0 \\
\begin{pmatrix} \big(e^*_{\mathbf{u}}(\mathbf{u}, p; \gamma)\big) & 0 \\ 0 & \big(e^*_p(\mathbf{u}, p; \gamma)\big) \end{pmatrix} \begin{pmatrix} \mathbf{u}_a \\ p_a \end{pmatrix} = \begin{pmatrix} -J_{\mathbf{u}}(\mathbf{u}, p; \gamma) \\ -J_p(\mathbf{u}, p; \gamma) \end{pmatrix} \\
\big(e^*_\gamma(\mathbf{u}, p; \gamma)\big)(\mathbf{u}_a, p_a) + J_\gamma(\mathbf{u}, p; \gamma) = 0.
\end{gathered}
\tag{2.14}
$$

where $\mathbf{u}_a$ and p_a are, respectively, the adjoint variable for $\mathbf{u}$ and p, and $e^*(\cdot)$ is the adjoint (dual) operator of $e(\cdot)$. For more details, see Appendix B.

Furthermore, the above formulation works under the following regularity assumptions:

1. The functional $J(\mathbf{u}, p, \gamma)$ is convex.

2. The functional J is Fréchet-differentiable.

3. The function spaces for the variables are:

$$
\begin{aligned}
&\mathbf{u}, \mathbf{w} \in \mathcal{U}_{\Gamma_D};\\
&\mathbf{u}_a, \mathbf{v} \in \mathcal{U} := \Big(\mathscr{L}^2(0,T) \times \mathscr{H}^1(\Omega)\Big)^d;\\
&p, p_a \in \mathcal{P} := \mathscr{L}^2(0,T) \times \mathscr{L}^2(\Omega)\\
&\tilde{\mathbf{f}} \in \mathcal{F} := \Big(\mathscr{L}^2(0,T) \times \mathscr{H}^1(\Omega)\Big)^d;\\
&\mathbf{g} \in \mathcal{G}_{\Gamma_N} := \Big(\mathscr{L}^2(0,T) \times \mathscr{L}^2(\Gamma_N)\Big)^d;\\
&\mathbf{u}_0 \in \big(\mathscr{H}^1_{\Gamma_D}(\Omega)\big)^d;\\
&\mathbf{u}_D \in \big(\mathscr{H}^1(\Gamma_D)\big)^d;\\
&\gamma \in \mathscr{L}^2(\Omega).
\end{aligned}
\tag{2.15}
$$

As a consequence, the integration over time and space can be switched as described by Zeidler [29], and $e(\mathbf{u}, p, \gamma)$ can be expressed as follows:

$$
\begin{aligned}
e(\mathbf{u}, p; \gamma) = &\int_\Omega \int_0^T \rho \Big[\frac{\partial(\mathbf{u}\cdot\mathbf{v})}{\partial t} - \mathbf{u}\cdot\frac{\partial \mathbf{v}}{\partial t}\Big] dt d\Omega +\\
&+ \mu \int_0^T \int_\Omega \Big[\nabla\mathbf{u} : \nabla\mathbf{v} - \nabla\cdot\big(\nabla\mathbf{u}\cdot\mathbf{v}\big)\Big] d\Omega dt +\\
&+ \int_0^T \int_\Omega \rho\big(\mathbf{u}\cdot\nabla\big)\mathbf{u}\cdot\mathbf{v} d\Omega dt + \int_0^T \int_\Omega \big[\nabla\cdot(p\mathbf{v}) - p\nabla\cdot\mathbf{v}\big] d\Omega dt +\\
&- \int_0^T \int_\Omega q\nabla\cdot\mathbf{u} d\Omega dt - \int_0^T \int_\Omega \tilde{\mathbf{f}}\cdot\mathbf{v} d\Omega dt\\
&+ \int_\Omega (\mathbf{u} - \mathbf{u}_0)|_{t=0}\cdot\mathbf{v} d\Omega.
\end{aligned}
$$

The latter expression, according to the Gauss theory in [15], reduces to

$$
\begin{aligned}
e(\mathbf{u},p;\gamma) = &\int_\Omega \rho(\mathbf{u}\cdot\mathbf{v})|_{t=T} d\Omega - \int_0^T\int_\Omega \rho\mathbf{u}\cdot\frac{\partial \mathbf{v}}{\partial t} d\Omega dt + \\
&+ \mu\int_0^T\int_\Omega \nabla\mathbf{u} : \nabla\mathbf{v} d\Omega dt + \int_0^T\int_\Omega \rho\big(\mathbf{u}\cdot\nabla\big)\mathbf{u}\cdot\mathbf{v} d\Omega dt + \\
&- \int_0^T\int_\Omega p\nabla\cdot\mathbf{v} d\Omega dt - \int_0^T\int_\Omega \tilde{\mathbf{f}}\cdot\mathbf{v} d\Omega dt - \int_0^T\int_{\Gamma_N} \mathbf{g}\cdot\mathbf{v} d\Gamma dt + \\
&- \int_0^T\int_\Omega q\nabla\cdot\mathbf{u} d\Omega dt + \int_0^T\int_{\Gamma_D}\Big(p\mathbb{I} - \mu\nabla\mathbf{u}\Big)\mathbf{n}\cdot\mathbf{v} d\Gamma dt.
\end{aligned}
\tag{2.16}
$$

To develop the adjoint formulation of (2.1), subject to (2.2), the Gateaux derivatives of the functional J and the weak NS formulation (2.13) must be computed. In order to do so it must be observed that, both the functional and the NS weak operator are be Fréchet-differentiable [30]. Moreover, to be Fréchet-differentiable implies also the existence of the Gateux-derivative [15]. Therefore, the Gateaux-derivatives of J and $e(\mathbf{u},p,\gamma)$, along the direction $(\mathbf{w},r)\in\mathcal{U}_{\Gamma_D}\times\mathcal{P}$, are

$$
\begin{aligned}
\big\langle e_{\mathbf{u}}(\mathbf{u},p;\gamma),\mathbf{w}\big\rangle_{\mathcal{U}^*_{\Gamma_D},\mathcal{U}_{\Gamma_D}} &= \lim_{l\to 0^+}\frac{e(\mathbf{u}+l\mathbf{w},p)-e(\mathbf{u},p)}{l} = ... = \\
&= \int_\Omega \rho(\mathbf{w}\cdot\mathbf{v})|_{t=T} d\Omega - \int_0^T\int_\Omega \rho\mathbf{w}\cdot\frac{\partial\mathbf{v}}{\partial t} d\Omega dt + \\
&+ \mu\int_0^T\int_\Omega \nabla\mathbf{w} : \nabla\mathbf{v} d\Omega dt + \int_0^T\int_\Omega \rho\big(\mathbf{w}\cdot\nabla\big)\mathbf{u}\cdot\mathbf{v} d\Omega dt + \\
&+ \int_0^T\int_\Omega \rho\big(\mathbf{u}\cdot\nabla\big)\mathbf{w}\cdot\mathbf{v} d\Omega dt - \int_0^T\int_\Omega \frac{\partial\tilde{\mathbf{f}}}{\partial\mathbf{u}}\mathbf{w}\cdot\mathbf{v} d\Omega dt + \\
&- \int_0^T\int_\Omega q\nabla\cdot\mathbf{w} d\Omega dt,
\end{aligned}
$$

$$\left\langle e_p(\mathbf{u},p;\gamma),r\right\rangle_{\mathcal{P}^*,\mathcal{P}} = \lim_{l\to 0^+}\frac{e(\mathbf{u},p+lr)-e(\mathbf{u},p)}{l} = ... =$$
$$-\int_0^T\int_\Omega r\nabla\cdot\mathbf{v}d\Omega dt - \int_0^T\int_\Omega \frac{\partial\tilde{\mathbf{f}}}{\partial p}r\cdot\mathbf{v}d\Omega dt + \int_0^T\int_\Gamma r\mathbf{n}\cdot\mathbf{v}d\Gamma dt,$$

in which the integral terms over Γ_D is neglected it, being along the Dirichlet boundary, where $\mathbf{u}\equiv\mathbf{u}_D$. According to (2.14), substituting the adjoint variables

$$\mathbf{u}_a = \mathbf{v} \tag{2.17}$$

$$p_a = q \tag{2.18}$$

the dual operators of $e_{\mathbf{u}}(\cdot)$ and $e_p(\cdot)$ can be expressed as:

$$\begin{aligned}\left\langle e^*_{\mathbf{u}}(\mathbf{u}_a,p_a;\gamma),\mathbf{w}\right\rangle_{\mathcal{U}_{\Gamma_D}{}^*,\mathcal{U}_{\Gamma_D}} = &\int_\Omega\rho(\mathbf{w}\cdot\mathbf{u}_a)|_{t=T}d\Omega - \int_0^T\int_\Omega\rho\mathbf{w}\cdot\frac{\partial\mathbf{u}_a}{\partial t}d\Omega dt+\\ &+\mu\int_0^T\int_\Omega\nabla\mathbf{w}:\nabla\mathbf{u}_a d\Omega dt + \int_0^T\int_\Omega\rho\big(\mathbf{w}\cdot\nabla\big)\mathbf{u}\cdot\mathbf{u}_a d\Omega dt+\\ &+\int_0^T\int_\Omega\rho\big(\mathbf{u}\cdot\nabla\big)\mathbf{w}\cdot\mathbf{u}_a d\Omega dt - \int_0^T\int_\Omega\frac{\partial\tilde{\mathbf{f}}}{\partial\mathbf{u}}\mathbf{w}\cdot\mathbf{u}_a d\Omega dt+\\ &-\int_0^T\int_\Omega p_a\nabla\cdot\mathbf{w}d\Omega dt.\end{aligned}$$

$$\begin{aligned}\left\langle e^*_p(\mathbf{u}_a,p_a;\gamma),r\right\rangle_{\mathcal{P}^*,\mathcal{P}} = &-\int_0^T\int_\Omega r\nabla\cdot\mathbf{u}_a d\Omega dt+\\ &-\int_0^T\int_\Omega\frac{\partial\tilde{\mathbf{f}}}{\partial p}r\cdot\mathbf{u}_a d\Omega dt + \int_0^T\int_{\Gamma_D} r\mathbf{n}\cdot\mathbf{u}_a d\Gamma dt\end{aligned}$$

Applying the inverse Gauss theory and integrating by parts, yields

$$\int_0^T\int_\Omega\nabla\mathbf{w}:\nabla\mathbf{u}_a d\Omega dt = -\int_0^T\int_\Omega\Delta\mathbf{u}_a\cdot\mathbf{w}d\Omega dt+\int_0^T\int_{\Gamma_N}\nabla\mathbf{u}_a\mathbf{n}\cdot\mathbf{w}d\Gamma dt$$

and

$$\int_0^T \int_\Omega p_a \nabla \mathbf{w} d\Omega dt = -\int_0^T \int_\Omega \nabla p_a \cdot \mathbf{w} d\Omega dt + \int_0^T \int_{\Gamma_N} p_a \mathbf{n} \cdot \mathbf{w} d\Gamma dt$$

$$\begin{aligned}
&\int_0^T \int_\Omega \big(\mathbf{u} \cdot \nabla\big)\mathbf{w} \cdot \mathbf{u}_a d\Omega dt = \\
&= -\int_0^T \int_\Omega \big(\mathbf{u} \cdot \nabla\big)\mathbf{u}_a \cdot \mathbf{w} d\Omega dt + \int_0^T \int_\Omega \mathbf{u} \cdot \nabla(\mathbf{u}_a \cdot \mathbf{w}) d\Omega dt = \\
&= -\int_0^T \int_\Omega \big(\mathbf{u} \cdot \nabla\big)\mathbf{u}_a \cdot \mathbf{w} d\Omega dt + \\
&\quad + \int_0^T \int_\Omega \nabla \cdot \big(\mathbf{u}(\mathbf{u}_a \cdot \mathbf{w})\big) d\Omega dt - \int_0^T \int_\Omega \cancelto{0}{\nabla \cdot \mathbf{u}} (\mathbf{u}_a \cdot \mathbf{w}) d\Omega dt = \\
&= -\int_0^T \int_\Omega \big(\mathbf{u} \cdot \nabla\big)\mathbf{u}_a \cdot \mathbf{w} d\Omega dt + \int_0^T \int_{\Gamma_N} (\mathbf{u} \cdot \mathbf{n})\mathbf{u}_a \cdot \mathbf{w} d\Gamma dt.
\end{aligned}$$

At this point, the optimality conditions (2.14) must be applied.

Hence, the weak (Gateaux) derivatives of the objective functional must be performed:

$$\begin{aligned}
&\big\langle J_{\mathbf{u}}(\mathbf{u}, p; \gamma), \mathbf{w} \big\rangle_{\mathcal{U}_{\Gamma_D}{}^*, \mathcal{U}_{\Gamma_D}} = \lim_{l \to 0} \frac{J(\mathbf{u} + l\mathbf{w}, p; \gamma) - J(\mathbf{u}, p; \gamma)}{l} = \\
&= \lim_{l \to 0} \frac{\int_0^T \int_\Omega A(\mathbf{u} + l\mathbf{w}, \nabla(\mathbf{u} + l\mathbf{w}), p; \gamma) d\Omega dt - \int_0^T \int_\Omega A(\mathbf{u}, \nabla \mathbf{u}, p; \gamma) d\Omega dt}{l} + \\
&+ \lim_{l \to 0} \frac{\int_0^T \int_{\partial\Omega} B(\mathbf{u} + l\mathbf{w}, p; \gamma) d\Gamma dt - \int_0^T \int_{\partial\Omega} B(\mathbf{u}, p; \gamma) d\Gamma dt}{l}.
\end{aligned}$$

Since the integrals are independent of the limit variable, the integration order can be changed, leading to:

$$
\begin{aligned}
&\big\langle J_{\mathbf{u}}(\mathbf{u},p;\gamma),\mathbf{w}\big\rangle_{\mathcal{U}_{\Gamma_D}{}^*,\mathcal{U}_{\Gamma_D}} = \\
&\qquad \int_0^T\int_\Omega \lim_{l\to 0}\frac{A(\mathbf{u}+l\mathbf{w},\nabla(\mathbf{u}+l\mathbf{w}),p;\gamma)-A(\mathbf{u},\nabla\mathbf{u},p;\gamma)}{l}d\Omega dt+\\
&\qquad +\int_0^T\int_{\partial\Omega}\lim_{l\to 0}\frac{B(\mathbf{u}+l\mathbf{w},p;\gamma)-B(\mathbf{u},p;\gamma)}{l}d\Gamma dt,
\end{aligned}
$$

where the limit involving $A(\mathbf{u},\nabla\mathbf{u},p;\gamma)$ is

$$
\begin{aligned}
&\lim_{l\to 0}\frac{A(\mathbf{u}+l\mathbf{w},\nabla(\mathbf{u}+l\mathbf{w}),p;\gamma)-A(\mathbf{u},\nabla\mathbf{u},p;\gamma)}{l}=\\
&=\lim_{l\to 0}\frac{A(\mathbf{u}+l\mathbf{w},\nabla(\mathbf{u}+l\mathbf{w}),p;\gamma)-A(\mathbf{u}+l\mathbf{w},\nabla\mathbf{u},p;\gamma)}{l}+\\
&+\lim_{l\to 0}\frac{A(\mathbf{u}+l\mathbf{w},\nabla\mathbf{u},p;\gamma)-A(\mathbf{u},\nabla\mathbf{u},p;\gamma)}{l}=\\
&=\frac{\partial A}{\partial\mathbf{u}}\cdot\mathbf{w}+\frac{\partial A}{\partial\nabla\mathbf{u}}:\nabla\mathbf{w}.
\end{aligned}
$$

Therefore, all of the above yields to:

$$
\begin{aligned}
\big\langle J_{\mathbf{u}}(\mathbf{u},p;\gamma),\mathbf{w}\big\rangle_{\mathcal{U}_{\Gamma_D}{}^*,\mathcal{U}_{\Gamma_D}} &= \int_0^T\int_\Omega\Big[\frac{\partial A}{\partial\mathbf{u}}\cdot\mathbf{w}+\frac{\partial A}{\partial\nabla\mathbf{u}}:\nabla\mathbf{w}\Big]d\Omega dt+\\
&+\int_0^T\int_{\partial\Omega}\frac{\partial B}{\partial\mathbf{u}}\cdot\mathbf{w}d\Gamma dt
\end{aligned}
$$

that, integrating by parts as follows

$$
\begin{aligned}
\int_0^T\int_\Omega\Big(\frac{\partial A}{\partial\nabla\mathbf{u}}:\nabla\mathbf{w}\Big)d\Omega dt &= \int_0^T\int_\Omega\Big[\nabla\cdot\Big(\frac{\partial A}{\partial\nabla\mathbf{u}}\mathbf{w}\Big)-\Big(\nabla\cdot\frac{\partial A}{\partial\nabla\mathbf{u}}\Big)\cdot\mathbf{w}\Big]d\Omega dt=\\
&=\int_0^T\int_{\partial\Omega}\frac{\partial A}{\partial\nabla\mathbf{u}}\mathbf{n}\cdot\mathbf{w}d\Gamma dt-\int_0^T\int_\Omega\Big(\nabla\cdot\frac{\partial A}{\partial\nabla\mathbf{u}}\Big)\cdot\mathbf{w}d\Omega dt.
\end{aligned}
$$

leads to:

$$\begin{aligned}\big\langle J_{\mathbf{u}}(\mathbf{u},p;\gamma),\mathbf{w}\big\rangle_{\mathcal{U}_{\Gamma_D}{}^*,\mathcal{U}_{\Gamma_D}} &= \int_0^T \int_\Omega \Big[\frac{\partial A}{\partial \mathbf{u}}\cdot\mathbf{w} - \Big(\nabla\cdot\frac{\partial A}{\partial\nabla\mathbf{u}}\Big)\cdot\mathbf{w}\Big] d\Omega dt + \\ &+ \int_0^T \int_{\partial\Omega} \frac{\partial A}{\partial\nabla\mathbf{u}}\mathbf{n}\cdot\mathbf{w} d\Gamma dt + \int_0^T\int_{\partial\Omega}\frac{\partial B}{\partial\mathbf{u}}\cdot\mathbf{w}d\Gamma dt.\end{aligned}$$

Finally, since $\mathbf{w}\in\mathcal{U}_{\Gamma_D}$, the integral over Γ_D is zero, and then

$$\begin{aligned}\big\langle J_{\mathbf{u}}(\mathbf{u},p;\gamma),\mathbf{w}\big\rangle_{\mathcal{U}_{\Gamma_D}{}^*,\mathcal{U}_{\Gamma_D}} &= \int_0^T \int_\Omega \Big[\frac{\partial A}{\partial \mathbf{u}}\cdot\mathbf{w} - \Big(\nabla\cdot\frac{\partial A}{\partial\nabla\mathbf{u}}\Big)\cdot\mathbf{w}\Big] d\Omega dt + \\ &+ \int_0^T \int_{\Gamma_N} \frac{\partial A}{\partial\nabla\mathbf{u}}\mathbf{n}\cdot\mathbf{w} d\Gamma dt + \int_0^T\int_{\Gamma_N}\frac{\partial B}{\partial\mathbf{u}}\cdot\mathbf{w}d\Gamma dt\end{aligned}$$

Following the same passages, the derivative of J with respect to p reads

$$\begin{aligned}&\big\langle J_p(\mathbf{u},p;\gamma),r\big\rangle_{\mathcal{P}^*,\mathcal{P}} = \lim_{l\to0}\frac{J(\mathbf{u},p+lr;\gamma)-J(\mathbf{u},p;\gamma)}{l} = \\ &= \lim_{l\to0}\frac{\int_0^T\int_\Omega A(\mathbf{u},\nabla\mathbf{u},p+lr;\gamma)d\Omega dt - \int_0^T\int_\Omega A(\mathbf{u},\nabla\mathbf{u},p;\gamma)d\Omega dt}{l} + \\ &+ \lim_{l\to0}\frac{\int_0^T\int_{\partial\Omega} B(\mathbf{u},p+lr;\gamma)d\Gamma dt - \int_0^T\int_{\partial\Omega} B(\mathbf{u},p;\gamma)d\Gamma dt}{l},\end{aligned}$$

Since the integrals are independent of the limit variable, the limit above is equivalent to:

$$\begin{aligned}\big\langle J_p(\mathbf{u},p;\gamma),r\big\rangle_{\mathcal{P}^*,\mathcal{P}} &= \lim_{l\to0}\frac{J(\mathbf{u},p+lr;\gamma)-J(\mathbf{u},p;\gamma)}{l} = \\ &= \int_0^T\int_\Omega \lim_{l\to0}\frac{A(\mathbf{u},\nabla\mathbf{u},p+lr;\gamma)-A(\mathbf{u},\nabla\mathbf{u},p;\gamma)}{l}d\Omega dt + \\ &+ \int_0^T\int_{\partial\Omega}\lim_{l\to0}\frac{B(\mathbf{u},p+lr;\gamma)-B(\mathbf{u},p;\gamma)}{l}d\Gamma dt,\end{aligned}$$

that implies:

$$\big\langle J_p(\mathbf{u}, p; \gamma), r \big\rangle_{\mathcal{P}^*,\mathcal{P}} = \int_0^T \int_\Omega \frac{\partial A}{\partial p} r d\Omega dt + \int_0^T \int_{\partial\Omega} \frac{\partial B}{\partial p} r d\Gamma dt.$$

By the Neumann BC, p can be expressed as a function of $\nabla \mathbf{u}$ in Γ_N. This means that B can be considered independent on p in Γ_N, i.e., $B(\mathbf{u}, p; \gamma) = B(\mathbf{u}, \nabla \mathbf{u}; \gamma)$ in Γ_N. Finally, the Gâteaux-derivative of J w.r.t p is:

$$\big\langle J_p(\mathbf{u}, p; \gamma), r \big\rangle_{\mathcal{P}^*,\mathcal{P}} = \int_0^T \int_\Omega \frac{\partial A}{\partial p} r d\Omega dt + \int_0^T \int_{\Gamma_D} \frac{\partial B}{\partial p} r d\Gamma dt.$$

The adjoint PDE of the Navier-Stokes equations for the topology optimization problem, can finally be formulated imposing (2.14), yielding

$$\begin{aligned} \big\langle e^*_{\mathbf{u}}(\mathbf{u}_a, p_a; \gamma), \mathbf{w} \big\rangle_{\mathcal{U}_{\Gamma_D}{}^*,\mathcal{U}_{\Gamma_D}} &= -\big\langle J_{\mathbf{u}}(\mathbf{u}, p; \gamma), \mathbf{w} \big\rangle_{\mathcal{U}_{\Gamma_D}{}^*,\mathcal{U}_{\Gamma_D}} \\ \big\langle e^*_p(\mathbf{u}_a, p_a; \gamma), r \big\rangle_{\mathcal{P}^*,\mathcal{P}} &= -\big\langle J_p(\mathbf{u}, p; \gamma), r \big\rangle_{\mathcal{P}^*,\mathcal{P}}. \end{aligned} \tag{2.19}$$

By equalizing the terms under the same integral signs, we obtain the following continuous formulation PDE system, whose weak formulation implies the weak formulation for the adjoint system derived above:

$$\begin{cases} -\rho\dfrac{\partial \mathbf{u}_a}{\partial t} - \mu\Delta\mathbf{u}_a - \rho(\mathbf{u}\cdot\nabla)\mathbf{u}_a + \rho(\nabla\mathbf{u})\mathbf{u}_a + \nabla p_a = \\ \qquad\qquad = -\Big(\dfrac{\partial A}{\partial \mathbf{u}} - \nabla\cdot\dfrac{\partial A}{\partial \nabla\mathbf{u}}\Big) + \dfrac{\partial \tilde{\mathbf{f}}}{\partial \mathbf{u}}\mathbf{u}_a, \text{ in } [0,T]\times\Omega \\ \nabla\cdot\mathbf{u}_a = \dfrac{\partial A}{\partial p} - \dfrac{\partial \tilde{\mathbf{f}}}{\partial p}\cdot\mathbf{u}_a, \text{ in } [0,T]\times\Omega \\ \mathbf{u}_a(T,\mathbf{x}) = 0, \text{ in } \Omega \\ \mathbf{u}_a = -\dfrac{\partial B}{\partial p}\mathbf{n}, \text{ on } [0,T]\times\Gamma_D \\ \big[-p_a\mathbb{I} + \mu\nabla\mathbf{u}_a\big]\mathbf{n} = \\ \qquad\qquad = -\rho(\mathbf{u}\cdot\mathbf{n})\mathbf{u}_a - \dfrac{\partial A}{\partial\nabla\mathbf{u}}\mathbf{n} - \dfrac{\partial B}{\partial \mathbf{u}}, \text{ on } [0,T]\times\Gamma_N. \end{cases} \tag{2.20}$$

The Dirichlet boundary conditions in the continuous formulation of the adjoint system comes from a first order approximation of the terms integrated over the boundary domain [24] [31].

Observing that

$$\mathbf{u}_a = -\frac{\partial B}{\partial p}\mathbf{n} \Rightarrow \int_0^T \int_{\Gamma_D} \Big(\mathbf{u}_a\cdot\mathbf{n} + \frac{\partial B}{\partial p}\Big) d\Omega dt$$

the weak formulation of (2.20) implies also the weak formulation derived in (2.19).

2.3 The functionals

The objective functional is the focal point of every optimization algorithm; once the problem constraints have been identified, its formulation determines the *optimization parameters dynamics*. This not only impacts the optimization procedure, but also influences the adjoint system by changing the forcing in the momentum adjoint equation, the adjoint compressibility, and both the adjoint Dirichlet and Neumann BCs. In the case of continuous systems, the classical formulation involves the integral over the parameter-space, i.e., $[0, T] \times \Omega$, of a selected cost function density, which usually accounts relevant quantities of the considered problem.

The cost function for the topology optimization of the fluid domain problem in (2.8) can be described as the total energy dissipation of the system throughout the domain. Since the general fluid dynamics problem is time and space dependent, $t \in [0, T]$, and $\mathbf{x} \in \Omega$, the considered cost function involves the integral over the space and time of the power density. Accordingly, the functional formulation in (2.9), J is rewritten as:

$$
\begin{aligned}
J(\mathbf{u}, p; \gamma) = & \int_0^T \int_\Omega \big[\text{volume power density}\big] d\Omega dt \\
& + \int_0^T \int_{\partial\Omega} \big[\text{surface power density}\big] d\Gamma dt,
\end{aligned}
$$

with the integrating functions defined as:

$$\begin{aligned} A(\mathbf{u}, \nabla\mathbf{u}, p, \gamma) := \beta_\alpha \alpha ||\mathbf{u}||^2 + \beta_S \frac{1}{2}\mu ||\nabla\mathbf{u} + \nabla\mathbf{u}^T||^2 + \\ + \beta_R \frac{1}{2}\mu ||\nabla \times \omega||^2; \end{aligned} \tag{2.21}$$

$$B(u, p, \gamma) := \beta_p p. \tag{2.22}$$

In order to take into account the various energy terms, the weighted approach has been used [12].

2.3.1 Power Dissipation in Fluid Dynamics

Given the definition of a fluid as *"a material that deforms continuously under the action of a shear stress"* [32], the deformation and rotation rates of the fluid elements are determined by the knowledge of the stresses acting over them. Moreover, since both the deformations and rotations can be described using the velocity gradient tensor, the power dissipation term integrated over the volume is studied using the classical symmetric and anti-symmetric decomposition, i.e.,

$$\nabla\mathbf{u} = S + \frac{1}{2}R \tag{2.23}$$

where

$$S := \frac{1}{2}\Big(\nabla\mathbf{u} + \nabla\mathbf{u}^T\Big) \text{ is the strain rate} \tag{2.24}$$

and

$$R := \nabla \mathbf{u} - \nabla \mathbf{u}^T \text{ is the rotation rate.} \tag{2.25}$$

Introducing the vorticity $\omega := \nabla \times \mathbf{u}$, R reads:

$$R = \begin{bmatrix} 0 & -\omega_3 & \omega_2 \\ \omega_3 & 0 & -\omega_1 \\ -\omega_2 & \omega_1 & 0 \end{bmatrix} \tag{2.26}$$

The diagonal entries of S describe the straight deformation effect along each component, while the off-diagonal terms represent the average rate of angular deformation. R entries, instead, represent twice the effective fluid element rotation rate [32].

With the above definitions, the volume power density can be rewritten as:

$$A(\mathbf{u}, \nabla\mathbf{u}, p, \gamma) := \beta_\alpha \alpha ||\mathbf{u}||^2 + \beta_S 2\mu ||S||^2 + \beta_R \frac{1}{4}\mu ||R||^2 \tag{2.27}$$

In absence of heat forces and adiabatic BCs, the sum of the first and second term of the right-hand side of (2.26) can be derived by multiplying the momentum equation with the velocity field and integrating by parts [31].

Finally, in case of a Stokes flow, when the Dirichlet conditions are the only conditions prescribed at the boundary, the problem of minimizing the total power dissipation inside the domain, subject to a volume constraint on the material distribution, is mathematically well-posed

[33].

Moreover, it is important to stress that *"the minimization of the dissipated power is equivalent to minimization of the pressure drop across the flow field"*[33], [34],[35].

To compute the effective formulation of the adjoint system for a functional defined by Equations (2.21)-(2.22), the derivative of the power density over $\mathbf{u}, \nabla\mathbf{u}$, and p must be computed. Firstly, it can be observed that

$$\begin{aligned} \frac{\partial A}{\partial p} &= 0; \\ \frac{\partial B}{\partial \mathbf{u}} &= 0. \end{aligned} \tag{2.28}$$

Then, since the direct dependence on $\mathbf{u}$ is taken into account only in the power dissipation due to permeability term, we have

$$\frac{\partial A}{\partial \mathbf{u}} = \frac{\partial\big(\beta_\alpha \alpha ||\mathbf{u}||^2\big)}{\partial \mathbf{u}} = 2\beta_\alpha \alpha \mathbf{u}. \tag{2.29}$$

On the other hand, in the partial derivative of $A(\mathbf{u}, \nabla\mathbf{u}, p; \gamma)$ with respect to $\nabla\mathbf{u}$, only the terms involving the velocity gradient components have a direct dependence on the velocity gradient, i.e.,

$$\begin{aligned} \frac{\partial A}{\partial \nabla\mathbf{u}} &= \frac{\partial\big(\beta_S \frac{1}{2}\mu ||\nabla\mathbf{u} + \nabla\mathbf{u}^T||^2\big)}{\partial \nabla\mathbf{u}} + \frac{\partial\big(\beta_R \frac{1}{2}\mu ||\nabla \times \omega||^2\big)}{\partial \nabla\mathbf{u}} = \\ &= \beta_S \frac{1}{2}\mu \frac{\partial ||\nabla\mathbf{u} + \nabla\mathbf{u}^T||^2}{\partial \nabla\mathbf{u}} + \beta_R \frac{1}{2}\mu \frac{\partial ||\nabla \times \omega||^2}{\partial \nabla\mathbf{u}} \end{aligned} \tag{2.30}$$

For the sake of simplicity, it is convenient to define the following terms:

$$\mathcal{S} := \frac{\partial ||\nabla \mathbf{u} + \nabla \mathbf{u}^T||^2}{\partial \nabla \mathbf{u}}$$
$$\mathcal{R} := \frac{\partial ||\nabla \times \omega||^2}{\partial \nabla \mathbf{u}},$$

which replaced into (2.30) give

$$\frac{\partial A}{\partial \nabla \mathbf{u}} = \frac{1}{2}\beta_S \mu \mathcal{S} + \frac{1}{2}\beta_R \mu \mathcal{R} \tag{2.31}$$

The analytic formulations for $\mathcal{S}$ and $\mathcal{R}$ can be derived as follows:

$$\mathcal{S} = 2\big(\nabla \mathbf{u} + \nabla \mathbf{u}^T\big) : \left(\frac{\partial\big(\nabla \mathbf{u} + \nabla \mathbf{u}^T\big)}{\partial \nabla \mathbf{u}}\right)$$

Using indices and the Einstein convection, it is rewritten as

$$\begin{aligned}\mathcal{S}_{kl} &= 2\big(\nabla \mathbf{u} + \nabla \mathbf{u}^T\big)_{ij}\left(\frac{\partial\big(\nabla \mathbf{u} + \nabla \mathbf{u}^T\big)}{\partial \nabla \mathbf{u}}\right)_{ijkl} = \\ &= 2\big(\nabla \mathbf{u} + \nabla \mathbf{u}^T\big)_{ij}\left(\frac{\partial\big(\nabla \mathbf{u} + \nabla \mathbf{u}^T\big)_{ij}}{\partial \nabla \mathbf{u}_{kl}}\right),\end{aligned}$$

and being

$$\begin{aligned}\frac{\partial \nabla \mathbf{u}_{ij}}{\partial \nabla \mathbf{u}_{kl}} &= \frac{\partial\left(\frac{\partial \mathbf{u}_i}{\partial x_j}\right)}{\partial\left(\frac{\partial \mathbf{u}_k}{\partial x_l}\right)} = \delta_{ik}\delta_{jl} \qquad \text{and} \\ \frac{\partial \nabla \mathbf{u}^T_{ij}}{\partial \nabla \mathbf{u}_{kl}} &= \frac{\partial\left(\frac{\partial \mathbf{u}_j}{\partial x_i}\right)}{\partial\left(\frac{\partial \mathbf{u}_k}{\partial x_l}\right)} = \delta_{il}\delta_{jk}\end{aligned} \tag{2.32}$$

finally yields to

$$\mathcal{S}_{kl} = 2\big(\nabla\mathbf{u} + \nabla\mathbf{u}^T\big)_{ij}\big(\delta_{ik}\delta_{jl} + \delta_{il}\delta_{jk}\big).$$

The latter, since the contraction involves the $i - j$ indices, reads as

$$\begin{aligned} \mathcal{S}_{kl} &= 4\big(\nabla\mathbf{u} + \nabla\mathbf{u}^T\big)_{kl} \qquad \Rightarrow \\ \mathcal{S} &= 4\big(\nabla\mathbf{u} + \nabla\mathbf{u}^T\big) = 8S. \end{aligned} \tag{2.33}$$

The derivative of the vorticity term can be derived similarly. In fact, by the definition of vorticity, it holds

$$\begin{gathered} ||\nabla \times \mathbf{u}||^2 = \frac{1}{2}||R||^2 \\ \text{which implies} \\ \mathcal{R} = \frac{1}{2}\frac{\partial ||R||^2}{\partial \nabla\mathbf{u}} = \frac{1}{2}\frac{\partial ||\nabla\mathbf{u} - \nabla\mathbf{u}^T||^2}{\partial \nabla\mathbf{u}}. \end{gathered} \tag{2.34}$$

Equation (2.34) can be rearranged as follows

$$2\mathcal{R} = 2\big(\nabla\mathbf{u} - \nabla\mathbf{u}^T\big) : \left(\frac{\partial\big(\nabla\mathbf{u} - \nabla\mathbf{u}^T\big)}{\partial \nabla\mathbf{u}}\right)$$

and by (2.32), it can be rewritten as

$$2\mathcal{R}_{kl} = 2\big(\nabla\mathbf{u} - \nabla\mathbf{u}^T\big)_{ij}\big(\delta_{ik}\delta_{jl} - \delta_{il}\delta_{jk}\big),$$

i.e,

$$\begin{aligned} \mathcal{R}_{kl} &= 2\big(\nabla\mathbf{u} - \nabla\mathbf{u}^T\big)_{kl} \qquad \Rightarrow \\ \mathcal{R} &= 2\big(\nabla\mathbf{u} - \nabla\mathbf{u}^T\big) = 2R. \end{aligned} \tag{2.35}$$

In conclusion, by replacing Equations (2.33) and (2.35) into (2.31), the derivative of the volume power density, A, is related to the velocity gradient by the following expression.

$$\begin{aligned}\frac{\partial A}{\partial \nabla \mathbf{u}} &= 2\beta_S\mu\big(\nabla\mathbf{u} + \nabla\mathbf{u}^T\big) + \beta_R\mu\big(\nabla\mathbf{u} - \nabla\mathbf{u}^T\big) = \\ &= 4\mu\beta_S S + \mu\beta_R R.\end{aligned} \tag{2.36}$$

Finally, given its simple formulation, the derivative of the surface power density over the pressure, is trivially

$$\frac{\partial B}{\partial p} = 1. \tag{2.37}$$

2.3.2 The complete adjoint PDE formulation

Replacing (2.36), (2.37) and (2.6) in the adjoint PDE (2.20) leads to the formulation of a system of PDE similar to the NS equations. However, the adjoint system does not have any non-linear term in its momentum equation formulation, granting an easier numerical solution. The right-hand side part is a combination of terms involving the NS forcing and J derivatives and the NS equations solutions, $\mathbf{u}$ and p. The continuity equation has the same structure of the NS system, with a sink term depending on the derivative of $\mathbf{f}$ w.r.t. p. The boundary conditions are formulated following the Dirichlet and Neumann definitions, and the time variable dependence is transformed in a final value problem.

$$\begin{cases} -\rho\dfrac{\partial \mathbf{u}_a}{\partial t} - \mu\Delta\mathbf{u}_a - \rho(\mathbf{u}\cdot\nabla)\mathbf{u}_a + \rho(\nabla\mathbf{u})\mathbf{u}_a + \nabla p_a = \\ \qquad = -2\beta_\alpha\alpha\mathbf{u} + \nabla\cdot\big(4\mu\beta_S S + \mu\beta_R R\big) + \\ \qquad\quad -\alpha\mathbf{u}_a + \dfrac{\partial\mathbf{f}}{\partial\mathbf{u}}\mathbf{u}_a, & \text{in } [0,T]\times\Omega \\ \nabla\cdot\mathbf{u}_a = -\dfrac{\partial\mathbf{f}}{\partial p}\cdot\mathbf{u}_a, & \text{in } [0,T]\times\Omega \\ \mathbf{u}_a(T,\mathbf{x}) = 0, & \text{in } \Omega \\ \mathbf{u}_a = -\mathbf{n}, & \text{on } [0,T]\times\Gamma_D \\ \big[-p_a\mathbb{I} + \mu\nabla\mathbf{u}_a\big]\mathbf{n} = \\ \qquad = -\rho(\mathbf{u}\cdot\mathbf{n})\mathbf{u}_a - \big(4\mu\beta_S S + \mu\beta_R R\big)\mathbf{n}, & \text{on } [0,T]\times\Gamma_N. \end{cases} \tag{2.38}$$

Chapter 3

Materials and Methods

To study the problem of the topology optimization of the aortic root, the development of a most general tool is required. To properly work, the model has to use various boundary conditions, different initial geometries, and multiple functional weights distributions. In order to face such a complicated task, a completely independent C++ topology optimization software has been implemented. The software is based on the finite element method to solve both the Navier-Stokes and its adjoint systems. Further, it integrates a differential analysis on the objective functional and the constraints to update the design parameter. The choice of implementing the whole topology optimization allows to have an almost complete comprehension of which crucial tasks are involving in its development and how to deal with them. This didactic-oriented choice demonstrated to be correct, since several implemented features proved to be helpful in the project progresses, such as different kinds of BCs or new functional terms.

Furthermore, the versatility of the use and modification of the custom software allows to treat the fluid domain topology optimization problem, considering 3D geometries and time-dependence. These features are not so frequent in the literature (see e.g. [18]), but they are fundamental for the final purpose of this work. Once the software was ready to be used, a parameter sensitivity analysis has been performed, preparatory to the development of a conscious functional formulation.

3.1 The Software Development

To correclty work, the software needs of several input files, namely, the geometry input file, the forcing and BC input file, the topology optimization input file, and the output format input file.

To deal with various geometries, a tool to import meshes from the commercial software COMSOL Multiphysics® (COMSOL, Inc., Stockholm, Sweden [36]) has been implemented. Every information about the geometry and its boundaries is processed and transformed to be suitable for the main program.

3.1.1 Finite Element Method Techniques

To avoid instabilities of the numerical method, mixed FEM spaces satisfying the *inf-sup condition* must be chosen [25],[37]. The most common example of mixed FEM spaces are the Raviart-Thomas ($\mathcal{RT}_q$) or the Taylor-Hood $\mathcal{P}_k - \mathcal{P}_k$ function spaces. However, since the software works with FE discretizations using first order shape function. The chosen mixed FEM stable space is $\mathcal{P}_1 - iso - \mathcal{P}_2/\mathcal{P}_1$ (see Figure 3.1).

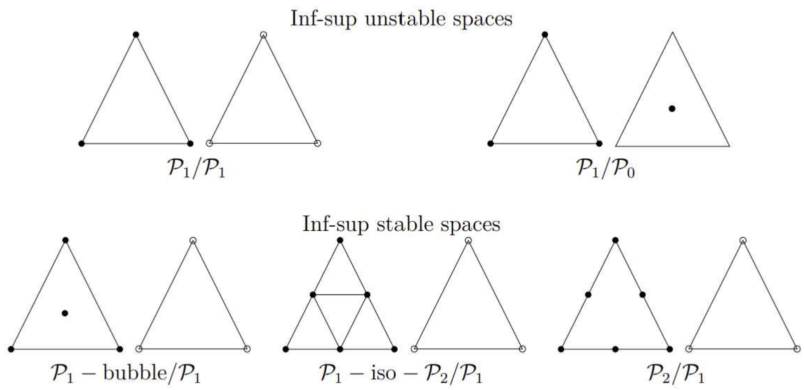

Figure 3.1: FEM spaces. Image from [25]

3.1.2 The Boundary Conditions

The momentum and continuity equation of the NS PDEs are completely determined once the physics parameters are chosen. Then, the solution of (2.2) is determined by the prescribed boundary and initial conditions. Gresho et al. [38] and Koch et al. [39], proved the existence and uniqueness of the solution, up to a constant for p, given regular Dirichlet BC $\left(\text{e.g., in our case } \mathbf{u}_D \in (\mathscr{H}^1(\Gamma_D))^d\right)$. Accordingly, given the Dirichlet BC, to set at least one condition on the pressure value at the boundary (e.g., the Neumann BC) is sufficient to guarantee the well posedness of the F.E.M. problem [25].

The Dirichlet boundary conditions have been applied fixing the nodal value of the velocity in each component

$$\mathbf{u} = \mathbf{u}_D \qquad\qquad in\ [0, T] \times \Gamma_D \tag{3.1}$$

For simplicity of notation, the no-slip boundaries, i.e.,

$$\mathbf{u}_D = 0 \tag{3.2}$$

will be referred as "wall" boundaries.

The Neumann boundary conditions are implemented in order to set the mean pressure value over a part of the boundary. If the no-slip condition is set to the adjacent edges, the prescription of the mean pressure is approximated setting

$$\mathbf{g}_i = \bar{p} \qquad i \in \{1, ..., \mathrm{dim}\}.$$

Thereby, the open boundary conditions are obtained just by setting $\bar{p} = 0$, i.e.,

$$\Big(-\frac{1}{\rho} p\mathbb{I} + \nu \nabla \mathbf{u} \Big) \mathbf{n} = \mathbf{g} \qquad in\ [0, T] \times \Gamma_N. \tag{3.3}$$

However, Heywood et al. [40] showed this approximation scales as the inverse of the radius of curvature. Thus, the use of planar boundaries are not affected by approximations on the mean pressure value.

In many problem the symmetry of the geometry can be exploited to reduce the size of the domain of analysis. The condition of symmetry has been implemented by setting to zero the normal velocity and the normal derivative of its parallel component at the boundary, i.e.,

$$\begin{aligned} \mathbf{u}_\perp &= (\mathbf{u} \cdot \mathbf{n})\mathbf{n} = 0 \\ \frac{\partial \mathbf{u}_{/\!/}}{\partial \mathbf{n}} &= \frac{\partial (\mathbf{u} - \mathbf{u}_\perp)}{\partial \mathbf{n}} = 0 \end{aligned} \qquad in\ [0, T] \times \Gamma_S \tag{3.4}$$

In topology optimization problems, the prescription of the direction of the outflow could be functional to the final result of the analysis. In the present work, even if they does not simulate the natural behaviour of a fluid, the normal velocity at the boundary has been developed. This kind of BC has been thought to study the aortic root problem and, being the normal vector at the aorta's outlet equal to $\mathbf{n} = (0, 0, 1)$ (in

3D), their definition reads

$$\begin{matrix} \mathbf{u}_i = 0 & i \in \{1, ..., \text{dim-1}\} \\ \mathbf{g}_{i=dim} = 0 & \end{matrix} \quad in\ [0, T] \times \Gamma_{NVOB} \tag{3.5}$$

3.1.3 The Solver

The weak FEM Galerkin formulation leads to the construction of a linear system to be solved; therefore also a custom solver for linear system has been developed. Starting from the classical GMRES algorithm, the SIMPLE algorithm [41] as a preconditioner has been implemented to enhance the convergence [42]. The SIMPLE is a well known procedure, specific for linear systems deriving from the discretization of the NS equations, and used, for example, by software like OpenFoam® [43].

The convective term has been treated using the Picard iterative approach. This scheme solves the NS equations through a fixed point approach setting the velocity field of the convective term equal to the solution of the previous iteration. The Picard approach demonstrated to be very efficient to solve high number of degree of freedoms problems [44].

However, the solution of each iteration could suffer some instabilities if the Peclet's number

$$\mathbf{Pe} := \frac{||\mathbf{u}||_\infty h_{max}}{\nu}, \qquad h_{max} = \max_{el \in mesh} \max_{\text{side } h \in el} \{h\}$$

value is too high. In this case, some stabilization techniques must be applied. Here it has been included the SUPG stabilization term [45], which ensures the stability of the algorithm, despite the introduction of some "numerical diffusion" in the solution.

The High Performance Computing

After a computational time analysis of the code, to reach the best performances, a parallelization of the "heaviest" sections has been performed. To do so, multi-threading procedures through the methods of the *OpenMP* library have been implemented.

3.1.4 The Optimizers

After the solution of the Navier-Stokes equation and its adjoint PDE, the sensitivity analysis of the objective functional derivative of the functional (2.7) is computed and, then, the effective optimization procedure starts.

The software works with two different numerical schemes of optimization: the *Generalized Optimality Criteria (GOC)* and the *Method* *of Moving Asymptotes (MMA)*.

The GOC works solving at each iteration the K.K.T. conditions (as in [15]), and finding an approximate solution converging to the correct one.

The MMA, instead, simplifies the initial problem iterating on the solution of sub-problems. These subproblems are formulated by linearizing the constraints with respect to the reciprocal of each position component. The information of the previous iterations are exploited to evaluate the lower and upper bounds for the design variables, i.e., the *moving asymptotes*.

The MMA has two main advantages: it is easy to comprehend and use and, at the same time, it is faster to converge than "traditional optimization methods". Its main drawback is owing to some instabilities that may originate from high values of α_{max} [46]. On the contrary, the GOC solution, usually, has a greater stability when the value of α_{max} is high, but, in most general cases, its convergence requires more iterations than the MMA.

3.1.5 Flowcharts

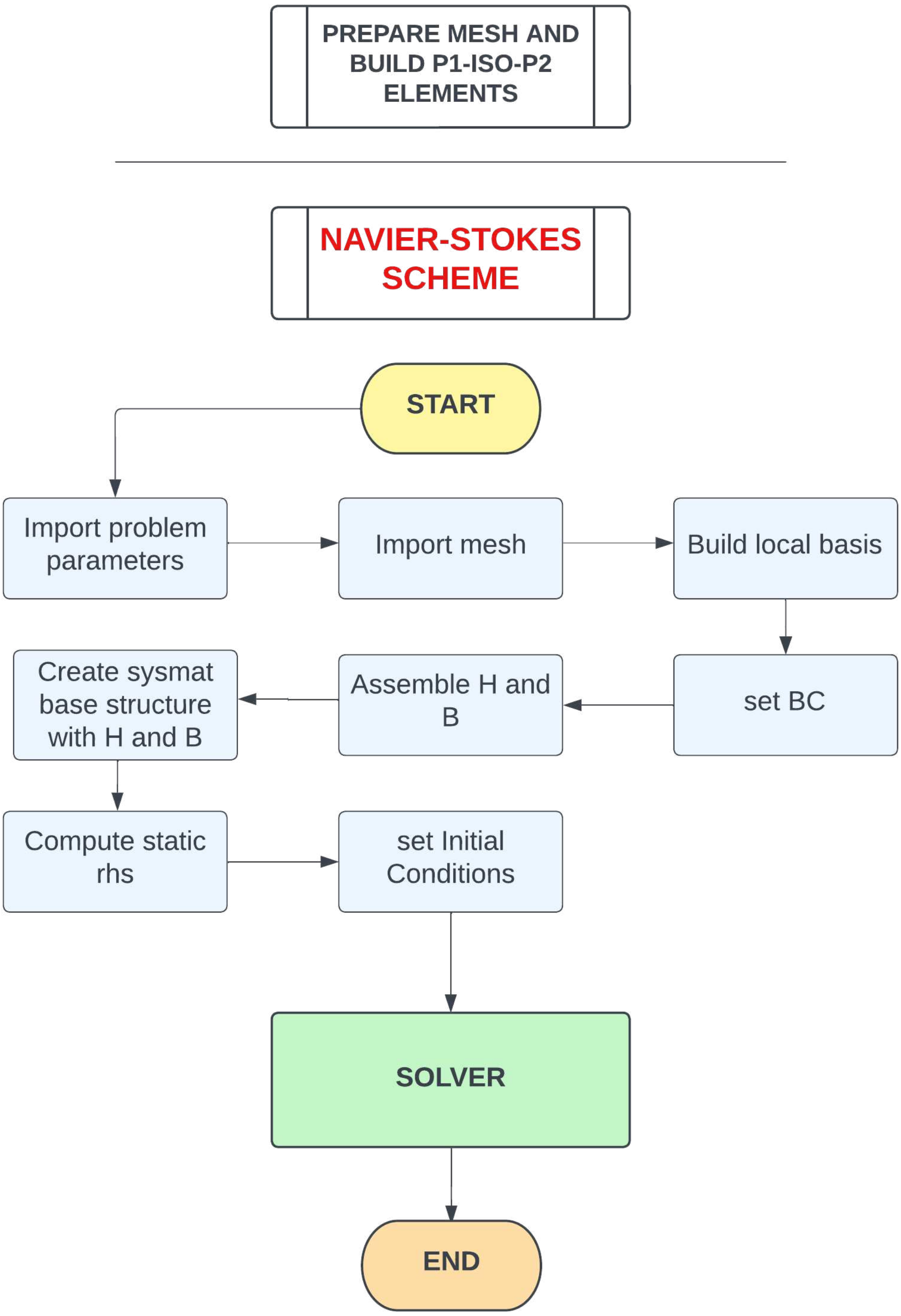

Figure 3.2: Software: Navier-Stokes Solution Flowchart

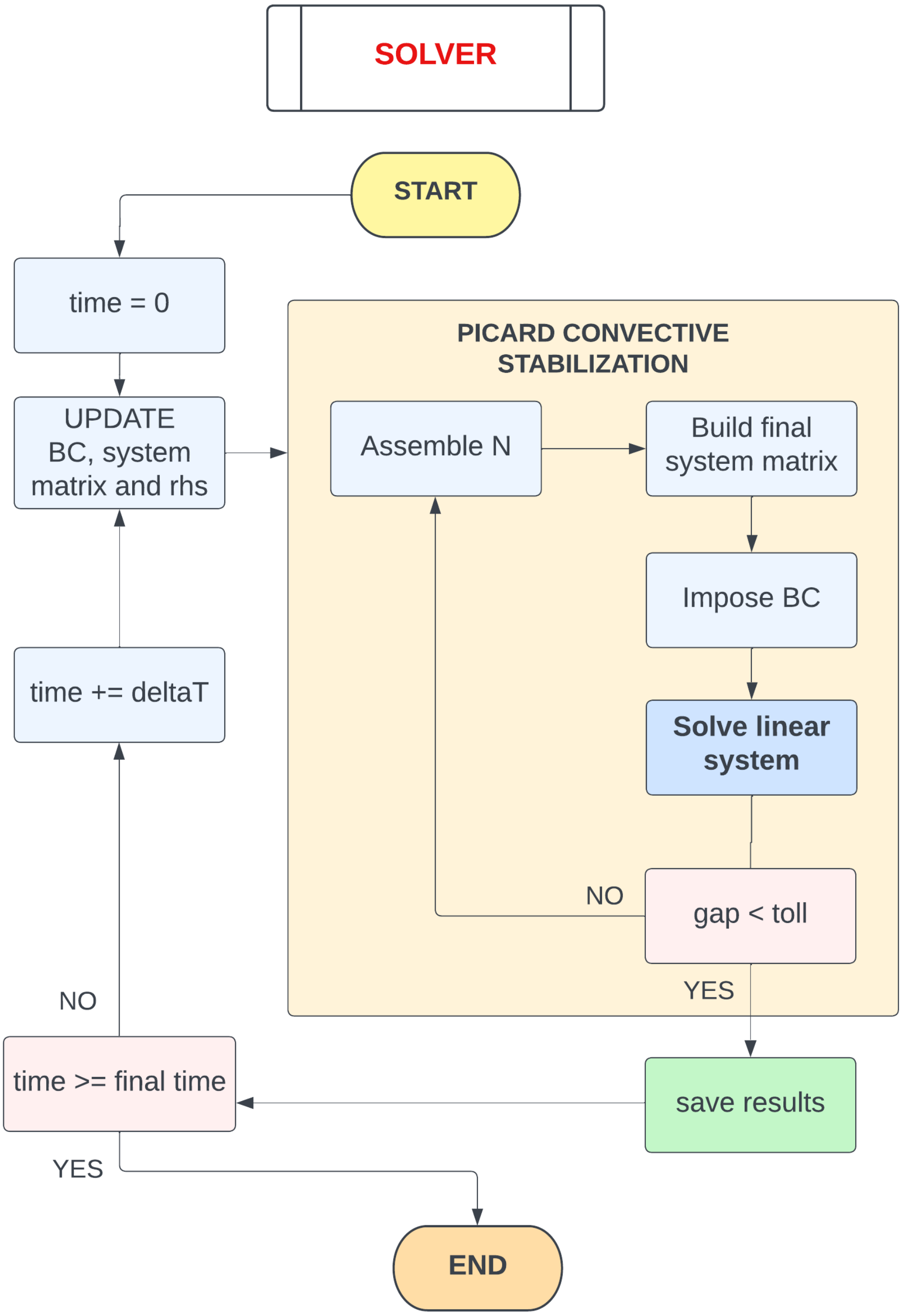

Figure 3.3: Software: Navier-Stokes Solver Flowchart

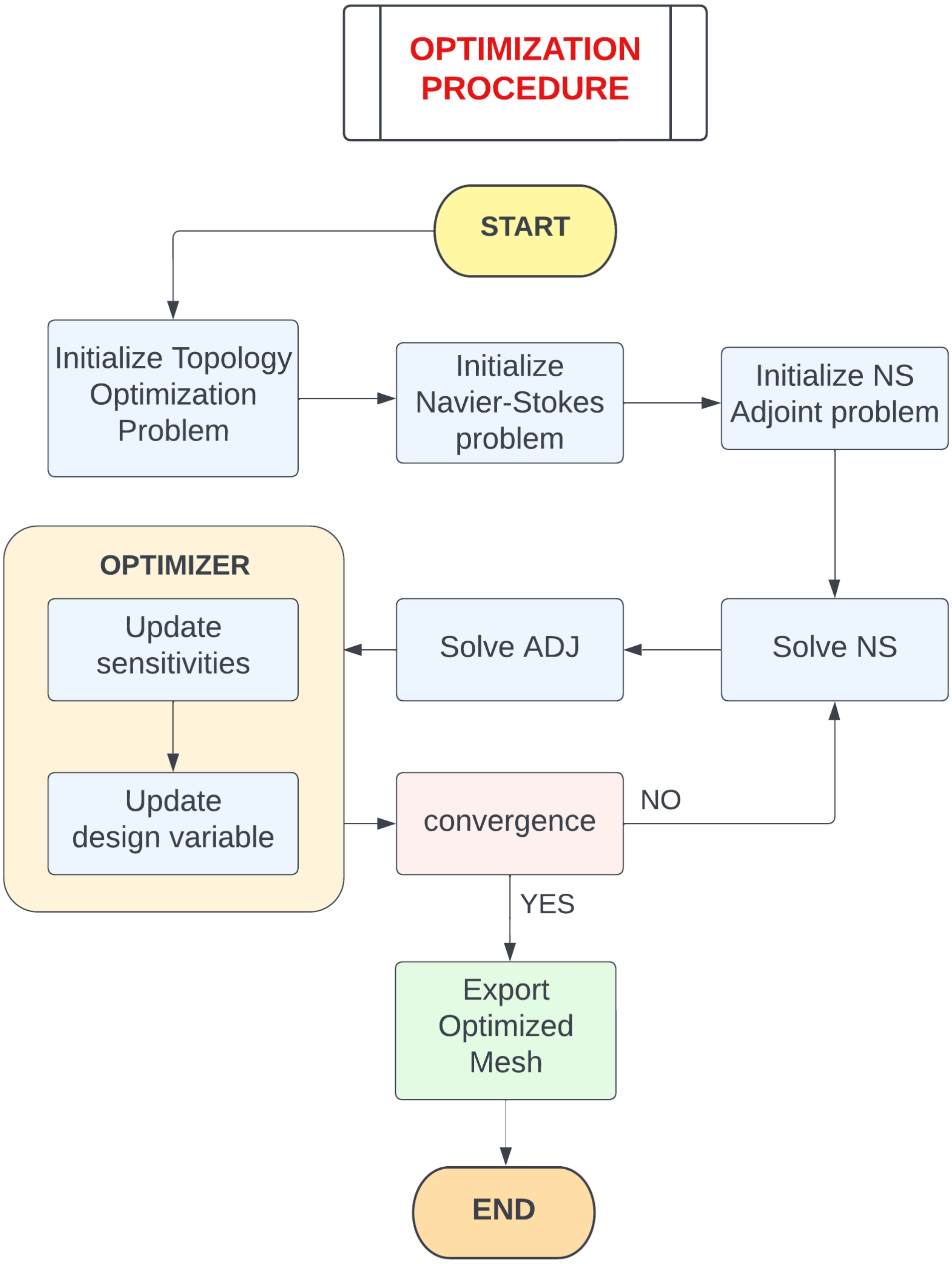

Figure 3.4: Software: Optimization Flowchart

3.2 Functional's Analysis

Substituting (2.27) and (2.22) in (2.9), the explicit formulation of the functional for the considered problem reads

$$J(\mathbf{u}, p, \gamma) = \int_0^T \int_\Omega \Big[\underbrace{\beta_\alpha \alpha ||\mathbf{u}||^2}_{\text{Permeability term}} + \underbrace{\beta_S 2\mu ||S||^2}_{\text{Deformation term}} + \underbrace{\beta_R \frac{1}{4}\mu ||R||^2}_{\text{Vorticity term}} \Big] d\Omega dt + \\ + \int_0^T \int_{\partial\Omega} \underbrace{\beta_p p}_{\text{Pressure term}} \; d\Gamma dt. \tag{3.6}$$

Therefore, once the values of $\mathbf{u}$, p, and γ are fixed, J value depends on the tuning of four functional parameters: $\beta_\alpha, \beta_S, \beta_R$ and β_p.
In order to work with a controlled value of the functional [12], in the weighted approach following equality must hold

$$\sum_i |\beta_i| = |\beta_\alpha| + |\beta_S| + |\beta_R| + |\beta_p| = 1. \tag{3.7}$$

It is now proposed a simple standard procedure to reduce the problem parameters, exploiting the ratios of the objective functional terms involving the velocity gradient and pressure terms. Since the power dissipation inside the fluid domain is owing to the sum of the terms multiplied by β_α and β_S, they are chosen to be equal, i.e., $\beta_\alpha = \beta_S$, and (3.7) reduces to

$$2|\beta_S| + |\beta_R| + |\beta_p| = 1 \tag{3.8}$$

Since the implemented algorithm works only with minimization problems, to easily study the maximization of a functional term contribution, the relative weight must be chosen with a negative sign.
Assuming $\beta_S \neq 0$, to easily define the study cases the following coefficient ratios are defined:

$$\begin{aligned} \beta_R^* &:= \frac{\beta_R}{\beta_S}; \\ \beta_p^* &:= \frac{\beta_p}{\beta_S}. \end{aligned} \tag{3.9}$$

3.2.1 The Vorticity term

The vorticity term has been introduced in the objective functional accordingly to the study of *Berggreen* [47], and its first applications in the field of shape optimization by Quarteroni [48] and Abraham [49]. Nevertheless, in the topology optimization only two-dimensional models included the minimization of the fluid rotor norm (see Sá et al. [50]).

In this section the vorticity term coefficient is embedded in the functional structure. To enhance the comprehension of the problem, magnitude analysis of the power density terms involving the velocity gradient components (2.23) is recommended.

Equalizing the deformation and vorticity terms of (3.6) yields to:

$$\beta_S \frac{1}{2}\mu||\nabla \mathbf{u} + \nabla \mathbf{u}^T||^2 = \beta_R \frac{1}{2}\mu||\nabla \times \omega||^2,$$

by substituting (2.34), the above equality becomes

$$\beta_S \frac{1}{2}\mu||\nabla \mathbf{u} + \nabla \mathbf{u}^T||^2 = \beta_R \frac{1}{4}\mu||\nabla \mathbf{u} - \nabla \mathbf{u}^T||^2$$

that is equivalent to

$$\beta_S = \frac{1}{2} \cdot \frac{||\nabla \mathbf{u} - \nabla \mathbf{u}^T||^2}{||\nabla \mathbf{u} + \nabla \mathbf{u}^T||^2} \cdot \beta_R \tag{3.10}$$

Since performing a scale analysis it easily follows the the two norms have the same magnitude, (3.10) can be approximated by

$$\beta_S = \frac{1}{2}\beta_R.$$

Therefore, the *a priori* strain rate (deformation) term is almost twice the vorticity term in the functional.

$$[\text{Deformation term}] \simeq 2 \cdot [\text{Vorticity term}]. \tag{3.11}$$

This means that choosing $|\beta_R^*| = 1$, the rotational effects should weight the half of the deformation ones. For more details, see Appendix C.

3.2.2 Analysis of $\alpha_q(\gamma)$

Recalling the definition of $\alpha(\gamma)$:

$$\alpha(\gamma) = \alpha_q(\gamma) := \alpha_{min} + (\alpha_{max} - \alpha_{min})\frac{q\gamma}{q+1-\gamma}$$

and considering its partial derivatives on γ:

$$\alpha'(\gamma) = (\alpha_{max} - \alpha_{min})\frac{q(1+q)}{(q+1-\gamma)^2} > 0 \tag{3.12}$$

$$\alpha''(\gamma) = 2(\alpha_{max} - \alpha_{min})\frac{q(1+q)}{(q+1-\gamma)^3} > 0 \tag{3.13}$$

$\forall\gamma \in [0,1]$ and $\forall q > 0$, it can be observed that $\alpha(\gamma)$ is a concave, increasing function.

Moreover, since

$$\lim_{q\to\infty} \alpha_q(\gamma) = \begin{cases} \alpha_{min}, & \gamma = 0 \\ \alpha_{max}, & \gamma \in]0,1] \end{cases}$$

if $q \ll 1$, $\alpha(\gamma)$ behaves like a linear function, and for $q \gg 1$, instead, it behaves like a step function (see Figure 3.5).

On conclusion, for large values of q, we expect quasi-discrete optimizing interfaces; on the contrary, for small q, a smoother transition is expected in the contour definition.

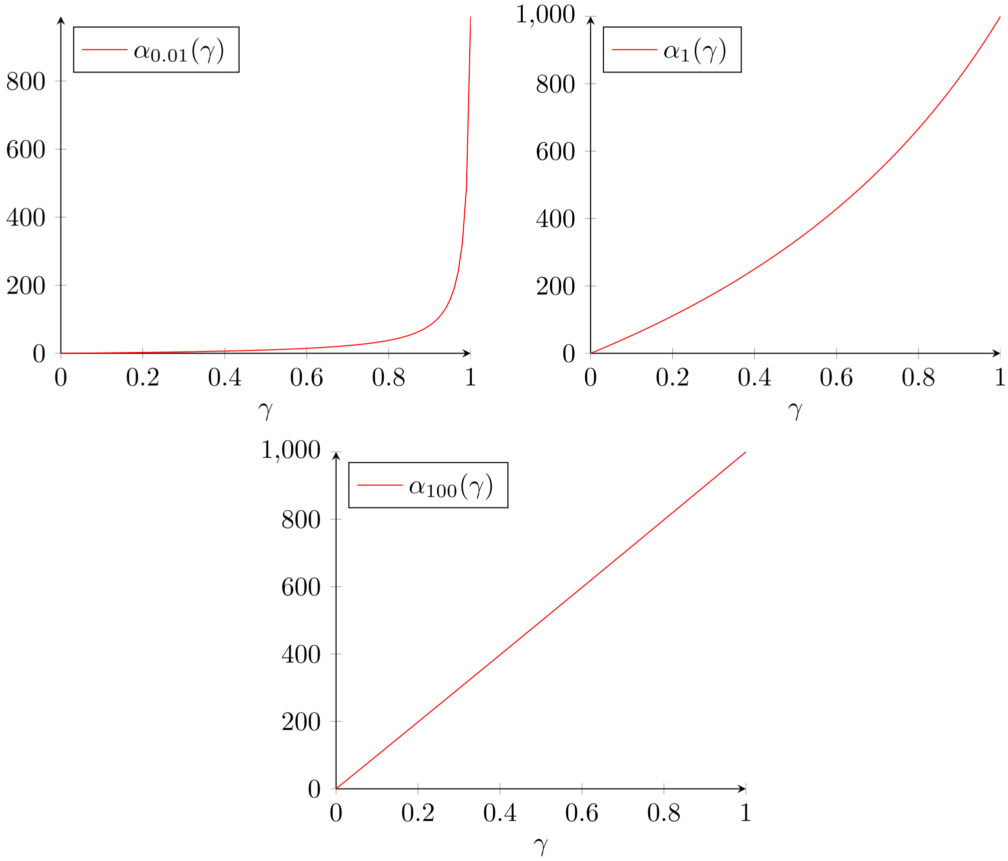

Figure 3.5: $\alpha_q(\gamma)$ comparison with $q = 0.01, 1, 100$

3.3 Preliminary Study-cases

The topology optimization of a fluid domain is a field of research still far from being understood. Although the articles production in this field is facing an exponential growth Dbouk [17] and Alexander [18] showed that the developed functional formulations, or the considered domain structures lack of variety.

One of the purposes of this work is trying to apply the Topological optimization method to study the aortic root district. The goal is quite ambitious and can be achieved only through the implementation of a complete model formulation (e.g., time-dependent, three dimensional) and the formulation of new functionals.

To assess the proposed algorithm parameters, a series of preliminary tests has been performed and reported in the following sections.

3.3.1 Oblique Plate in a Rectangular Domain

First, it has been analyzed the model response at varying the Reynolds number.

The Reynolds number is defined as

$$\mathbf{Re} := \frac{||\mathbf{u}||_{\max} \cdot L}{\nu}, \tag{3.14}$$

where $||\mathbf{u}||_{\max}$ is the maximum value for the velocity magnitude, L is the characteristic length of the domain and $\nu = \mu/\rho$ is the cinematic viscosity of the fluid.

The domain to optimize consists in a rectangle, with a basis $b = 2m$ and height $h = 1m$, with a rectangular hole, of sizes $0.3m \times 0.05m$, inclined w.r.t. the x-axis of 75 (see Figure 3.6).

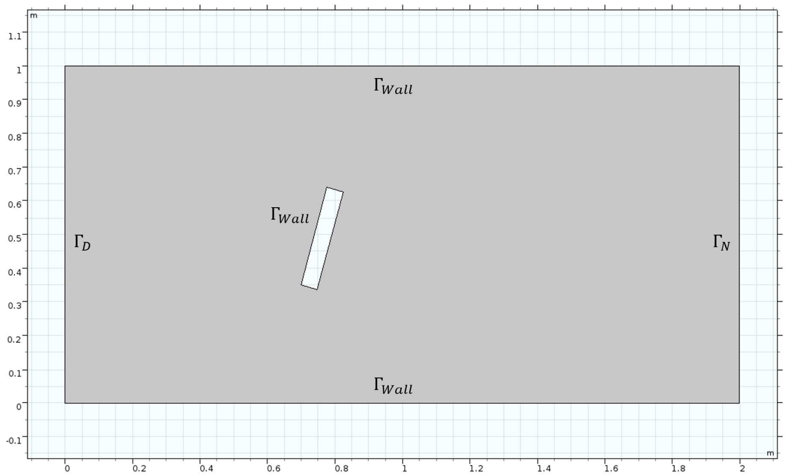

Figure 3.6: Oblique Plate in a Rectangular Domain

To study the topology optimization behaviour over different values of $\mathbf{Re}$, it has been considered a stationary problem, and the following boundary conditions

$$\begin{cases} \mathbf{u}_D = \big(4 \cdot y \cdot (1-y), 0\big)\ m/s & in\ \Gamma_D, \\ \mathbf{g} = \big(0, 0\big)\ Pa & in\ \Gamma_N. \end{cases} \tag{3.15}$$

The topology optimization parameter are set to be:

V_r	α_{min}	α_{max}	q	β_α	β_S	β_R	β_p
0.6	0	1e3	1	1	1	0	0

Table 3.1: Obliques plate in a rectangular domain: Topology optimization parameters.

3.3.2 Channel in a Squared Domain

The goal of this study-case is to investigate on the newly introduced vorticity term in the objective functional formulation (3.6). To this purpose two different functional weights values of β_R^* have been studied, namely $\beta_R^* = 0$ and $\beta_R^* = -2$. The initial geometry consists in a square of length $l = 1m$. The presence of a channel is simulated imposing an inlet velocity and an open boundary outlet in two segments of length $0.4m$, respectively Γ_D and Γ_N, centered in the lower and upper sides (see Figure 3.7).

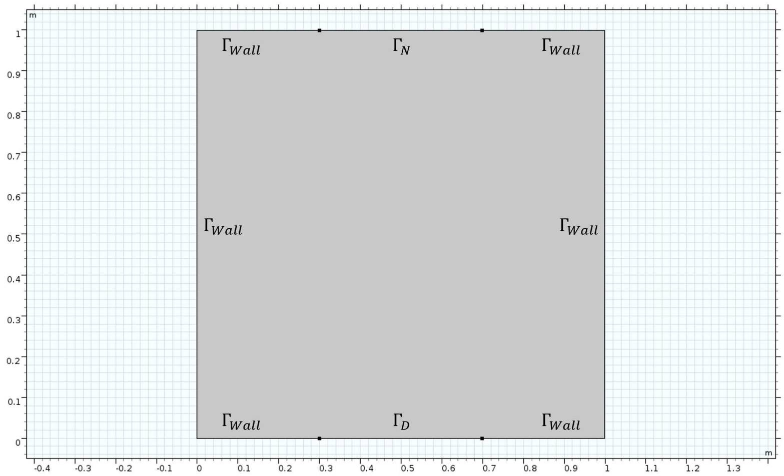

Figure 3.7: Channel in a Squared Domain

The problem has been studied in stationary regime, prescribing the following boundary conditions:

$$\begin{cases} \mathbf{u}_D = (0, 10)\; m/s & in\; \Gamma_D, \\ \mathbf{g} = (0, 0)\; Pa & in\; \Gamma_N. \end{cases} \tag{3.16}$$

The density and the viscosity are set, respectively to:

$$\rho = 1\ kg/m^3 \qquad \text{and}$$
$$\mu = 0.1\ kg/(m \cdot s),$$

leading to $\mathbf{Re} = 25$. The topology optimization parameters for the two values of β_R^* are summarized in Tables 3.2-3.3.

$\beta_R^* = 0$:

V_r	α_{min}	α_{max}	q	β_α	β_S	β_R	β_p
0.5	0	1e4	1	1	1	0	0

Table 3.2: Channel in a squared domain: Topology optimization parameters for $\beta_R^* = 0$ study-case.

$\beta_R^* = -2$:

V_r	α_{min}	α_{max}	q	β_α	β_S	β_R	β_p
0.5	0	1e4	1	0.34	0.34	-0.66	0

Table 3.3: Channel in a squared domain: Topology optimization parameters for $\beta_R^* = -2$ study-case.

3.4 Aortic Root Analysis

The study of the aortic root has been performed simulating the blood flow in a model geometry (see Figure 3.8), where the radius of the base and top circles are $r = 11.5mm$, and the height is set to be $h = 46mm$. The aortic sinuses are replicated according the epitrochoidal shape described by Reul et al. in 1990 [3].

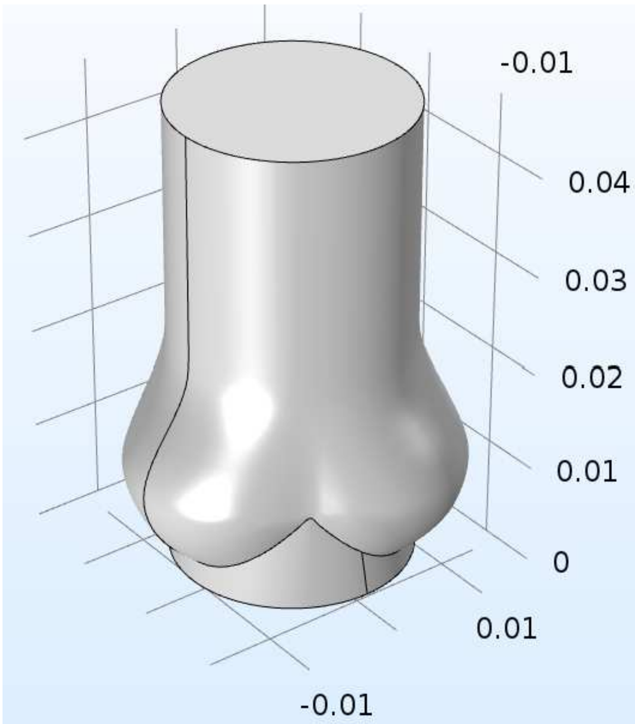

Figure 3.8: Aortic Root 3D Model

In the real case, the aortic valve is connected to the aortic root at the *annulus*, i.e. "the virtual ring formed by the basal attachments of the aortic valvular leaflets" [51] (see Figure 1.2). The aortic flowrate distribution has been considered in according with the description made by Bertelsen et al. 2016 [7] and Toninato et al. 2016 [6] (see Figure

3.9), that results into a peak velocity $\mathbf{u}_{max} = 1.5\ m/s$ at time equal to $150\ ms$.

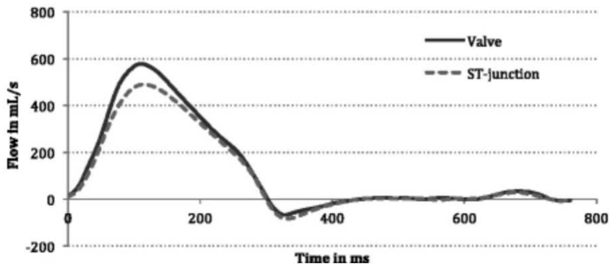

Figure 3.9: Aortic Root: Flowrate. Image from [7].

The blood flow passing through the aortic root has density and dynamic viscosity equal to $\rho = 1000\ kg/m^3$ and $\mu = 0.004\ kg/(m \cdot s)$, respectively. Being the diameter of the aorta equal to $d = 23mm$, the Reynolds number for the considered problem is

$$\mathbf{Re} = 7500. \tag{3.17}$$

The Reynolds number is defined for a fully developed flow, i.e., it is estimated at the peak velocity, $\mathbf{u}_{\text{max}} = 1.5\ m/s$. This approximation provides an idea on the computational complexity to treat the convection term in the NS equations solution, rather than describing the laminar/turbulent behaviour of the fluid.

3.4.1 The Optimization Model Geometries

To obtain an optimized domain could replicate, at least qualitatively, the Valsalva sinuses formation, it is defined an initial cylindrical domain that includes the aortic root anatomy, as modeled in 3.8. The bigger cylinder has radius equal to three times that of the aorta.
Surely, the aortic sinuses must accommodate the leaflets during the maximum flowrate phase, i.e., while they are completely open. In fact, they prevent the leaflets to continuously slap against the aorta's boundary, causing damage to both the aortic walls and the flaps themselves. Nonetheless, to continue on his path with the minimum energy losses, the blood flow exiting the left ventricle must exit the aortic root with a velocity profile with only normal component. To this purpose, the sinuses should be small enough to force the sinotubular junction to be placed close as possible to the aortic valve.
Performing a qualitative analysis on the leaflets size, this distance can be roughly (over)estimated as twice the aortic root radius. Hence, an optimal sinuses height should be greater than $h_{opt} = 23mm$. Accordingly, the external cylinder, i.e., the domain region to be shaped, is set of the same height of the supposed sinotubular junction (see Figure 3.10). The axial-symmetry of the aortic root is broken by the presence of the tri-cuspid aortic valve. Although the aorta's boundaries are made by an elastic material, the commissures, i.e. "the point of contact where two leaflets meet at the root wall" [52], must show only

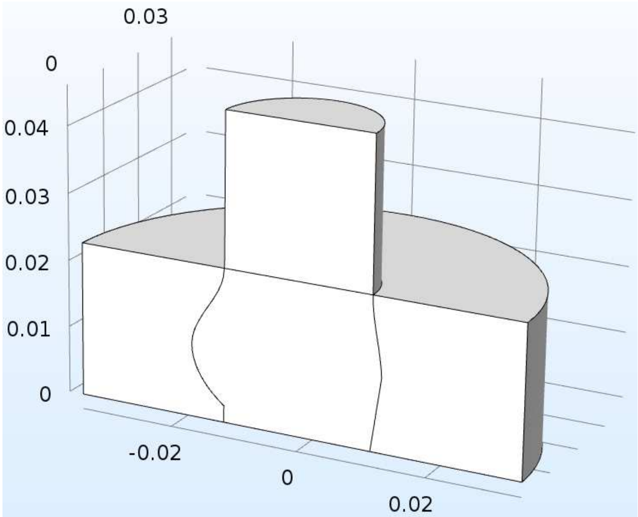

Figure 3.10: Aortic Root Optimization: 3D model domain.

small deformations during the cardiac cycle. If this were not true, during the systolic phase, the leaflets could spill over and move till touching the sinuses boundary. To avoid this unwilling phenomena, the leaflets' junctions must be bounded and fixed. This is mirrored in the performed schematization by inserting three $2r$ long surfaces, starting from the bound of the cylinder. Introducing these walls, the model is no longer axial-symmetric and fulfill the the real-case 120 symmetry scenario (see Figure 3.11).

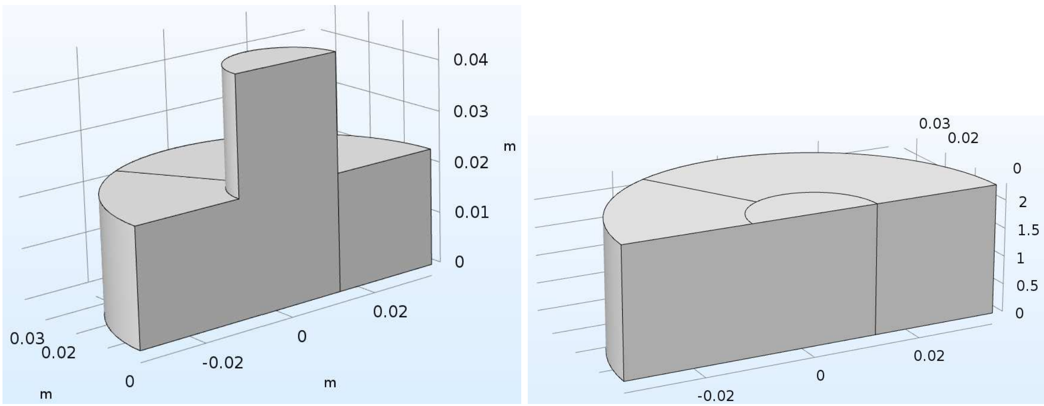

Figure 3.11: Aortic Root Optimization: 120 symmetry, 3D domain. a) full inner cylinder model; b) computational time saving model, without the upper cylinder.

Finally, to save computation time, it has been studied also an axial-symmetric 2D model. This choice allowed to perform the simulations with finer meshes avoiding numerical instabilities of the FEM at high Re values (see Figure 3.12).

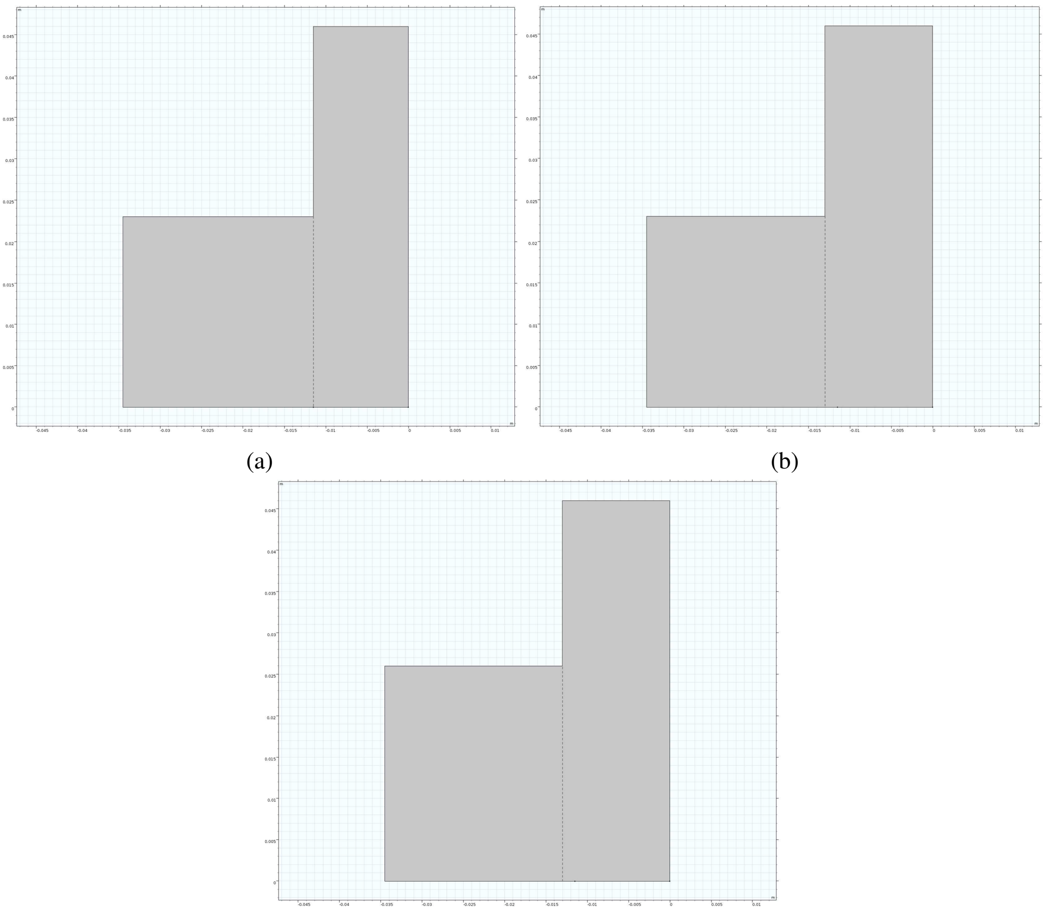

(a) (b) (c)

Figure 3.12: Aortic Root Optimization: Axial-symmetric domain, 2D model. a) physiological geometry model; b) larger upper cylinder model: r = 13mm; c) higher sino-tubular junction: h = 26mm and larger upper cylinder model: r = 13mm.

3.4.2 The Boundary Conditions

The goal of the tested boundary conditions is to reproduce different time instants of the cardiac cycle. The inlet boundary condition on the velocity has been set approximating the flowrate distribution (see Figure 3.9), re-scaled to its peak value: $1.5\ m/s$ (see Figure 3.13). The outlet is considered as an open boundary where it has been prescribed a velocity profile with only normal component.

$$\mathbf{u}_D = \begin{cases} \Big(0,0,0\Big)\ m/s, & t \in [0, 0.1], \\ \Big(0,0,1.5sin\big(\frac{\pi}{2}\cdot\frac{t-0.1}{0.05}\big)\Big)\ m/s, & t \in]0.1, 0.15], \\ \Big(0,0,1.5cos\big(\frac{\pi}{2}\cdot\frac{t-0.15}{0.2}\big)\Big)\ m/s, & t \in]0.15, 0.35], \\ \Big(0,0,0\Big)\ m/s, & t \in [0.35, 0.8], \end{cases} \qquad in\ \Gamma_D; \tag{3.18}$$

$$\mathbf{g} = \Big(0,0,0\Big)\ Pa \qquad \text{and} \qquad \mathbf{u}_{/\!/} = (0,0)\ m/s, \qquad in\ \ \Gamma_N. \tag{3.19}$$

The topology optimization study has focused on the investigation of the optimal aortic root shape in the flow rate acceleration phase. To discuss the various test-cases, four different boundary conditions, simulating the highlighted instants in Figure 3.13, have been prescribed.

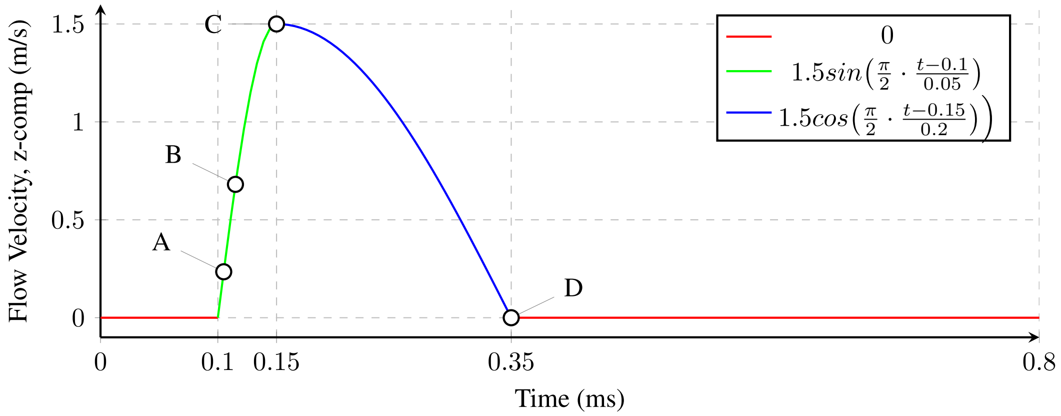

Figure 3.13: Aortic Root: Inlet velocity approximation

Here the adopted BCs are reported with their relative labels:

Type A:

This BCs simulate the initial phase of the blood flow, when the valve leaflets are opening:

$$\begin{aligned} &\mathbf{u}_D = \Big(0, 0, 1.5sin(\frac{\pi}{2} \cdot \frac{t}{0.05})\Big)\ m/s,\ t \in [0, 0.005],\ in\ \Gamma_D; \\ &\mathbf{g} = \Big(0, 0, 0\Big)\ Pa \qquad \text{and} \qquad \mathbf{u}_{/\!/} = (0, 0)\ m/s, \qquad in\ \ \Gamma_N. \end{aligned} \tag{3.20}$$

Type B:

This BCs simulate the blood flow until the valve leaflets are completely opened:

$$\begin{aligned} &\mathbf{u}_D = \Big(0, 0, 1.5sin(\frac{\pi}{2} \cdot \frac{t}{0.05})\Big)\ m/s,\ t \in [0, 0.015],\ \ in\ \Gamma_D; \\ &\mathbf{g} = \Big(0, 0, 0\Big)\ Pa \qquad \text{and} \qquad \mathbf{u}_{/\!/} = (0, 0)\ m/s, \qquad in\ \ \Gamma_N. \end{aligned} \tag{3.21}$$

Type C:

This BCs simulate the blood flow until it reaches the velocity peak:

$$\begin{aligned}&\mathbf{u}_D = \Big(0, 0, 1.5sin\big(\frac{\pi}{2} \cdot \frac{t}{0.05}\big)\Big)\, m/s,\ t \in [0, 0.05],\ in\ \Gamma_D;\\&\mathbf{g} = \Big(0, 0, 0\Big)\, Pa \qquad \text{and} \qquad \mathbf{u}_{/\!/} = (0, 0)\, m/s, \quad in\ \Gamma_N.\end{aligned} \tag{3.22}$$

Type D:

This BCs simulate until the end of the blood flow injection phase, i.e., at the end of the systole:

$$\begin{aligned}&\mathbf{u}_D = \begin{cases}\Big(0, 0, 1.5sin\big(\frac{\pi}{2}\frac{t}{0.05}\big)\Big)\, m/s,\ t \in [0, 0.05], \\ \Big(0, 0, 1.5cos\big(\frac{\pi}{2}\frac{t-0.05}{0.2}\big)\Big)\, m/s,\ t \in]0.05, 0.25],\end{cases} \qquad in\ \Gamma_D;\\&\mathbf{g} = \Big(0, 0, 0\Big)\, Pa \qquad \text{and} \qquad \mathbf{u}_{/\!/} = (0, 0)\, m/s, \qquad in\ \Gamma_N.\end{aligned} \tag{3.23}$$

3.4.3 The Test-cases

The study about the optimal aortic root design has been performed initially adopting the geometries of Figures 3.11 and 3.12, and the boundary conditions has been set, to both 3D and 2D study-cases according to the scheme of Figure 3.14.

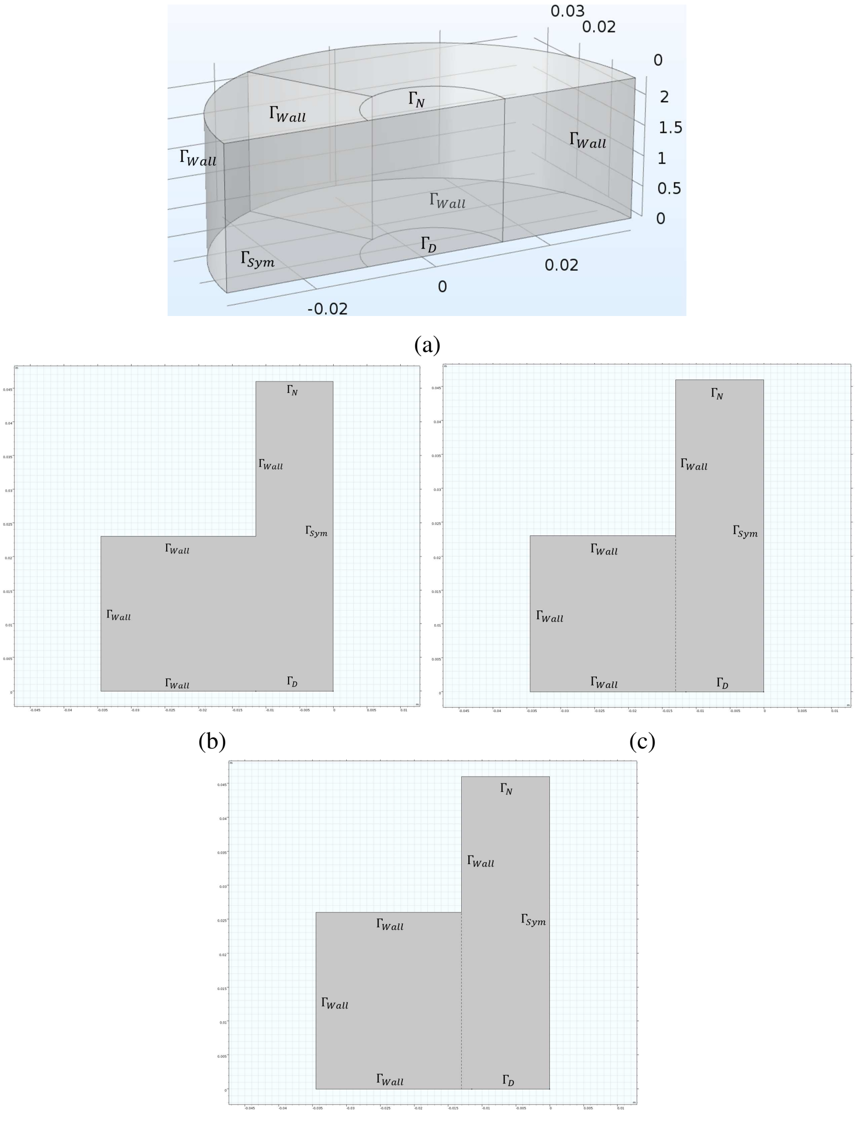

Figure 3.14: Aortic Root Optimization Model: Boundaries definition recalling Figures 3.11,3.12. a) 3D geometry boundary characterization; b),c),d) 2D geometries boundaries characterization.

Test-case 1:

Dimension: 2;

Geometry:

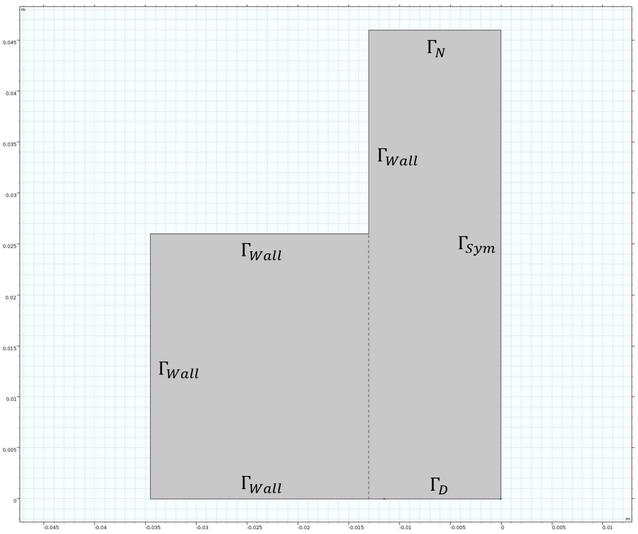

Figure 3.15: Test-case 1: Boundaries definition.

Boundary Conditions: Type A;

Topology Optimization Parameters:

V_r	α_{min}	α_{max}	q	β_α	β_S	β_R	β_p
0.6	0	1e5	1	1	1	0	0

Table 3.4: Test-case 1: Topology optimization parameters.

Test-case 2:

Dimension: 3;

Geometry:

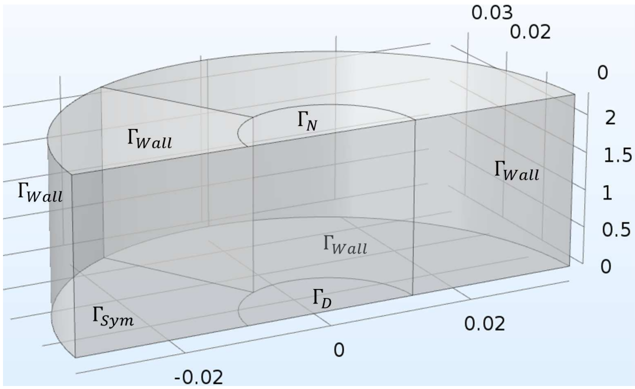

Figure 3.16: Test-case 2: Boundaries definition.

Boundary Conditions: Type A;

Topology Optimization Parameters:

V_r	α_{min}	α_{max}	q	β_α	β_S	β_R	β_p
0.3	0	1e7	1	1	1	0	0

Table 3.5: Test-case 2: Topology optimization parameters.

Test-case 3:

Dimension: 2;

Geometry:

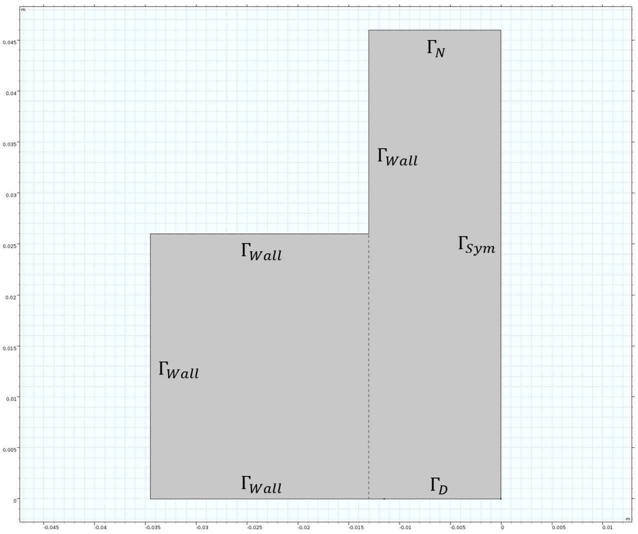

Figure 3.17: Test-case 3: Boundaries definition.

Boundary Conditions: Type B;

Topology Optimization Parameters:

V_r	α_{min}	α_{max}	q	β_α	β_S	β_R	β_p
0.6	0	1e6	1	1	1	0	0

Table 3.6: Test-case 3: Topology optimization parameters.

Test-case 4:

Dimension: 3;

Geometry:

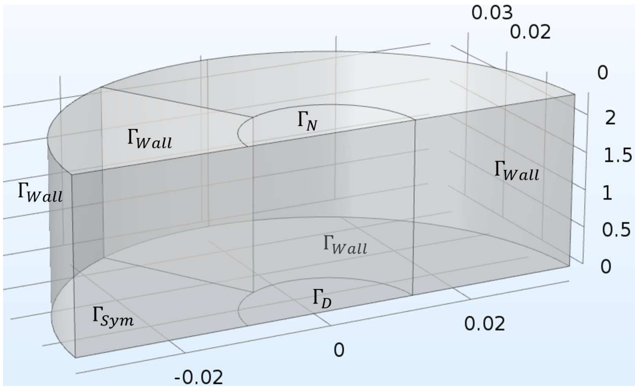

Figure 3.18: Test-case 4: Boundaries definition.

Boundary Conditions: Type B;

Topology Optimization Parameters:

V_r	α_{min}	α_{max}	q	β_α	β_S	β_R	β_p
0.3	0	1e7	1	1	1	0	0

Table 3.7: Test-case 4: Topology optimization parameters.

Test-case 5:

Dimension: 2; Geometry:

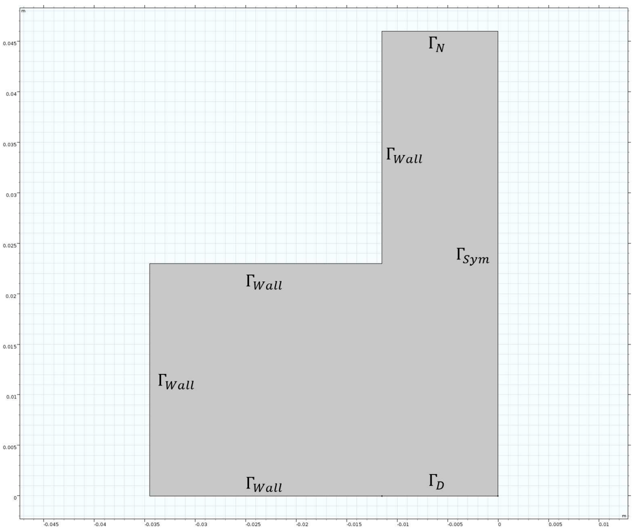

Figure 3.19: Test-case 5: Boundaries definition.

Boundary Conditions: Type C;

Topology Optimization Parameters:

V_r	α_{min}	α_{max}	q	β_α	β_S	β_R	β_p
0.6	0	1e7	1	1	1	0	0

Table 3.8: Test-case 5: Topology optimization parameters.

Test-case 6:

Dimension: 2;

Geometry:

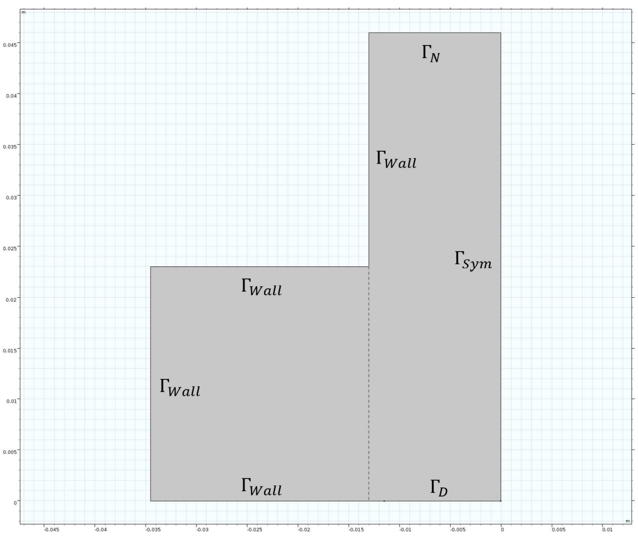

Figure 3.20: Test-case 6: Boundaries definition.

Boundary Conditions: Type C;

Topology Optimization Parameters:

V_r	α_{min}	α_{max}	q	β_α	β_S	β_R	β_p
0.6	0	1e7	1	1	1	0	0

Table 3.9: Test-case 6: Topology optimization parameters.

Test-case 7:

Dimension: 2;

Geometry:

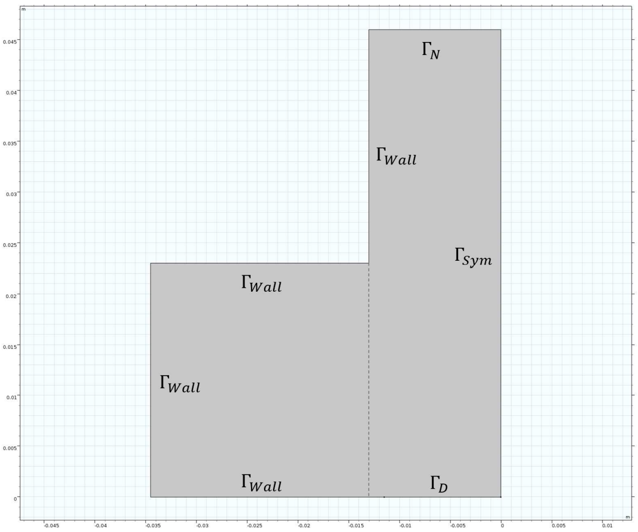

Figure 3.21: Test-case 7: Boundaries definition.

Boundary Conditions: Type C;

Topology Optimization Parameters:

V_r	α_{min}	α_{max}	q	β_α	β_S	β_R	β_p
0.6	0	1e7	1	0.5	0.5	-0.5	0

Table 3.10: Test-case 7: Topology optimization parameters.

Test-case 8:

Dimension: 2;

Geometry:

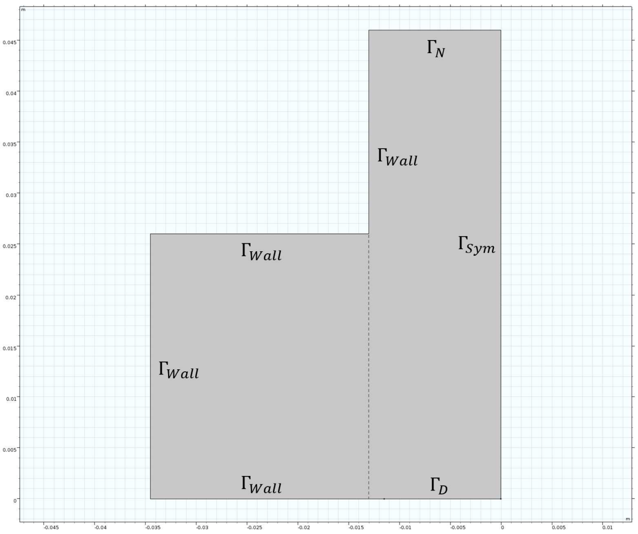

Figure 3.22: Test-case 8: Boundaries definition.

Boundary Conditions: Type C;

Topology Optimization Parameters:

V_r	α_{min}	α_{max}	q	β_α	β_S	β_R	β_p
0.6	0	1e7	1	1	1	0	0

Table 3.11: Test-case 8: Topology optimization parameters.

Test-case 9:

Dimension: 2;

Geometry:

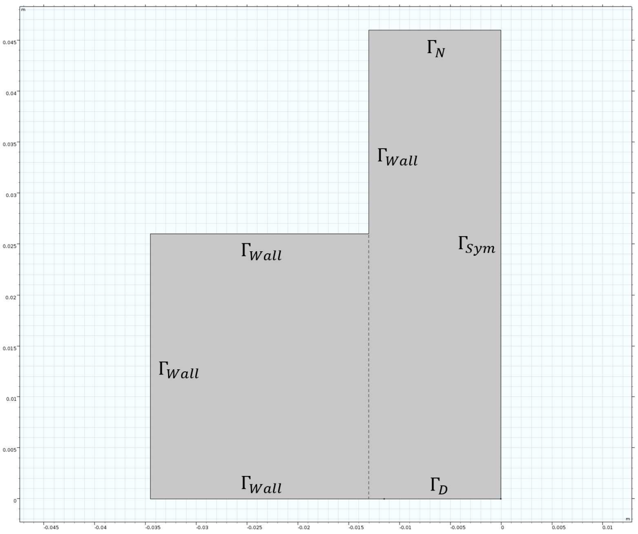

Figure 3.23: Test-case 9: Boundaries definition.

Boundary Conditions: Type D;

Topology Optimization Parameters:

V_r	α_{min}	α_{max}	q	β_α	β_S	β_R	β_p
0.6	0	1e7	1	1	1	0	0

Table 3.12: Test-case 9: Topology optimization parameters.

Chapter 4

Results and Conclusions

4.1 Preliminary Study-cases

In this section the topological optimization solution obtained in the preliminary study-cases are presented and then discusses.

4.1.1 Oblique Plate in a Rectangular Domain: Results and Discussion

The study cases investigate on the effect of the flow inertia variation over the optimal domain shape.
The optimization parameter evolution follows the same behaviour in all the considered cases (see Figures 4.1, 4.2 and 4.3). Starting from an homogeneous design parameter distribution, the latter evolves avoiding the higher fluid rotation regions, in according with the minimization of the deformation term of the functional defined in 3.6.

Case $\mathrm{Re} = 1$:

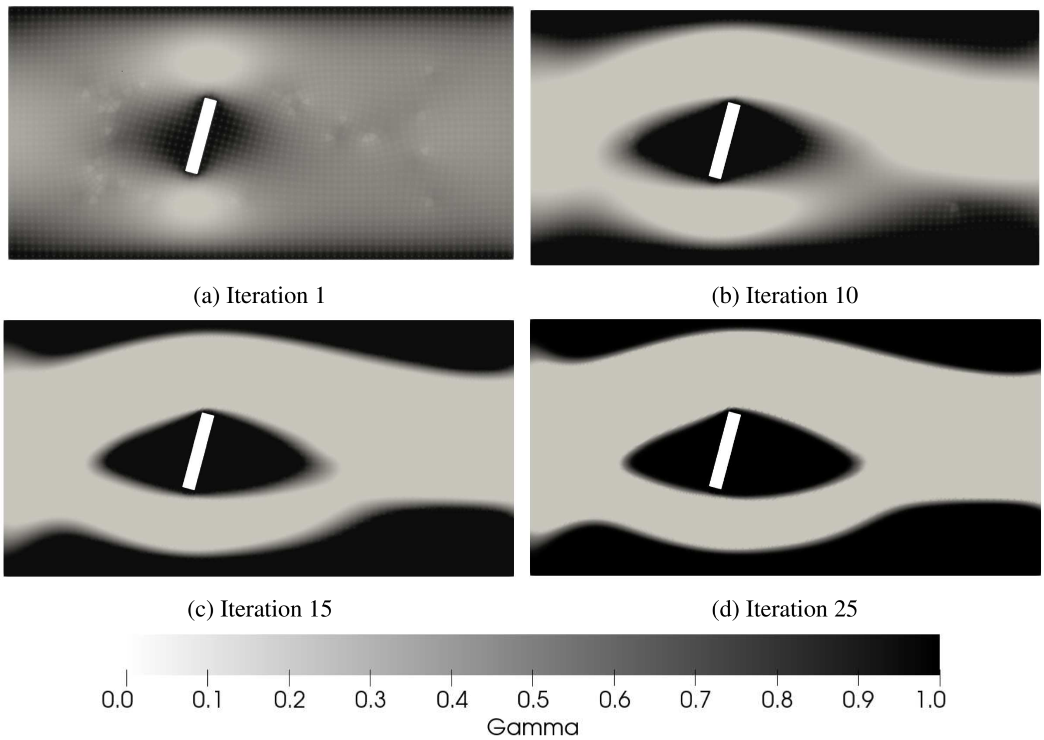

(a) Iteration 1 (b) Iteration 10

(c) Iteration 15 (d) Iteration 25

Figure 4.1: Oblique Plate in a Rectangular Domain: $\mathbf{Re} = 1$

Case $\mathbf{Re} = 100$:

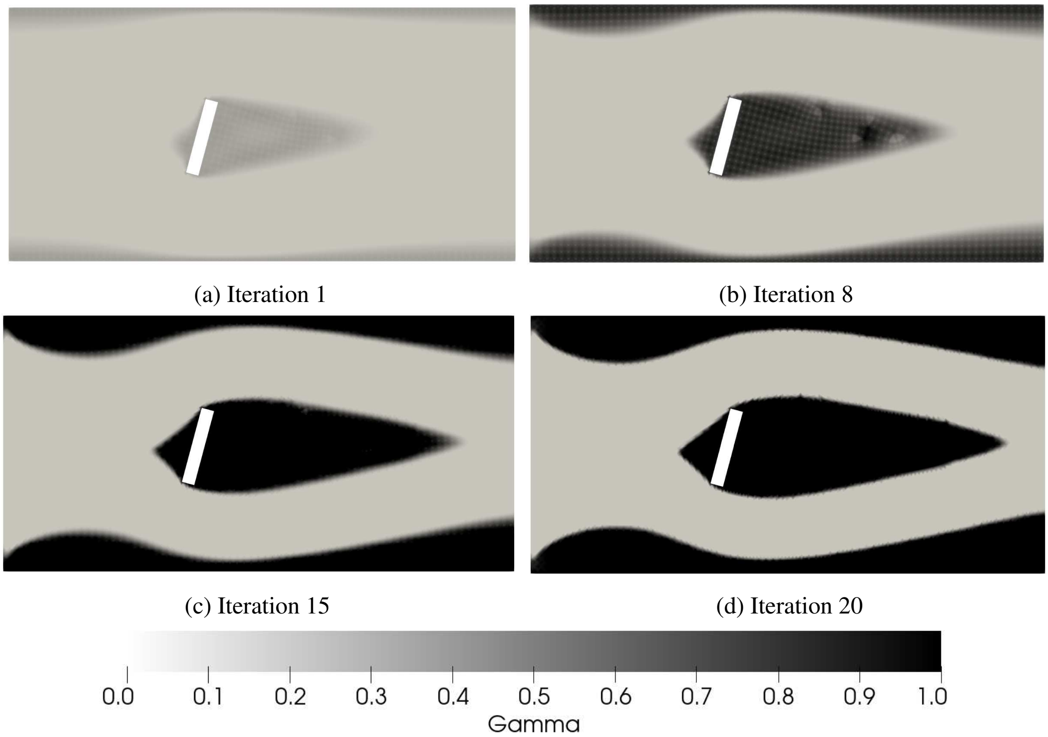

Figure 4.2: Oblique Plate in a Rectangular Domain: $\mathbf{Re} = 100$

Case $\mathbf{Re} = 1000$:

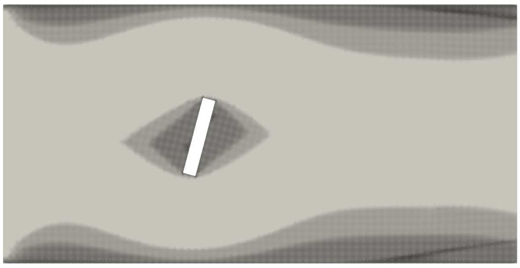

(a) Iteration 1

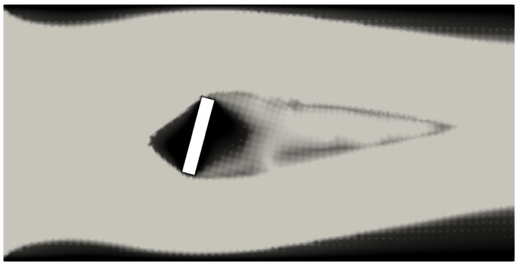

(b) Iteration 10

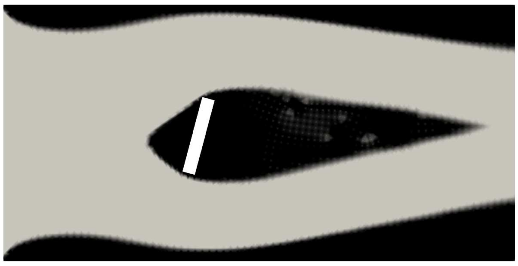

(c) Iteration 20

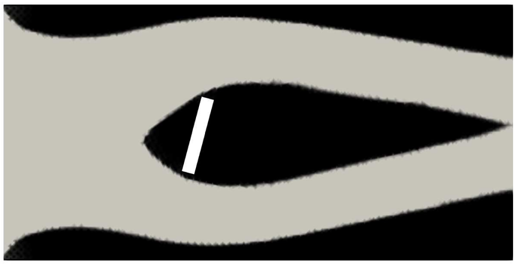

(d) Iteration 27

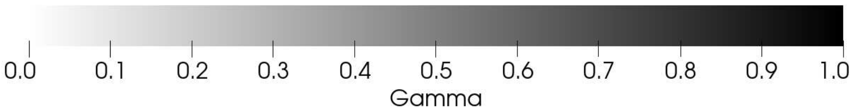

Figure 4.3: Oblique Plate in a Rectangular Domain: $\mathbf{Re} = 1000, \alpha_{max} = 1e5$

The increase of $\mathbf{Re}$, i.e., the increase of the flow inertia, demonstrates to have a clear impact on the final configuration (see Figures 4.1, 4.2, and 4.3). The optimized geometry has to avoid the formation of vortices, which highly dissipate the bulk flow energy.

For the highest analysed Reynolds number($\mathbf{Re} = 1000$), the density method for topology optimization suffers some convergence issues. A too little value of α_{max} can lead the optimal configuration to converge to a non "discrete" solution and the fluid passes through low-porosity regions with a non negligible velocity magnitude. Therefore, for high $\mathbf{Re}$, the value of α_{max} should be increased. However, increasing the maximum value of the forcing $\mathbf{f}_\alpha$ could create numerical instabilities, e.g., the "check-board effect" [46] (see Figure 4.4). Hence, its value must be chosen to balance these drawbacks.

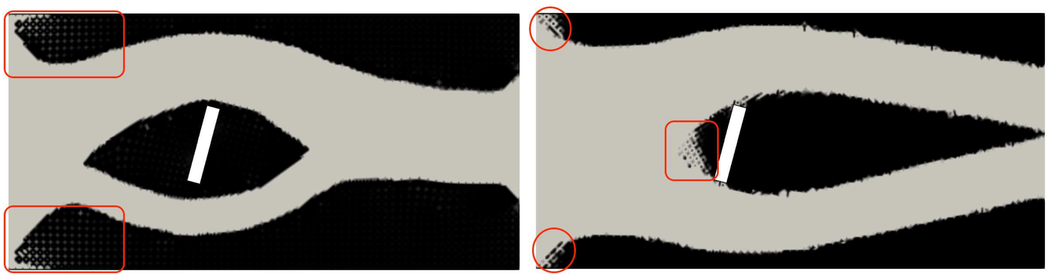

(a) $\mathbf{Re} = 1,\ \alpha_{max} = 1e7$

(b) $\mathbf{Re} = 1000,\ \alpha_{max} = 1e7$

Figure 4.4: Check-board Effect

For these reasons, the final comparison between the optimal shapes has been performed setting $\alpha_{max} = 10^5$ only for the highest Reynolds number scenario.

In conclusion, given that for the considered functional (see Table 3.1) $(\beta_R^*, \beta_p^*) = (0, 0)$, the optimal shape is expected to minimize the symmetric part of the velocity gradient tensor, i.e., the deformation of the group of streamlines (see Figure 4.5).

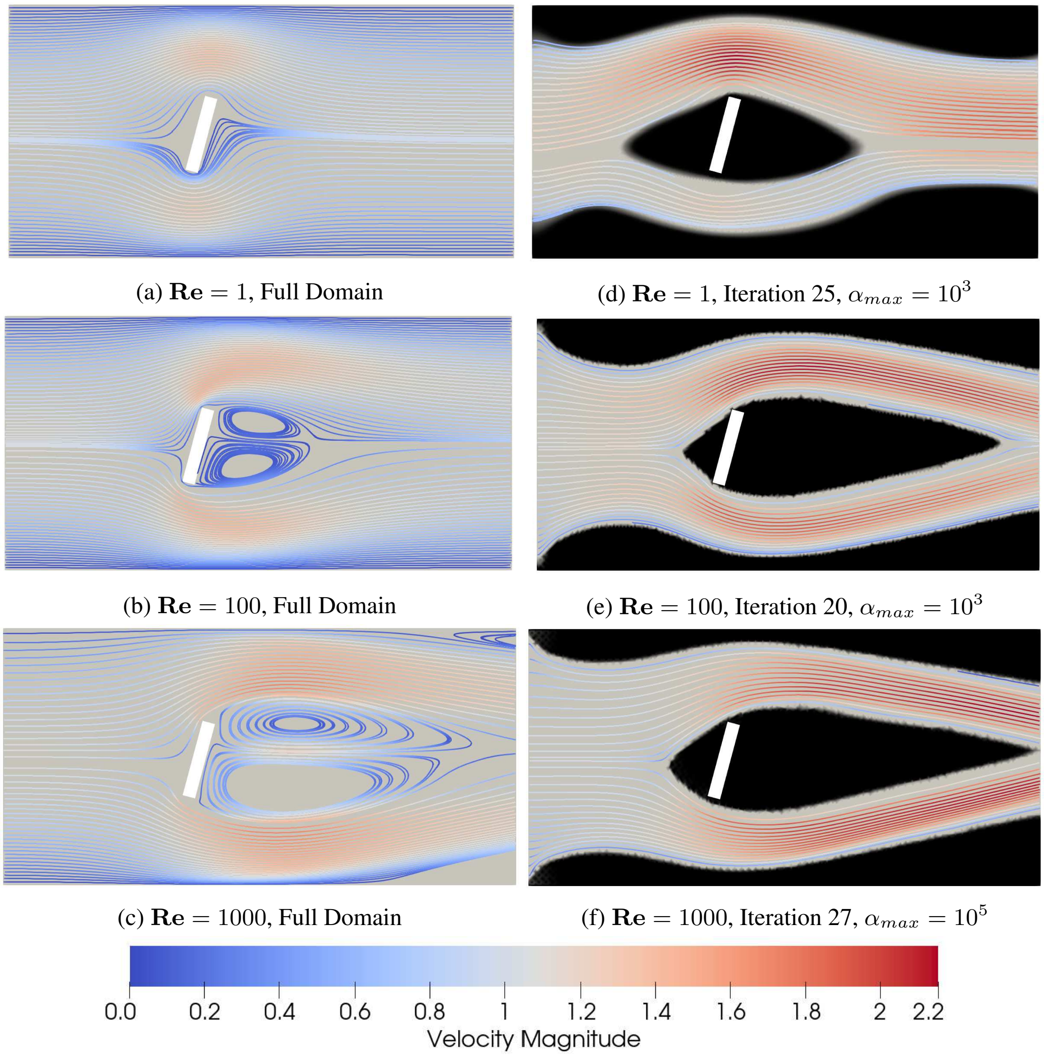

Figure 4.5: Oblique Plate in a Rectangular Domain: Streamlines. a),b),c) streamlines in the free initial geometry, respectively with $\mathbf{Re} = 1$, $\mathbf{Re} = 100$, and $\mathbf{Re} = 1000$; d),e),f) streamlines in the optimal domain shape, respectively with $\mathbf{Re} = 1$, $\mathbf{Re} = 100$, and $\mathbf{Re} = 1000$

The functional value behaviour over the algorithm iterations has the same qualitative representation for all the three studied cases. Looking at Figures 4.6, 4.7 and 4.8, the functional values seems to have a sort of parabolic distribution. In the first iterations the functional value is increased in order to restrict the fluid domain to a feasible one. Once the latter has been found, in the subsequent iterations the geometry minimizes the energy dissipation keeping active, i.e. verified, the volume constraint.

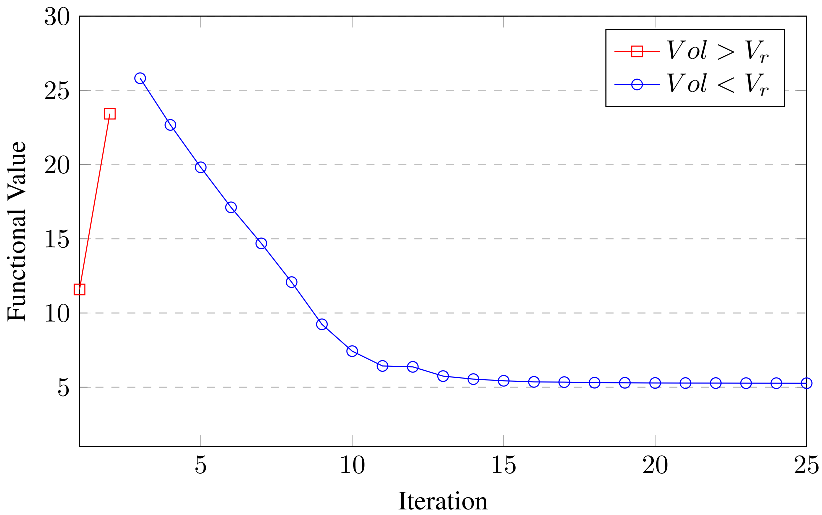

Figure 4.6: Oblique Plate in a Rectangular Domain, $\mathbf{Re} = 1$: Functional

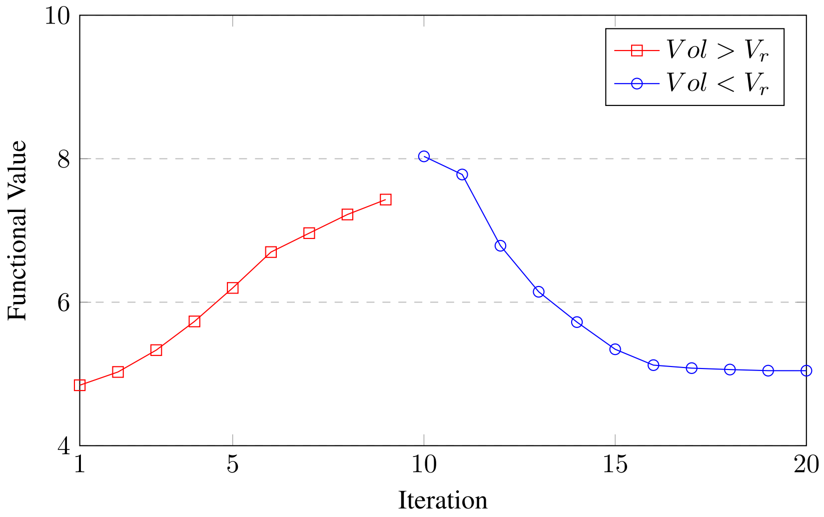

Figure 4.7: Oblique Plate in a Rectangular Domain, $\mathbf{Re} = 100$: Functional

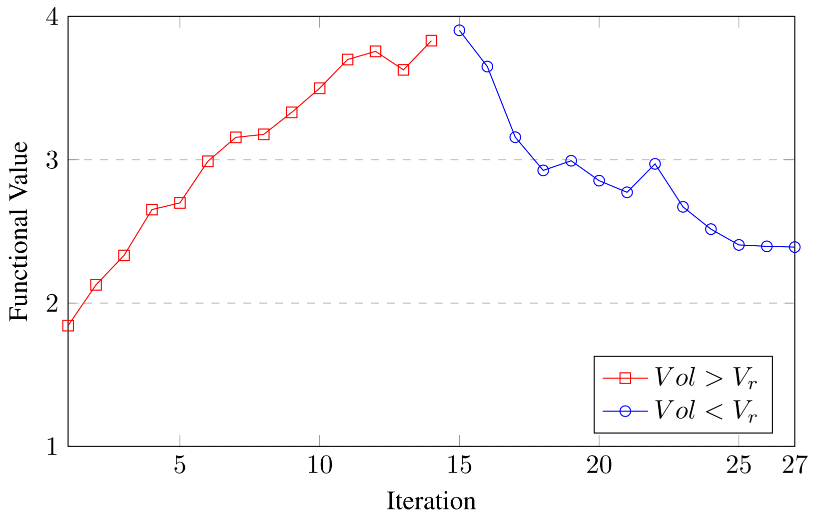

Figure 4.8: Oblique Plate in a Rectangular Domain, $\mathbf{Re} = 1000$: Functional

4.1.2 Channel in a Squared Domain: Results and Discussion

The channel in a squared domain problem has been implemented to study the newly introduced vorticity term in the functional J 3.6.
The optimization parameter evolution follows a completely different behaviour in the two considered cases (see Figures 4.9 and 4.10). Starting from a similar design parameter distribution at it.1, already in the fifth iteration the distribution has a different representation. In the $\beta_R^* = 0$ case, in fact, the there is a big central barrel-like shape, while in the $\beta_R^* = -2$ study the optimization geometry is reduced to a central cylinder. In the following iteration the evolution of γ follows opposite paths. When $\beta_R^* = 0$, the optimization erodes the first iterations shape until it reaches a feasible configuration, i.e., it respect the volume constraint, without modifying the core of the shape. In the $\beta_R^* = -2$ case, instead part of the flow is conveyed through a straight channel; however another two lateral channels, from the inlet flow along the boundary drive the flow to the outlet.

Case $\beta_R^* = 0$:

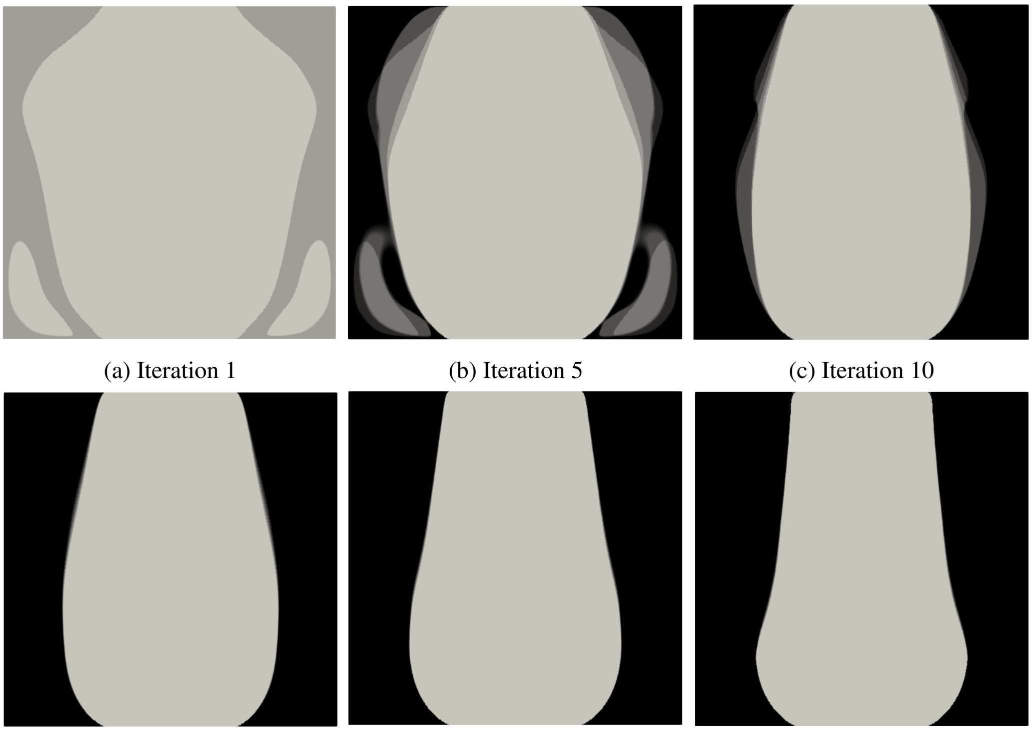

(a) Iteration 1 (b) Iteration 5 (c) Iteration 10

(d) Iteration 15 (e) Iteration 30 (f) Iteration 50

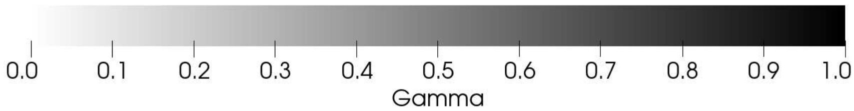

Figure 4.9: Channel in a Squared Domain: $\beta_R^* = 0$. Design parameter evolution.

Case $\beta_R^* = -2$:

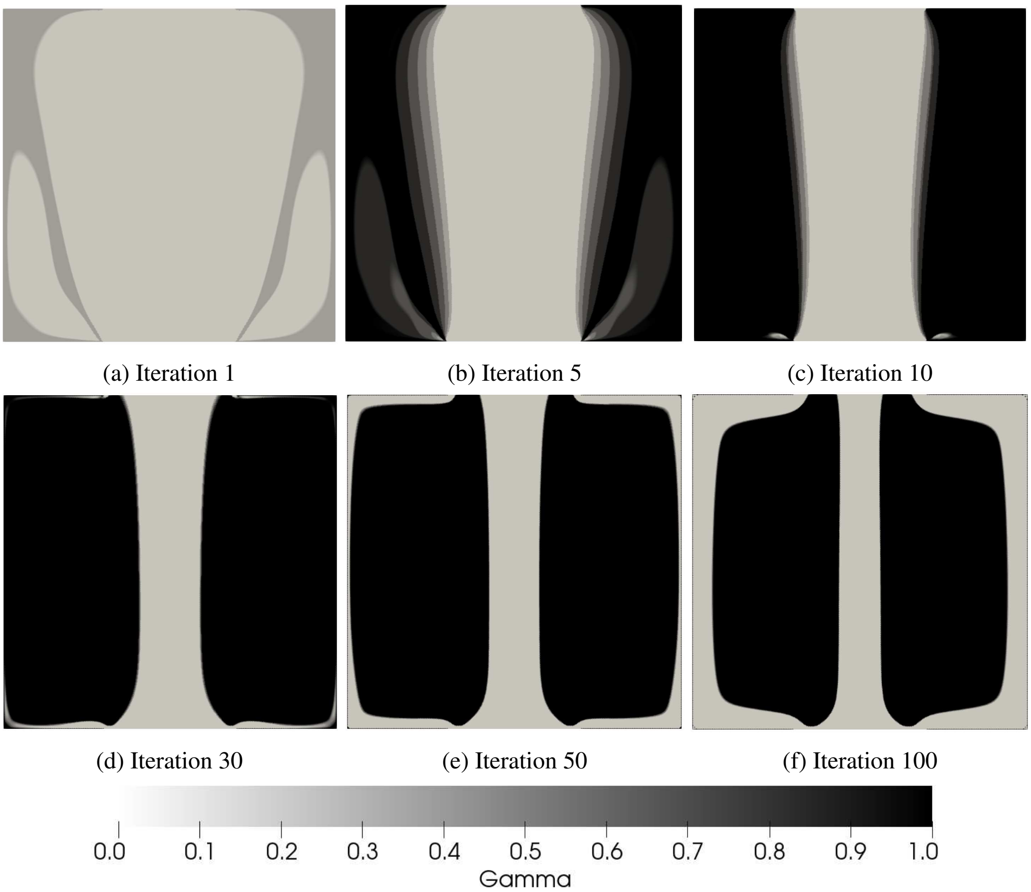

(a) Iteration 1 (b) Iteration 5 (c) Iteration 10

(d) Iteration 30 (e) Iteration 50 (f) Iteration 100

Figure 4.10: Channel in a Squared Domain: $\beta_R^* = -2$. Design parameter evolution.

The design parameter evolution comparison shows, as expected, a strong dependence of the final configurations with respect to the objective functional formulation.

The optimal shape maximizing the anti-symmetric part of the velocity gradient performs a reorganization of the material distribution throughout the domain. However, also in this case, the contribution of the symmetric part of the velocity gradient can still be observed; in fact, even if constraining the lateral part of the optimal flow to curve, the optimal domain topology avoids the formation of vortices (see Figure 4.11).

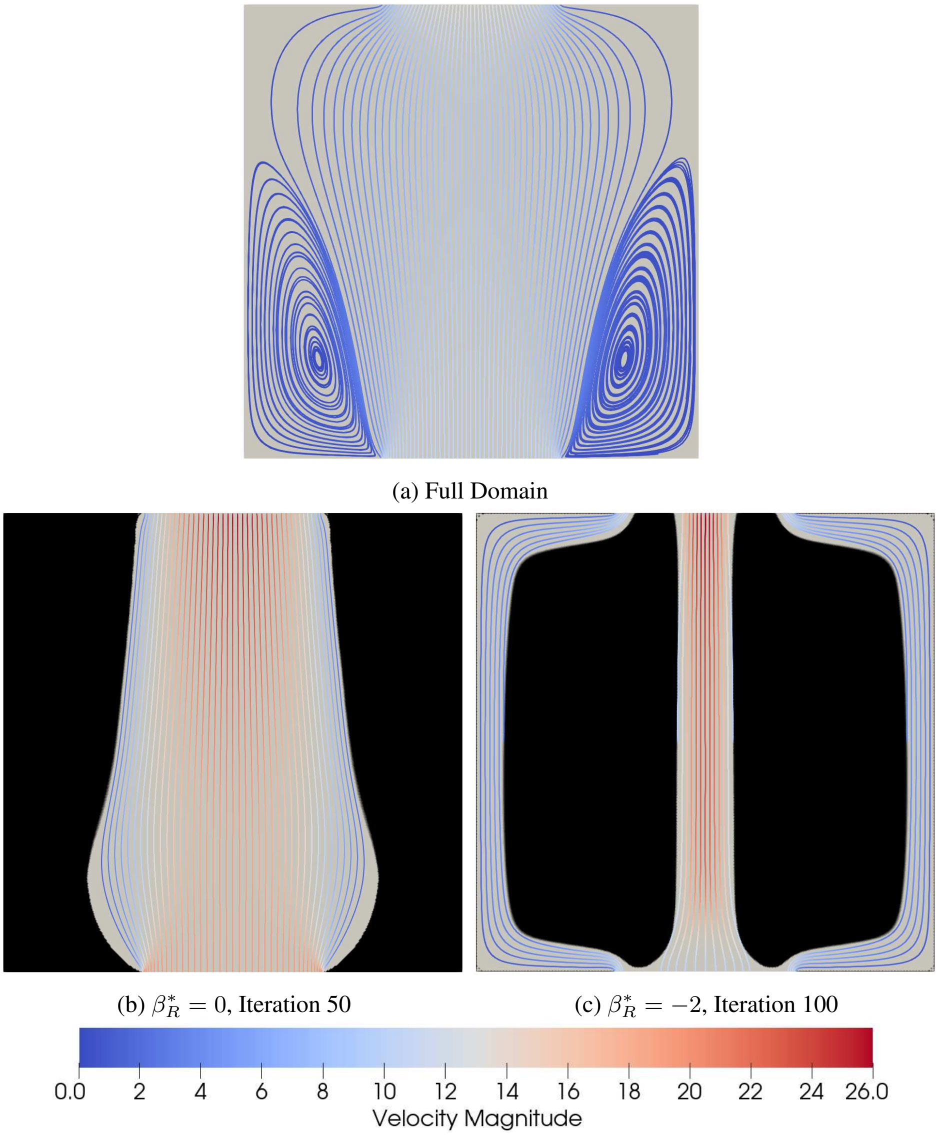

Figure 4.11: Channel in a Squared Domain: Streamlines. a) streamlines in the free initial geometry; b) streamlines in the optimal domain shape 4.9, with $\beta_R^* = 0$; b) streamlines in the optimal domain shape 4.10, with $\beta_R^* = -2$;

The functional value over the optimization iterations has a relevant behaviour in this study-case. Looking at the Figure 4.12 it can be observed that, setting a negative value for the β_R functional weight, the maximization of the vorticity term is correctly performed through the minimization of the functional J, leading it to have also negative values.

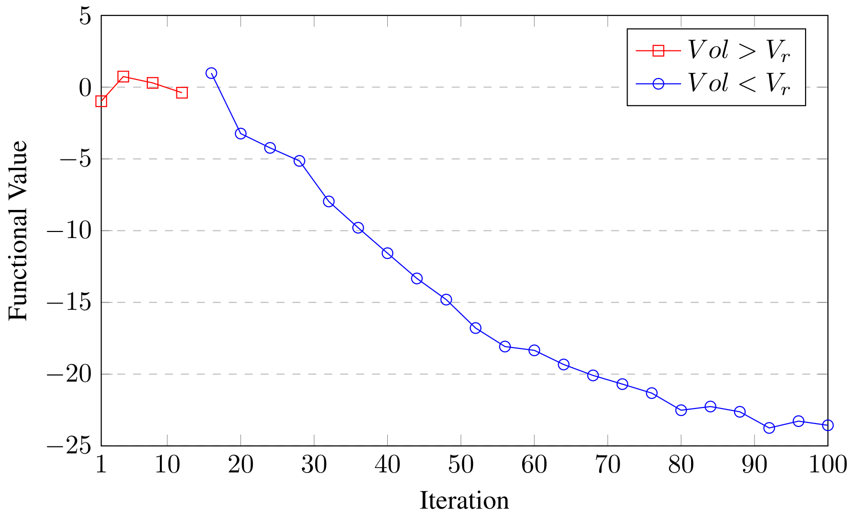

Figure 4.12: Channel in a squared domain, $\beta_R^* = -2$: Functional Analysis

4.2 Aortic Root Results

Test-case 1:

The design parameter evolution in Figure4.13 shows the formation of a bulge-like aortic root profile. Starting from the iteration 70, the optimized domain shows an almost discrete distribution of γ, constraining the streamlines to flow only inside the non-solid portion of the domain (see Figure 4.14).

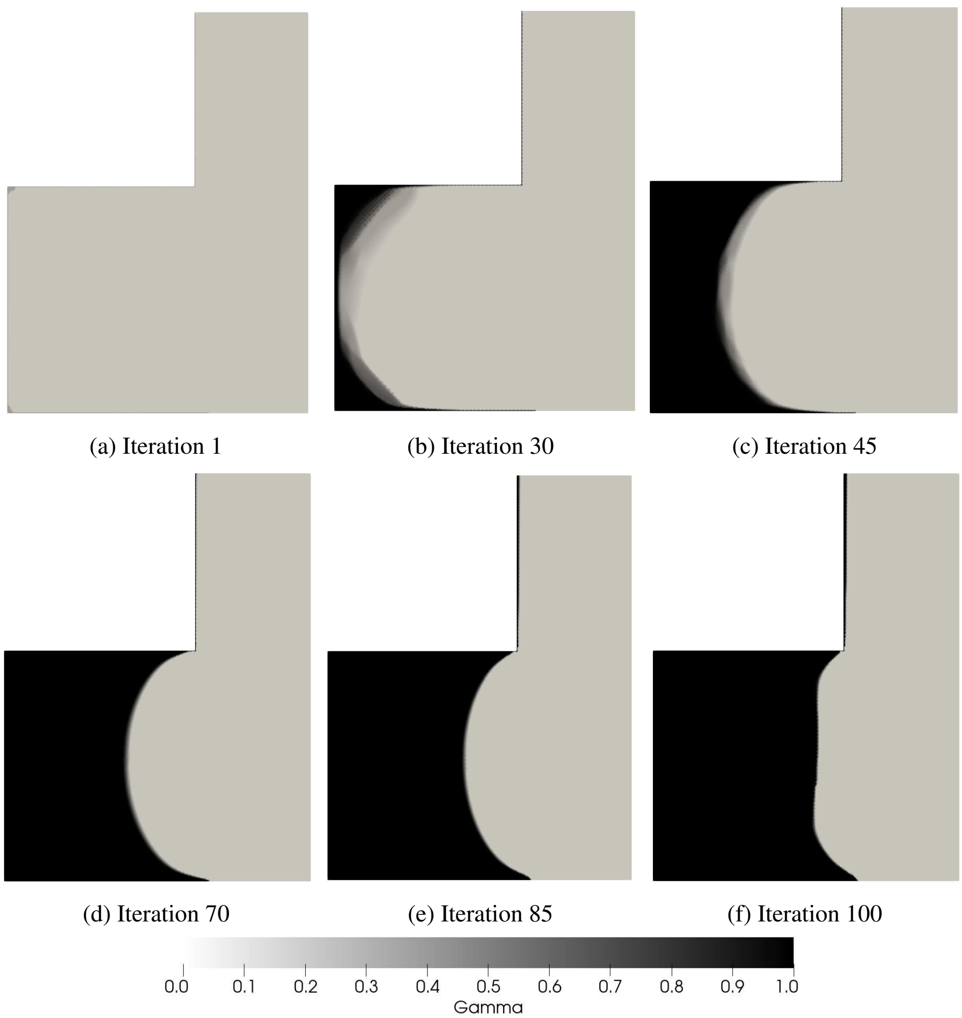

Figure 4.13: Test-case 1: Design Parameter Evolution

The maximun velocity magnitude achieved by the flow in the optimal domain shape is approximately $|u|_{\text{max}} = 0.3\ m/s$, leading to a Reynolds number maximum value of $\mathbf{Re} \simeq 1500$. Moreover, since the simulation has been performed imposing boundary conditions of type A, the final time is $t = 0.005\ s$; such a little time variable domain does not allow the formation of vortices inside the prescribed geometry in any of the optimization procedure iterations. Hence, the bulges function is just to minimize the pressure at the side boundaries, diminishing the velocity magnitude value by letting the streamlines to perform a little rotation.

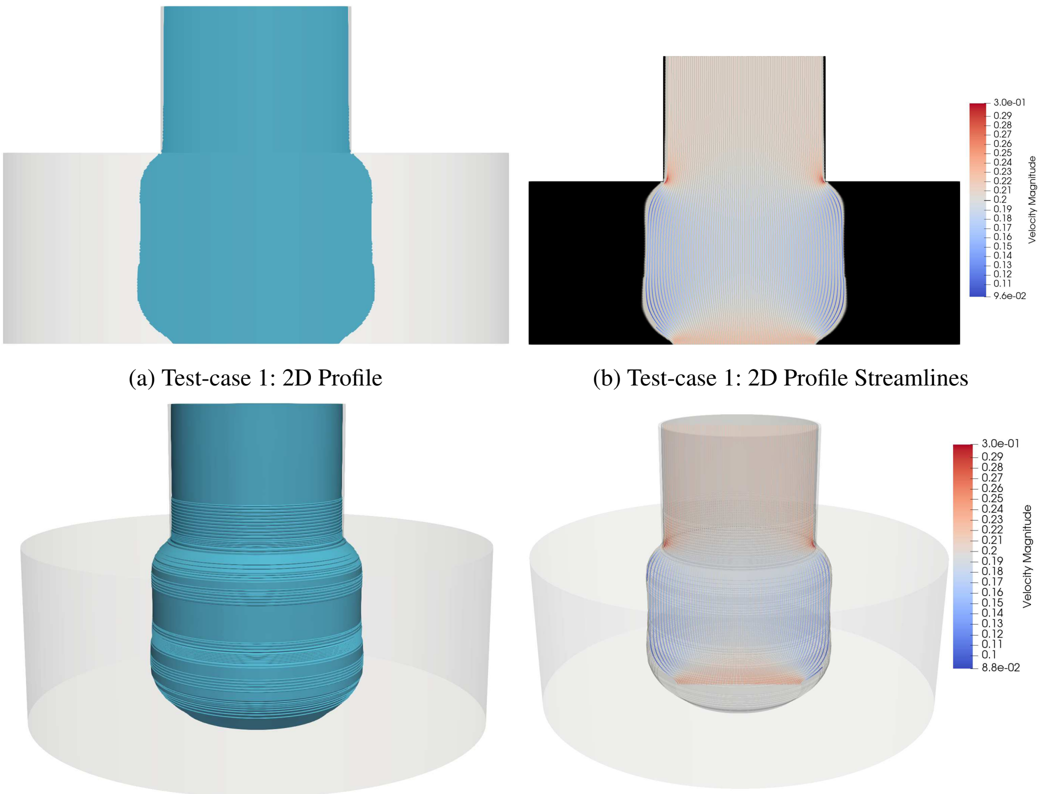

(a) Test-case 1: 2D Profile

(b) Test-case 1: 2D Profile Streamlines

(c) Test-case 1: 3D Profile

(d) Test-case 1: 3D Profile Streamlines

Figure 4.14: Test-case 1: Optimal Domain

Test-case 2:

This test case was performed replicating the same boundary condition, and topology optimization parameters as the test-case 1, breaking the axial-symmetry by switching the domain of analysis to a three-dimensional geometry (see Figure 3.16). Despite the presence of the wall interfaces 3.11, the optimal design parameter evolution replicated the same behaviour of the axial-symmetric case. Hence here it is reported only the optimal domain shape (see Figure 4.15).

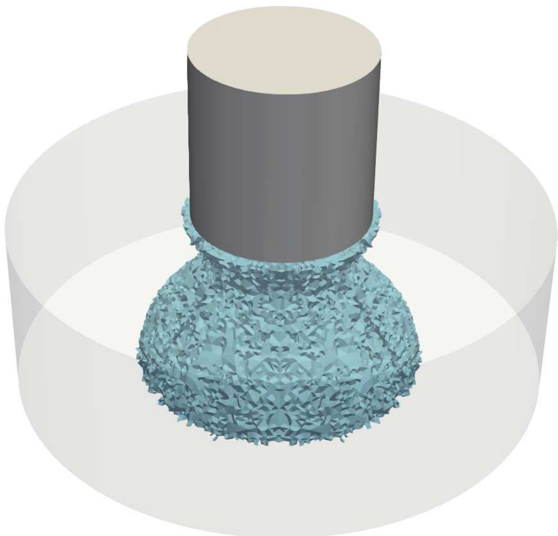

Figure 4.15: Test-case 2: Optimal Domain

A further analysis on the inefficiency of the 120-symmetrical wall interfaces will be developed in the general discussion 4.3.

Test-case 3:

The design parameter evolution in Figure 4.16 shows the formation of a bulge-like aortic root profile, like in the first test-case (see Figure 4.13). However, the optimal domain shape has a slightly different behaviour than the test-case 1 solution; in fact, in this study-case, the bulge has more rounded shape that lets the flow to perform a stronger rotation in order to lower the stresses on the side boundaries (see Figure 4.17).

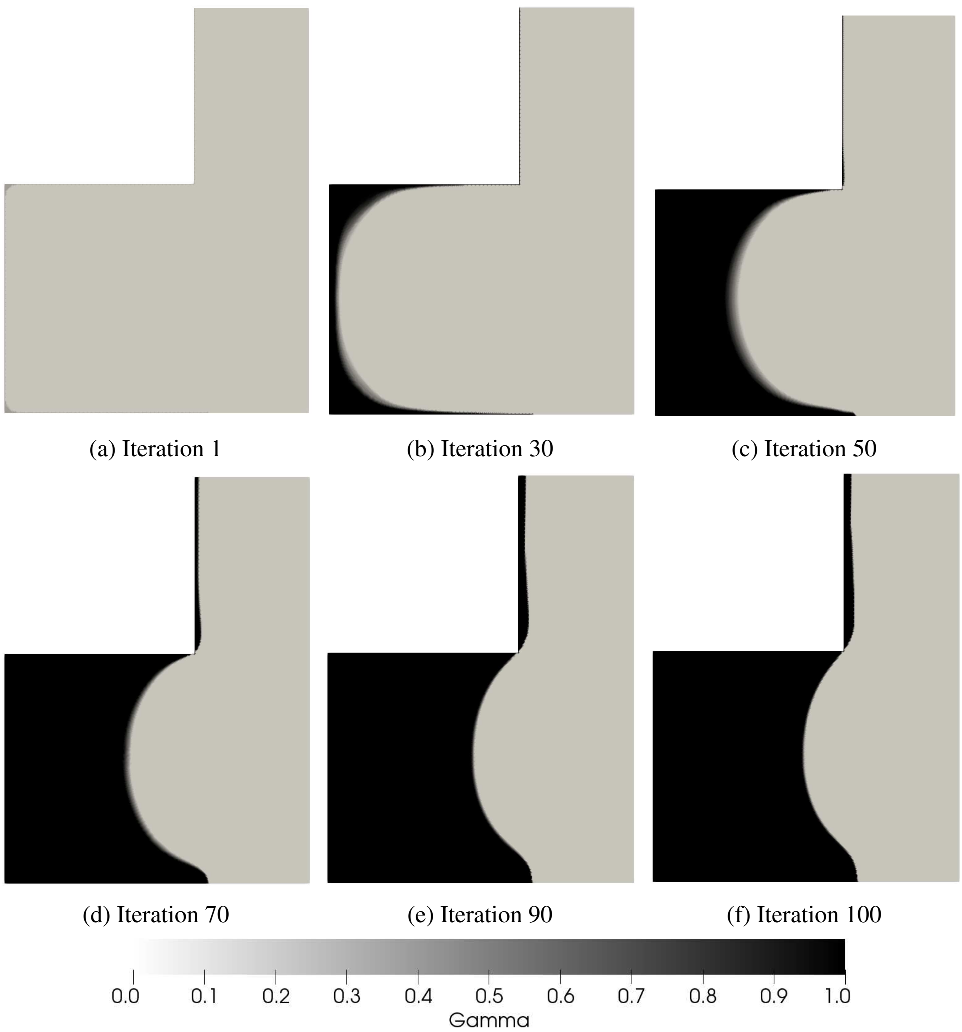

Figure 4.16: Test-case 3: Design Parameter Evolution

Despite the fact that, prescribing BC of type B, the maximum value of the velocity magnitude, $|u|_{\text{max}} = 0.81\ m/s$, leads to $\mathbf{Re} \simeq 4000$, similarly to the test-case 1, the optimal geometry streamlines does not shows the presence of any vortex, probably because of the small value of the ending time, i.e., $t_{end} = 0.015s\ s$.

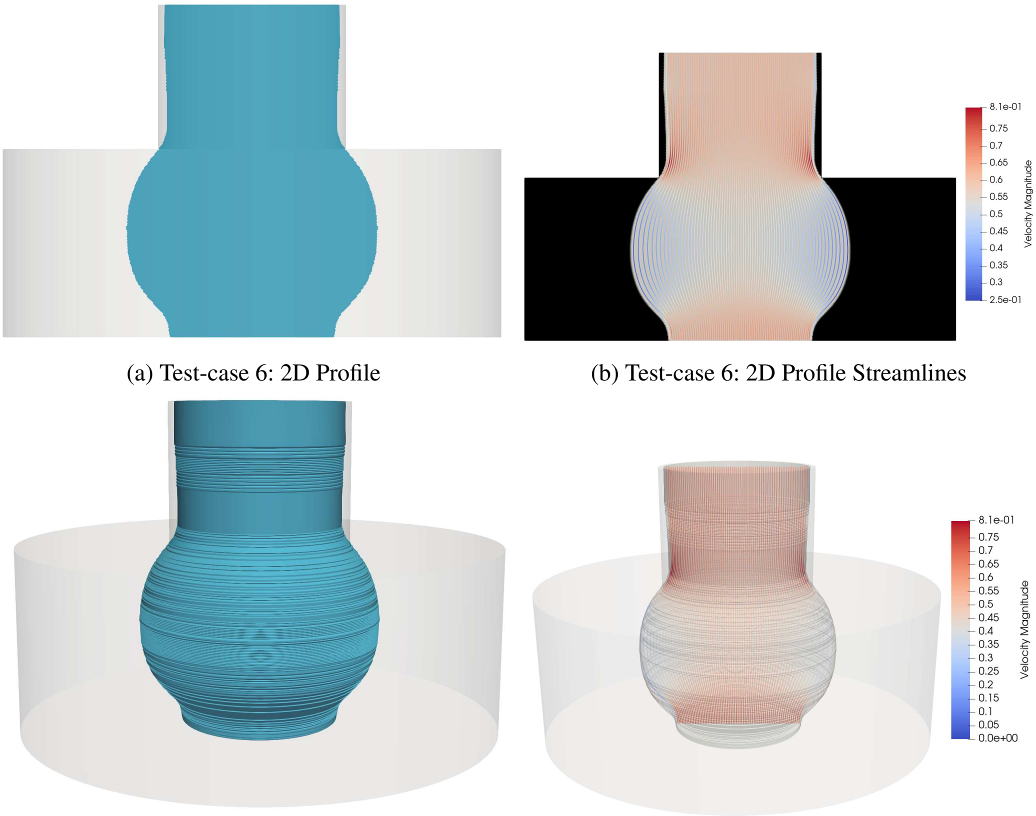

(a) Test-case 6: 2D Profile

(b) Test-case 6: 2D Profile Streamlines

(c) Test-case 6: 3D Profile

(d) Test-case 6: 3D Profile Streamlines

Figure 4.17: Test-case 3: Optimal Domain

Also in this case, starting from the iteration 70, the optimized domain shows an almost discrete distribution of γ (see Figure 4.17).

The functional value evolution over the optimization algorithm iterations in Figure 4.18 shows that the it.70 is exactly the one where the volume constraint is satisfied for the first time. In the subsequent iterations it occurs only a little reduction of the functional value, in according with the little variation of the design parameter distribution (see Figures 4.16 and 4.18).

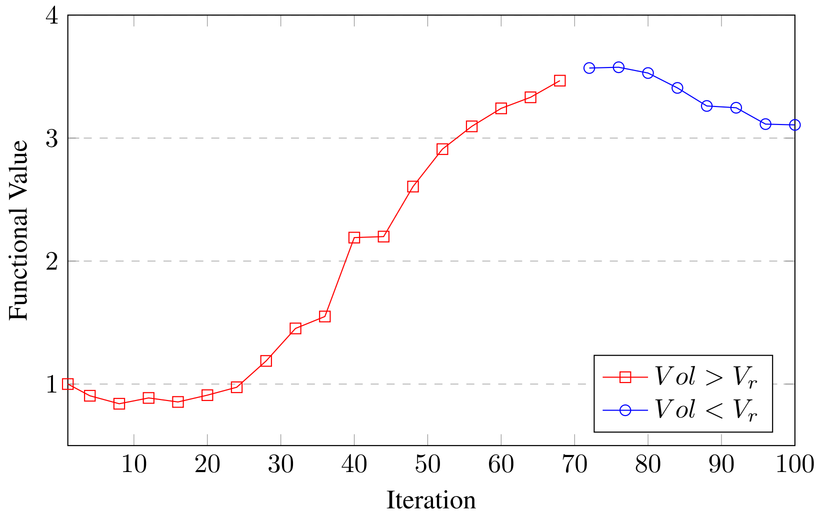

Figure 4.18: Test-case 3: Functional Value over 100 Iterations

Test-case 4:

This test has been performed with the same idea of test-case 2: replicating the same boundary condition and topology optimization parameters as the axial-symmetrical test-case, test-case 3, and breaking the axial-symmetry by switching the domain of analysis to a three-dimensional geometry (see Figure 3.18). Also in this 3D simulation, the presence of the wall interfaces 3.11 has been ignored by the optimal design parameter evolution; it replicated the same behaviour of the test-case 3 with the addition of three empty surfaces in correspondence of the inserted walls. Hence here it is reported only the optimal domain shape (see Figure 4.19).

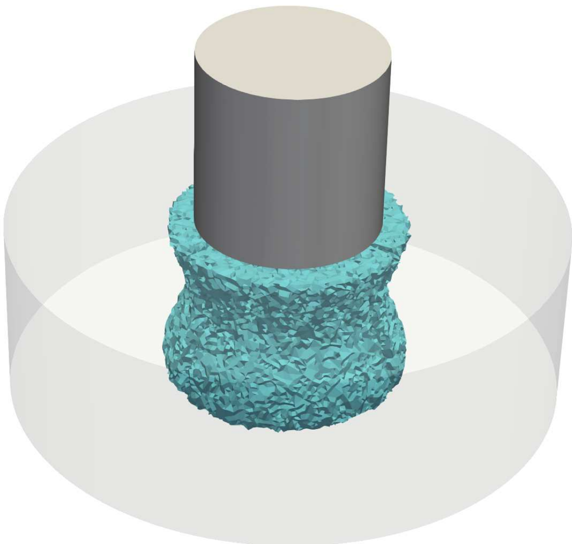

Figure 4.19: Test-case 4: Optimal Domain

A further analysis on the inefficiency of the 120-symmetrical wall interfaces will be developed in the general discussion 4.3.

Test-case 5:

The goal of this study case was to perform a first simulation with boundary conditions of type C, in order to understand if, in presence of vortices, the optimization procedure required some variations on the initial geometry to provide an optimal domain similar to the the aortic root shape. The design parameter evolution in Figure4.20 shows the formation of a bulge-like aortic root profile. However, differently from the test-cases 1 and 2, starting from it.80 the optimal domain shape seems to provide a qualitative replication of the Valsalva sinuses. The bulge starts after a little gap with the inlet, and develops a well rounded shape that closes in correspondence of the imposed sino-tubular junction.

In the upper part of the central cylinder, to avoid the re-circulation, and then the formation vortices, the optimal geometry narrows the diameter (see Figure 4.20e). To compensate this effect, in the following test-cases, the simulations have been performed increasing the diameter of the outlet by $3mm$.

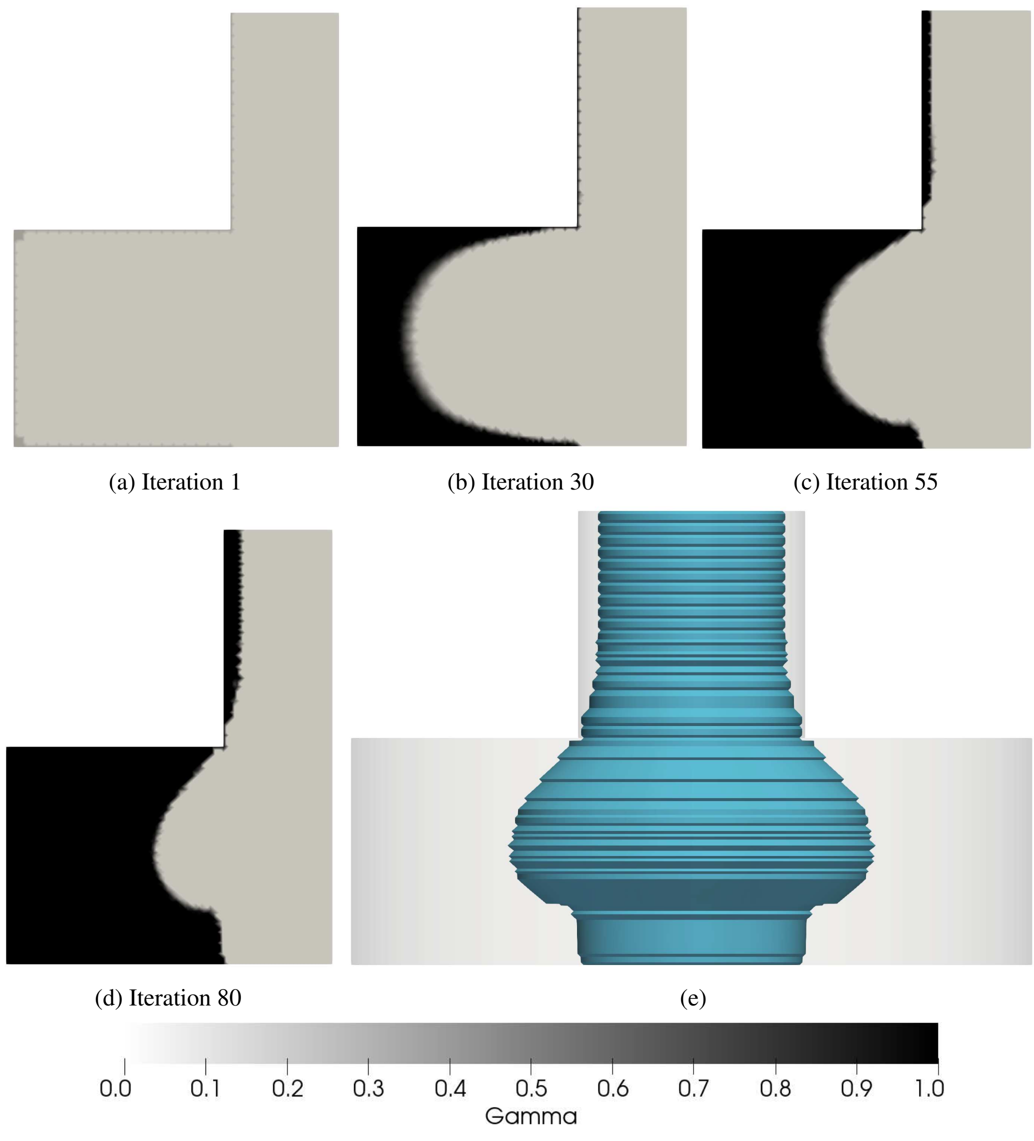

Figure 4.20: Test-case 5: Design Optimization. a),b),c),d) Design parameter evolution; e) Optimal Shape.

Test-case 6:

According to the results of the test-case 5, the outlet diameter has been increased by $3mm$, $d_{outlet} = 26mm$.
The optimal design parameter of Figure 4.21 replicates the one of the previous test-case solution. In fact, it can be observed the formation of a bulge, which is able to contain the streamlines vortices during the peak velocity instants, $|u|_{\max} = 1.5\ m/s$. Such $|u|_{\max}$ value leads to $\mathbf{Re} \simeq 7500$, that, considering a time-domain with $t_{end} = 0.05ms$, match the correct conditions to the formation of a vortex ring near the inlet that propagates over time, till it reaches the center of the optimization domain height. The optimal domain shape bulges seems to play the role of a suitable container for the flow vortices, avoiding the fluid energy dissipation with the side boundaries (see Figure 4.21e).
Looking at the streamlines in Figure 4.21 it can be observed that, since the optimal configuration does not let the energy dissipate, thanks to the restriction of the domain volume and the presence of vortices inside the bulges, the maximum flow velocity magnitude is greater of the injected one, reaching a peak value of $|u|_{opt_{\max}} \simeq 1.7\ m/s$.

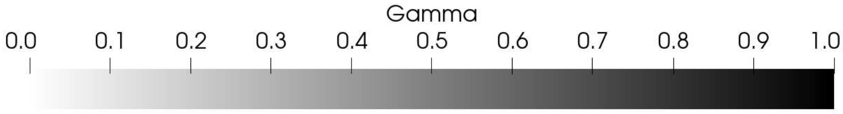

(a) Iteration 1

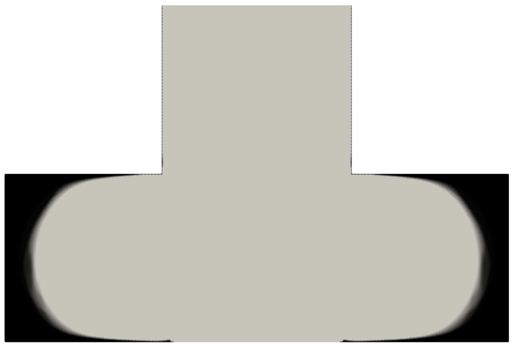

(b) Iteration 30

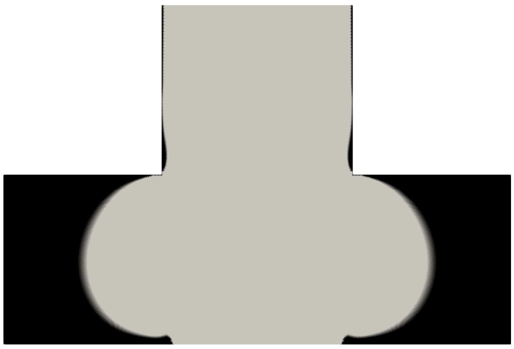

(c) Iteration 50

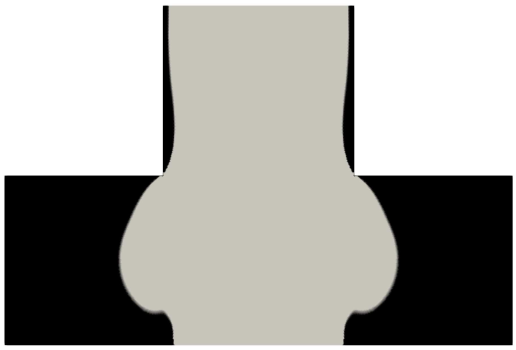

(d) Iteration 80

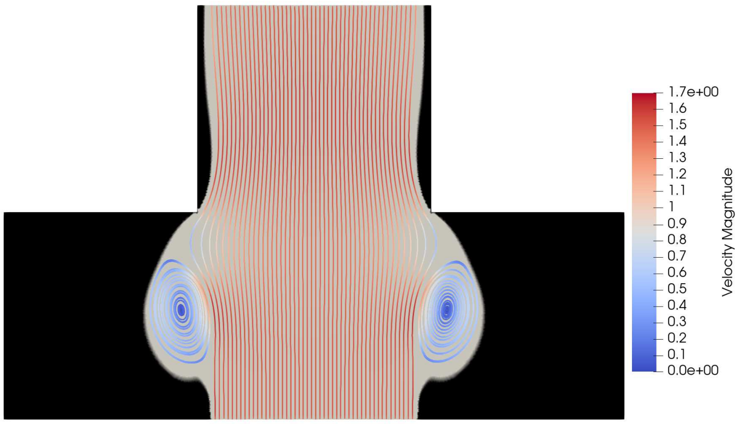

(e) Optimal domain shape, streamlines

Figure 4.21: Test-case 6: Design Parameter Evolution and Optimal Domain Streamlines. a),b),c),d) Design parameter evolution over various iterations; e) blood flow streamlines in the optimal domain shape.

Test-case 7:

The test-case 7 has been performed to investigate the effect of including the vorticity functional term, see (3.6), in the optimal shape. Studying the exact same geometry and BC of the test-case 6 it emerged that changing the value of β_R^* to $\beta_R^* = -1$ does not consistently change the design parameter evolution and the optimal domain shape (see Figure 4.22). Further comments and comparisons with the other test-cases will be held in the general discussion 4.3.

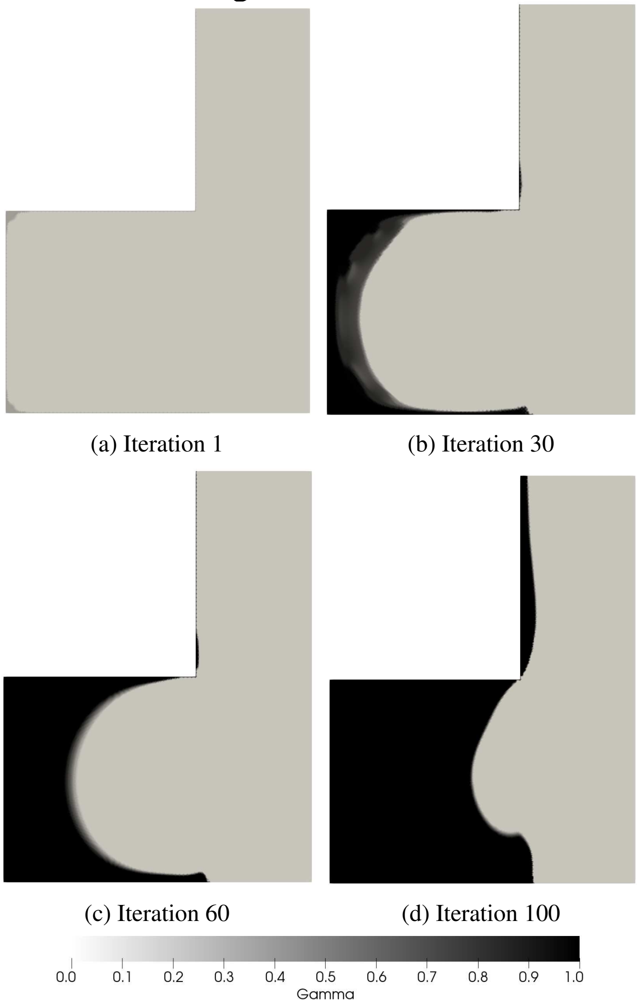

(a) Iteration 1 (b) Iteration 30

(c) Iteration 60 (d) Iteration 100

Figure 4.22: Test-case 7: Design parameter evolution.

Test-case 8:

To compensate the effects of imposing an inflow velocity with only normal component, it has been considered an higher optimization domain, setting the sinotubular junction to $h = 26mm$. The design parameter evolution follows the same pattern of the previous test-cases. In the first 50 iterations the optimization procedure performs a sort of regular shrinkage of the external cylinder, to reach as fast as possible a feasible value of the fluid domain volume. However, considering BC of type C, starting from it.60, the optimal shape bulge transforms to a tear-shaped bulge as in test-cases 5, 6, and 7 (see Figure 4.23). The streamlines behaviour in the optimal domain shape replicates exactly the results of the other test-cases with boundary conditions of type C. Looking at the 3D rotational extrusion in Figure 4.24d, the vortices are, in fact, trapped in the tear-shaped bulge.

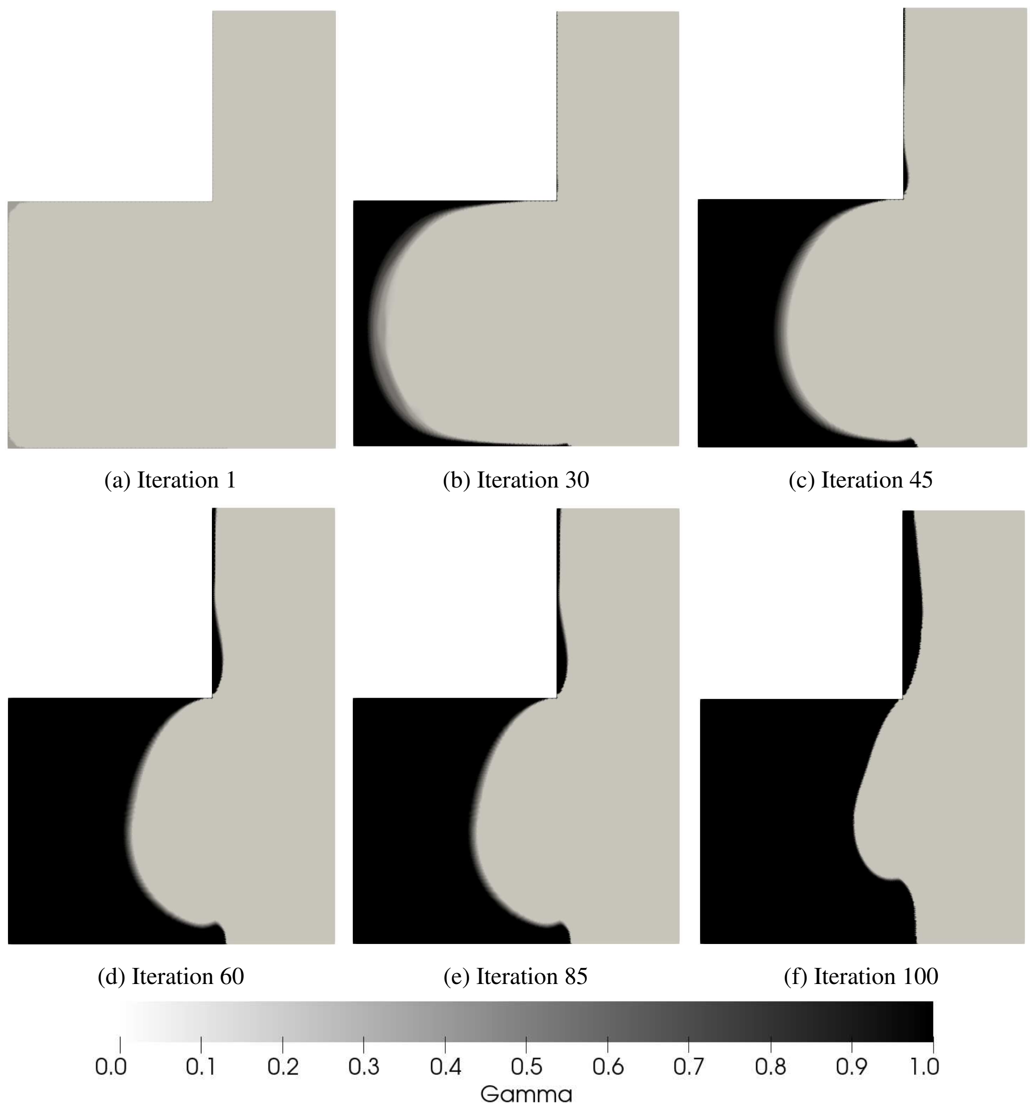

Figure 4.23: Test-case 8: Design Parameter Evolution

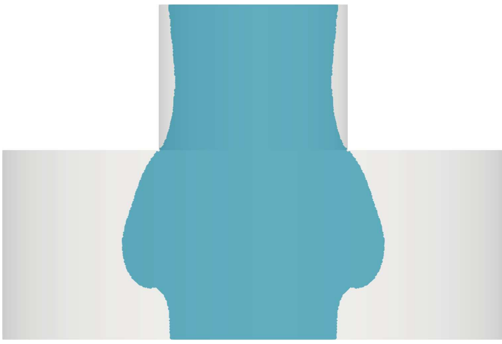

(a) Test-case 8: 2D Profile

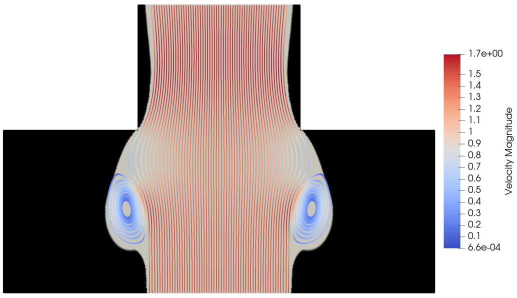

(b) Test-case 8: 2D Profile Streamlines

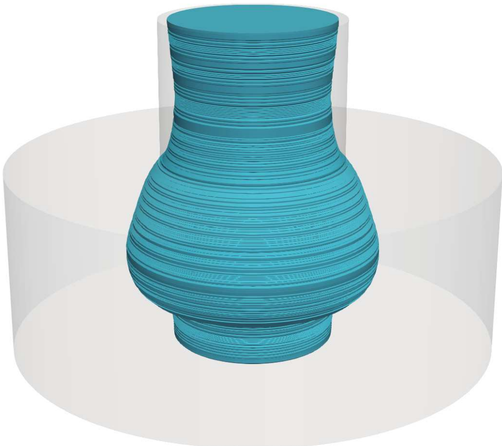

(c) Test-case 8: 3D Profile

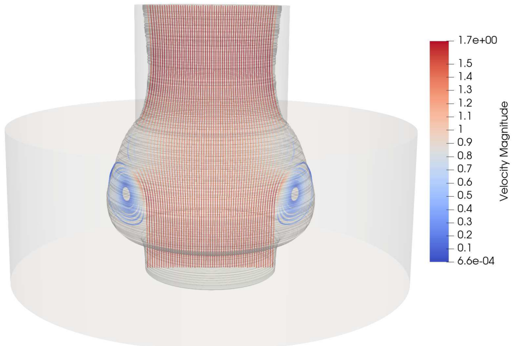

(d) Test-case 8: 3D Profile Streamlines

Figure 4.24: Test-case 8: Optimal Domain

Since this test-case has been performed after a robust topology optimization parameters tuning and various different geometry studies, here it is reported also the functional behaviour over the optimization iterations (see Figure 4.25). It can be observed that a feasible fluid domain volume is achieved at it.85.; in the subsequent iterations the algorithm lowers the functional value keeping the volume constraint satisfied. As a further remark for this test-case, it seems that the functional value distribution is concave until it reaches a suitable geometry, and then it becomes convex to have a faster convergence on its minimum value.

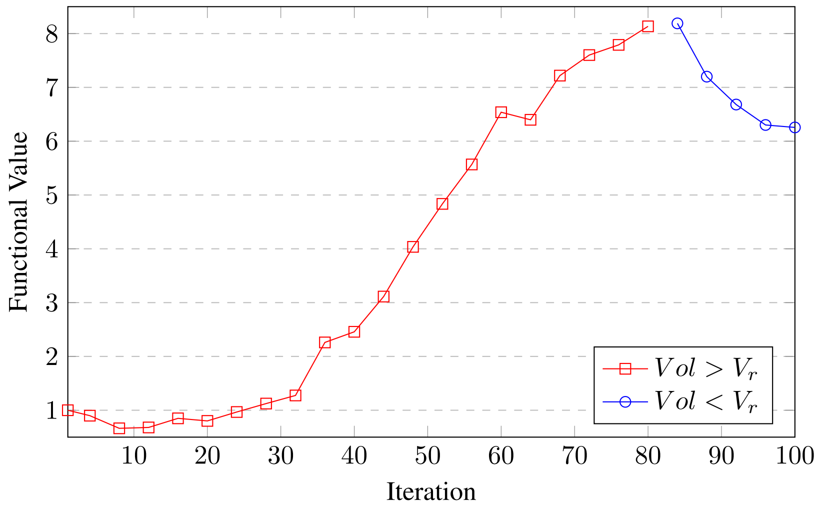

Figure 4.25: Test-case 8: Functional Value over 100 Iterations

Test-case 9:

The idea of this study case is to simulate all the instants in which the blood is injected into the aortic root through the aortic valve. To perform such study, BC of type D have been prescribed.

The design parameter evolution initially replicates the same behaviour of the test-cases with type C boundary conditions. But, starting from it.60, the evolution changes, leading to the narrowing of the fluid domain to almost restricting it to the inner cylinder at it.100 (see Figure 4.26).

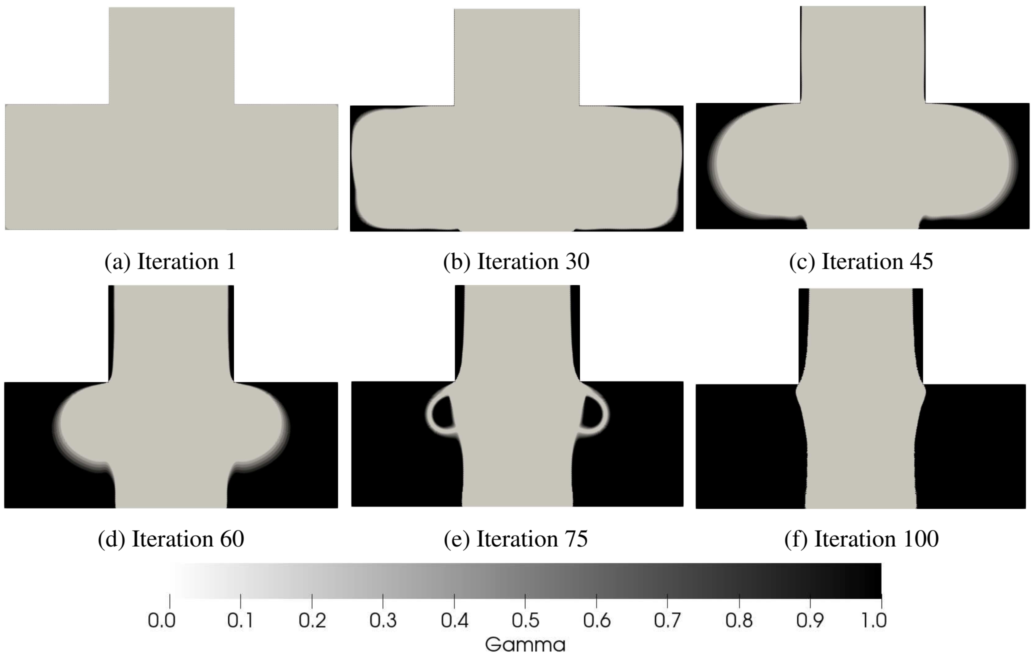

(a) Iteration 1 (b) Iteration 30 (c) Iteration 45

(d) Iteration 60 (e) Iteration 75 (f) Iteration 100

Figure 4.26: Test-case 9: Design Parameter Evolution

In conclusion, the optimal domain shape is different from the other boundary conditions cases (see Figure 4.27). The presence of a cusp at the sino-tubular junction, allows the formation of a little vortex; this vortex forces the streamlines of the injected flow to have a straight behaviour till they reach the outlet (see Figure 4.27d).

(a) Test-case 9: 2D Profile

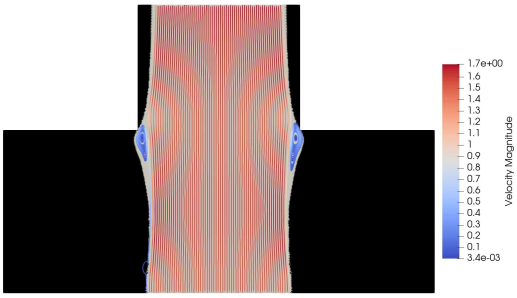

(b) Test-case 9: 2D Profile Streamlines

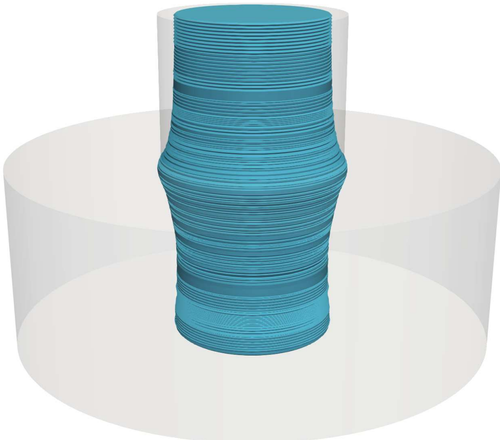

(c) Test-case 9: 3D Profile

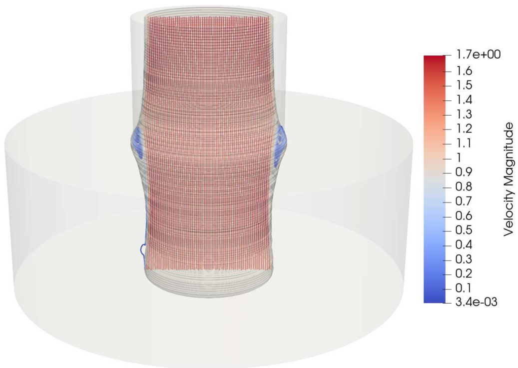

(d) Test-case 9: 3D Profile Streamlines

Figure 4.27: Test-case 9: Optimal Domain

4.3 Aortic Root Discussion

Whether the shape of the aortic sinuses plays a definite role (or not) in the local hemodynamics and aortic valve dynamics, is still unclear. Their peculiar shape suggests that the function cannot be merely limited to host the leaflets when the aortic valve is open. Valsalva in 1740 observed that the presence of sinuses in various animal species should indicate that these anatomical elements serve a common purpose [53]. In 1968 the Bellhouse brothers were the first to suggest that "apart from producing a thrust normal to the cusp and initiating valve closure, the vortices would also scour out the sinuses and prevent the formation of thrombi behind the cusps in blood flow" [1]. In 1970, Reid K. tried to fill the lack of the precise anatomical definition of the sinuses [2]. We observed that as far as the leaflets does not seem to be made of such an elastic material, "their closure must be achieved thanks to other life mechanisms", i.e., the aortic sinuses and their ridges. Reul, in 1990, proposed to describe the transverse view of the sinus shape as an epitrochoid [3]. Among the recent studies, Toninato et al. performed a comparison between various surgical valve implantation configurations, highlighting the importance of the aortic root shape in trans-aortic energy losses minimization [6].

The preliminary study cases and the test-cases 2 and 4, allowed us to understand the model limits, and, consequently, how to set the various parameters and possible initial geometries to treat the complex problem of studying the shape of the aortic root and its sinuses. Once the correct setup has been identified, some multi-scenarios simulations have been performed varying the boundary conditions in the aortic flow. The scope of these simulations was to investigate what part of the cardiac cycle could mainly determine the sinuses shape is optimizing in nature. The BC of Type C, i.e., the inlet velocity varying until to reach the velocity peak, seems to qualitatively well replicate the shape of the aortic sinuses tear-shaped bulges (see Figure 4.28).

The functional value evolution seems to follow a sort of prescribed pattern. Starting from the initial configuration, the algorithm increases its magnitude restricting the domain until it matches the volume constraint. Once a feasible volume has been identified, a geometry refinement is performed in order to to minimize the functional value (see Figures 4.6, 4.7, 4.8, 4.12, 4.18, and 4.25).

(a) Test-case 1

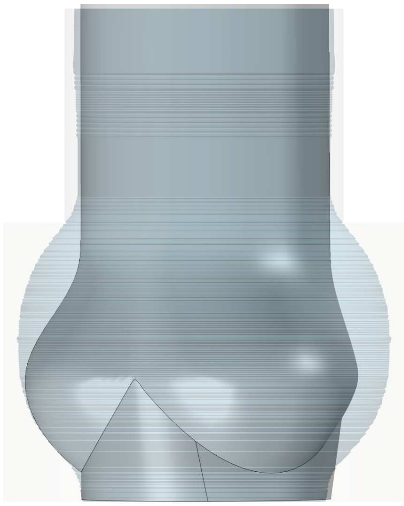

(b) Test-case 3

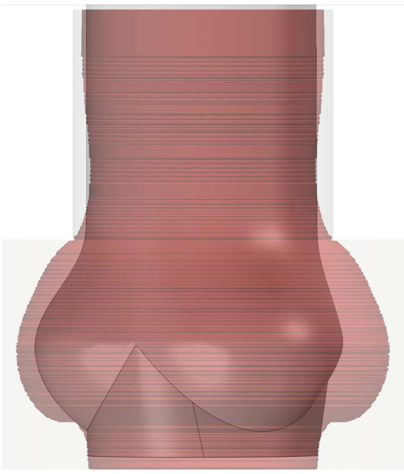

(c) Test-case 6

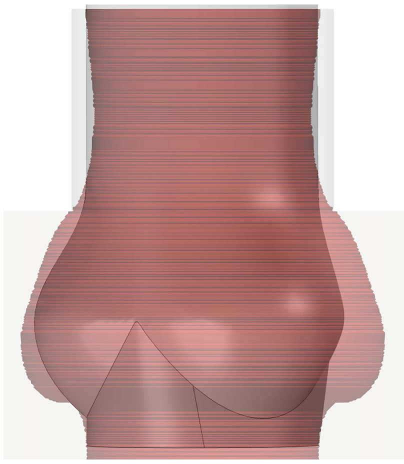

(d) Test-case 8

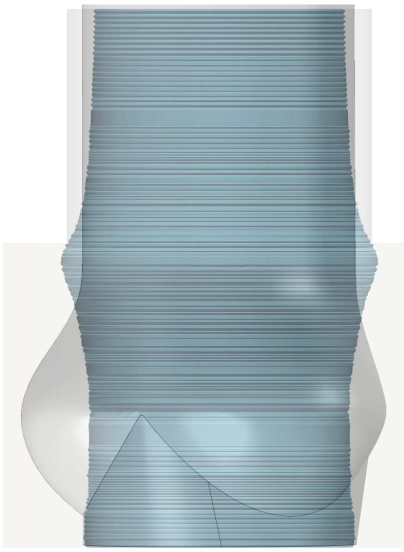

(e) Test-case 9

Figure 4.28: Test-cases comparison with the Aortic Root model 3.8. The figure represent the various axial-symmetric optimal domain shapes, overlapping them with the aortic root model profile in transparency.

Changing the topology optimization parameters to include the vorticity term in the functional, e.g. $\beta_R^* = -1$, does not influence neither the design parameter distribution in any of the iterations (see Figures 4.21, 4.22), nor the the final geometry of the "optimized aortic root" (see Figure 4.29).

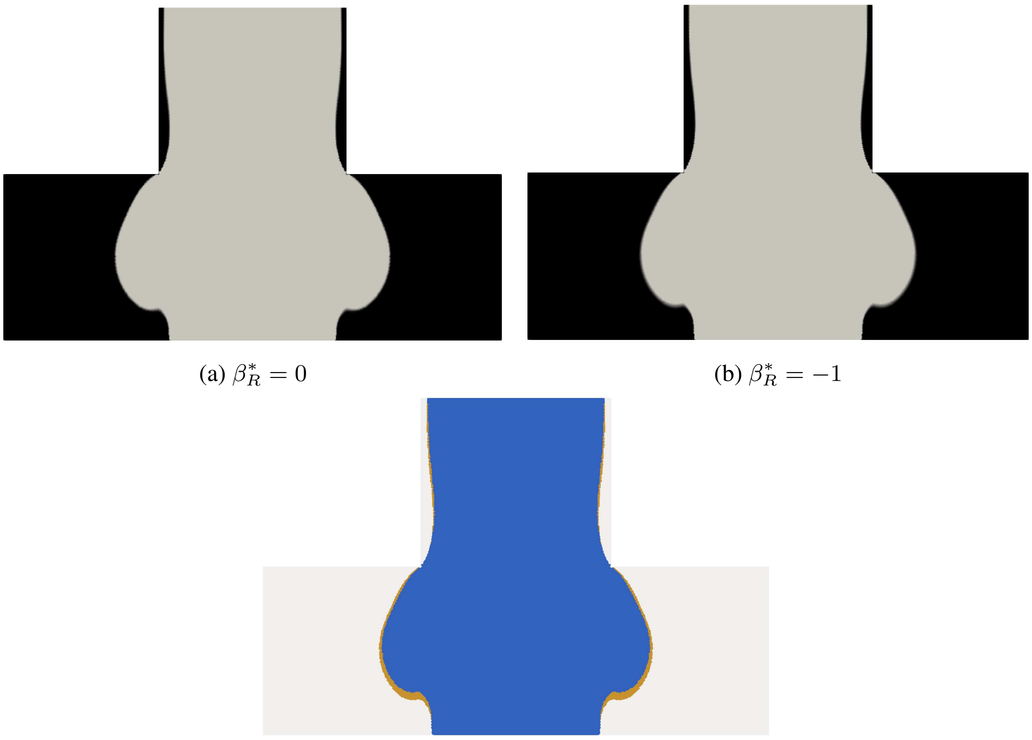

(a) $\beta_R^* = 0$ (b) $\beta_R^* = -1$

(c)

Figure 4.29: Test-case 6 and test-case 7 optimal designs comparison. a) $\beta_R^* = 0$, test-case 6, b) $\beta_R^* = -1$, test-case 7, c) Optimal designs superposition. $\beta_R^* = 0$: orange, $\beta_R^* = -1$: blue

This phenomena could be explained looking at the streamlines in the optimal domain (see Figure 4.21). The shape allows the formation of vortices inside the sinuses. Indeed, the system transfers energy from the central flow to the side vortices, rather than to dissipate energy by the wall shear stress. This reflects into a sort of implicit maximization of the vorticity. In the study-case of 3.7, maximizing the rotational

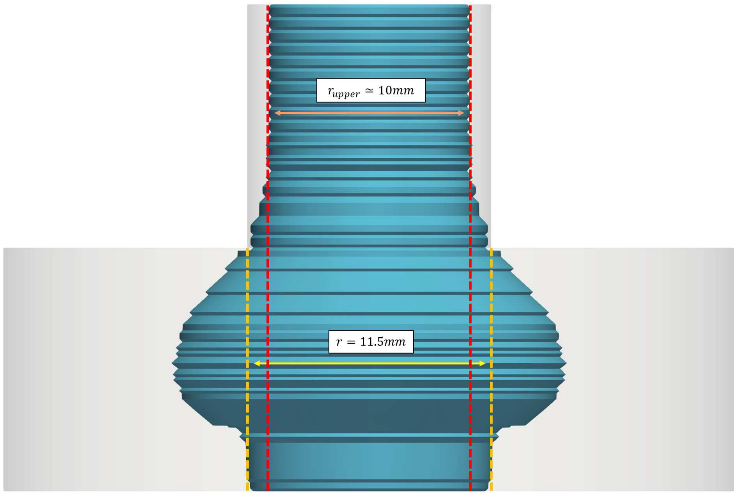

Figure 4.30: Test-case 5: Boundary layer removal from the Optimal Shape.

effects drastically changed the final configuration of the fluid domain (see Figure 4.11); differently, working with high Reynolds numbers leads to optimal shapes containing the vortices, and thus vanishing influence of the vorticity term in the functional of Equation (3.6).

For the two-dimensional test-cases, the α_{max} value had to be chosen high enough to guarantee the convergence to almost discrete values of the design parameter; in according to the results about convergence instability obtained testing the problem 3.3.1.

Furthermore, the optimal shape for high Reynolds numbers tend to behave like a *vena contracta*, excluding the regions near the side boundaries in the upper cylinder (see Figure 4.30). Hence, to compensate such effect, the aortic root radius above the sinotubular junction has been enlarged, w.r.t. the inlet one, by $1.5mm$ in test-cases 1, 3, 7 and 8. With this implementation, the solution provides an optimal upper cylinder diameter matching the aortic root's one.

Model Limitations

Owing to its simplify nature, the model ignores the presence of the valvular leaflets. However, since their material density is comparable with the blood one (see Swanson et al. [54] and Kasyanov et al. [55]), their presence do not really modify the fluid flow till they reach their maximum tension position , i.e., when the valve is completely open.

The presence of the coronary arteries is another important anatomical element that characterize the sinuses structure. This could be simulated by imposing the presence of two little outlets, forcing the optimal shape boundary to pass through these holes. Nevertheless, it is to stress that the coronaries presence is relevant during the back-flow phase, i.e., when the valve is closed. Consequently, their presence goes beyond the scope of this work, but it could represent a further improvement of the optimization analysis. Theoretically, the topology optimization algorithm should converge to a discrete optimization parameter solution. However, the practice requires a very large number of iterations. Therefore, to filter the optimal solution it has been chosen to consider only the mesh elements that have all nodal values of γ smaller than 0.15.

It must be noted that, until now, the topology optimization studies on fluid domains have focused on problems in strong laminar regime, i.e., for $\mathbf{Re} \simeq 1 - 10$; therefore no particular *a priori* optimal geometry could be expected. Indeed, the aim of this study is to work in a physiological setting. Testing with such physical parameters pushes the classical topology optimization tools to their limits right before the laminar/turbulent transition.

The three dimensional studies 2 and 4 exemplify a recurrent behaviour of the solutions for the 3D topology optimization model. Despite the insertion of the wall boundaries within the domain, the optimal solution is slightly affected by their presence (see Figure 4.31). These results pointed out potential limits of the used 3D model, highlighting its inability to recreate the correct sinuses shape at the leaflets commissures. Therefore, it has been decided to study the problem assuming a full axial-symmetric approach. Accordingly, the optimal shape comparison with the Valsalva sinuses has then been transformed into the problem on finding the aortic root optimal profile studying its 2D model.

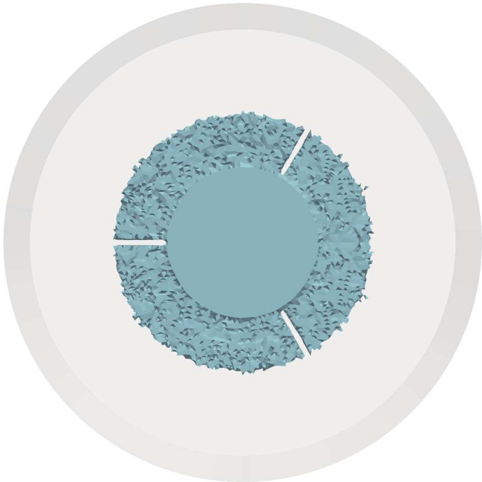

(a) Test-case 2, bottom view of the optimal domain

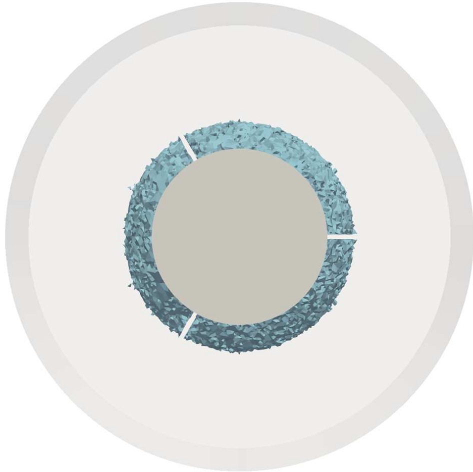

(b) Test-case 2, top view of the optimal domain

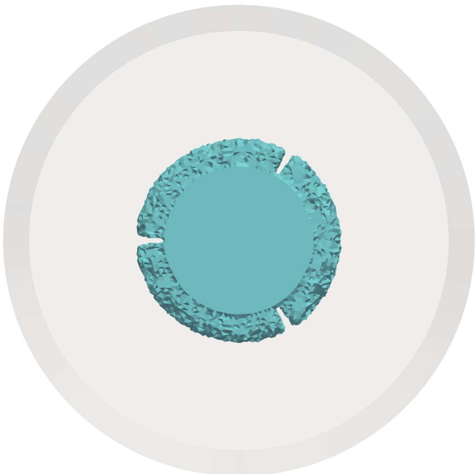

(c) Test-case 4, bottom view of the optimal domain

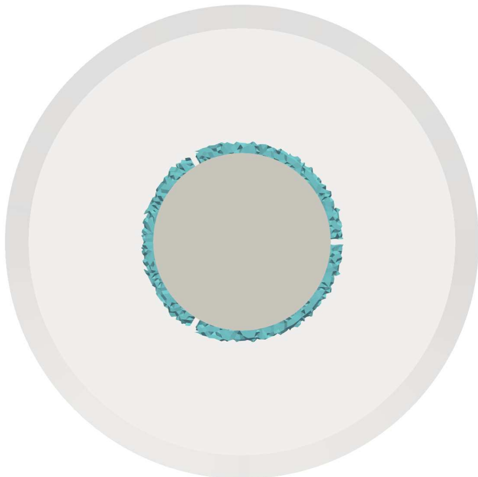

(d) Test-case 4, top view of the optimal domain

Figure 4.31: 3D Study Cases: Wall Boundaries in the Optimal Shape

4.4 Conclusions

The topology optimization study seems to confirm that the Valsalva sinuses plays a crucial role in the energy loss minimization during the blood flow acceleration phase.
Anyway, changing the topology optimization parameters to include the vorticity term in the functional, e.g. $\beta_R^* = -1$, does not consistently modify the final geometry of the "optimized aortic root".
In Nature, the vortices inside the aortic sinuses facilitate some portions of blood to circulate between the fully opened leaflets and the sinuses walls, promoting the initial valve closure mechanism. In any case, this explanation does not fully catch the role of the sinuses anatomy. The Valsalva sinuses shape follows the shape of the the completely opened leaflets, keeping a gap to avoid any contact between the elements. Therefore, it is reasonable that the open-leaflets shape minimizes the energy losses during the peak flow; this observation unfolds into a first insight to explain the presence of the large coaptation portion of the leaflets. Furthermore, one of the most common degenerations of the aortic root with age is the enlargement of the sino-tubular junction. The ethiology of this disease is likely the continuous stress of the ejected blood on the walls. It should be noted that, if there were not the sinusoidal shape, these stress condition would become even higher. In a cylindrical shape, in fact, we assist to the detachment of

the boundary layer, and the formation of vortices locally narrowing the streamtube along the ascending aorta.

To find a suitable way to break the axial-symmetry of the 3D model solution would be an important improvement of the present model. Probably, stricter assumptions on the initial optimization domain should work in this direction. However, this purpose is out of the scope of the present thesis. The thesis aimed at investigating the optimal shape of the aortic root, which minimizes the energy losses of the systolic flow. A different purpose would be to perform a "Valsalva sinuses inverse design" starting from *a posteriori* determined initial configuration. Further ideas to replicate the epitrochoidal sinuses shape are the following: we can insert the walls coherently with the real-case configuration near the annulus and force a the intra-leaflet triangular junction between the three sinuses, following the leaflets shape. Finally, an interesting analysis could include also a rotating injected flow, which is the only physiological condition on the flow missing in the studied model.

Appendix A

The Convective Term

For high Reynolds number (large convection term), it is necessary to introduce numerical diffusion in the system to stabilize the algorithm. Briefly, the problem is that the shape functions "weight" in the same way all the grid nodes in the computational solution. Moreover, if the convection is relevant, the upstream nodes will clearly have a higher impact on the downstream ones than the opposite. The standard solution to this problem is the SUPG ("Streamline Upwind Petrov Galerkin), which is a residual based stabilization and adds diffusion in the same direction of the convection term.
We stabilized the method by suitably choosing the coefficient β. Two possible approaches are the Oseen approach and the Picard iteration.

1. **Oseen approach.** In this case, at each time step, we use the velocity field of the last computed time, $\beta = u_h^n$. The resulting algorithm is relatively simple, but some restrictions on the time step Δt have to be applied to ensure the stability of the method.

2. **Picard iteration.** This approach is based on a standard nonlinear solver (root finding), and it practically works through an inner loop for the β stabilization. At each time step we fix a first tentative term equal to $\beta = u_h^{n+1,0} = u_h^n$ and then we keep solving the system, without increasing the time, and update the value of β until convergence. The convergence occurs by a test on the difference between the β values of next two following iterations.

A complete analysis is performed in [25] or [26].

Appendix B

Introduction to PDE Constrained Optimization

Let us now introduce some the most relevant concepts in order to formulate our topology optimization problem as a control problem with PDE constraints.
The discussion follows the arguments as they are presented in [15].

Formulation of control-constrained problems

Let consider a general non-linear problem of the form:

$$\min_{(y,u)\in Y\times U} J(y,u) \quad \text{subject to} \quad e(y,u)=0, \quad u\in U_{ad}\subseteq U. \quad \text{(B.1)}$$

Assumption B.1. Let's make the following assumptions:

1. $U_{ad} \subset U$ is nonempty, convex and closed.
2. $J : Y \times U \to \mathbb{R}$ and $e : Y \times U \to Z$ are continuously differentiable, with U, Y, Z Banach Spaces.
3. For all $u \in V, V \subset U$, neighborhood of U_{ad}, the state equation $e(y, u) = 0$ has the unique solution $y = y(u) \in Y$.
4. $e_y(y(u), u) \in \mathcal{L}(Y, Z)$ has bounded inverse $\forall u \in V \supset U_{ad}$.

Definition. ***Fréchet Differentiability***

Let V, W be normed vector spaces and $U \subseteq V$, open set. A function $f : U \to W$ is said Fréchet differentiable at $x \in U$, if there exists a bounded linear operator $D : V \to W$ such that:

$$\lim_{||h||_V \to 0} \frac{||f(x+h) - f(x) - Dh||_W}{||h||_V} = 0.$$

Definition. ***Gateaux Derivative***

Let V, W be normed vector spaces and $U \subseteq V$, open set.

The Gateaux derivative of a function $f : U \to W$ at $x \in U$ is defined as:

$$g(x) = \lim_{t \to 0} \frac{f(x+th) - f(x)}{t}$$

Observation. *If a function is Fréchet differentiable at a point then it is also Gateaux differentiable and we have: $g(x) = D = D_f(x)$, the differential of f.*

Under the previous assumptions the mapping $u \in V \mapsto Y$ is continuously Fréchet differentiable by the implicit function theorem (Dini's theorem).

General first order optimality condition

Let consider the general problem (B.1) and let Assumption B.1 hold. The reduced problem can now be formulated as follows,

$$\min_{u \in U} \hat{J}(u) \quad \text{subject to} \quad u \in U_{ad} \subseteq U, \tag{B.2}$$

with the reduced functional

$$\hat{J}(u) := J(y(u), u), \tag{B.3}$$

where $V \ni u \mapsto y(u) \in Y$ is the solution operator of the state equation.

Now some classical results are stated in order to justify the use of the adjoint formulation method.

Theorem B.2. *Let assumption B.1 hold. If $\bar{u}$ is a local solution of the reduced problem* (B.2) *then $\bar{u}$ satisfies the following variational inequality:*

$$\bar{u} \in U_{ad} \quad \textit{and} \quad \left\langle \hat{J}(\bar{u}), u - \bar{u} \right\rangle_{U^*,U} \geq 0 \quad \forall u \in U_{ad}. \tag{B.4}$$

The previous variational inequality directly yields the following necessary first order condition.

$$\frac{d}{du}\hat{J}(\bar{u}) = \frac{\partial J}{\partial y}\frac{dy}{du}\Big|_{(y(\bar{u}),\bar{u})} + \frac{\partial J}{\partial u}\Big|_{(y(\bar{u}),\bar{u})} = 0. \tag{B.5}$$

Observation B.3. *The direct computation of condition* (B.5) *can result a complex task because, specially in the PDE constrained case (e.g. Navier Stokes equations), the dependence of y with u is not directly computable. Moreover, since our scope is to get a domain topology optimization using numerical methods to solve both constraints and variational conditions, the analytical form of y is not known and so this solution strategy could not be applied.*

Finally we will use the adjoint representation of the functional derivative,

$$\hat{J}'(u) = e_u(y(u), u)^* \lambda(u) + J_u(y(u), u) \tag{B.6}$$

where $\lambda(u) \in Z^*$ is the adjoint state, solving the adjoint equation

$$e_y(y(u), (u))^* \lambda(u) = -J_y(y(u), u). \tag{B.7}$$

This leads to the formulation of an adjoint differential system that needs to be solved in order to proceed with the numerical solution of the variational problem.

Let us now state an optimality condition for the adjoint formulation.

Theorem B.4. *Let* $(\bar{y}, \bar{u})$ *an optimal solution of the problem* (B.1) *and let assumption B.1 hold. Then, there exists an adjoint state* $\bar{\lambda} \in Z^*$, *such that the following optimality conditions hold:*

$$e(\bar{y}, \bar{u}) = 0; \tag{B.8}$$

$$e_y(\bar{y}, \bar{u})^* \bar{\lambda} = -J_y(\bar{y}, \bar{u}); \tag{B.9}$$

$$\bar{u} \in U_{ad}, \quad \left\langle J_u(\bar{y}, \bar{u}) + e_u(\bar{y}, \bar{u})^* \bar{\lambda}, u - \bar{u} \right\rangle_{U^*,U} \geq 0. \tag{B.10}$$

Let us now consider a more general formulation of the problem in (B.1):

$$\min_{w \in W} J(w) \quad \text{subject to} \quad G(w) \in \mathcal{K}_G, \quad w \in \mathcal{C}. \tag{B.11}$$

Thanks to the Robinson's regularity condition [28] we can now state an important theorem, introduced in [27], that generalizes the Karush-Kuhn-Tucker conditions for PDE constrained optimal control problems.

Theorem B.5. *(Zowe and Kurcyusz) Let* $J : W \to \mathbb{R}, G : W \to V$ *be continuously Fréchet differentiable functions with Banach-spaces W,V. Further let* $\mathcal{C} \subset W$ *be non-empty, closed and convex, and let* $\mathcal{K}_G \subset V$ *be a closed convex cone. Then for any local solution* $\bar{w}$ *of* (B.11) *at which Robinson's regularity condition is satisfied, the following optimality condition holds:*

There exist a Lagrange multiplier $\bar{q} \in V^*$ *with*

$$G(\bar{w}) \in \mathcal{K}_G, \tag{B.12}$$

$$\bar{q} \in \mathcal{K}_G^\circ := \big\{ q \in V^* \big| \langle q, v \rangle_{V^*,V} \le 0 \,\forall v \in \mathcal{K}_G \big\}, \tag{B.13}$$

$$\langle \bar{q}, G(\bar{w}) \rangle_{V^*,V} = 0, \tag{B.14}$$

$$\bar{w} \in \mathcal{C}, \quad \langle J'(\bar{w}) + G'(\bar{w})^* \bar{q}, w - \bar{w} \rangle_{W^*,W} \ge 0 \;\; \forall w \in \mathcal{C}. \tag{B.15}$$

Observation B.6. *Using the Lagrangian function*

$$L(w, q) := J(w) + \langle q, G(w) \rangle_{V^*,V} \tag{B.16}$$

we can write (B.15) *in the following more compact form*

$$\bar{w} \in \mathcal{C}, \quad \langle L_w(\bar{w}, \bar{q}), w - \bar{w} \rangle_{W^*,W} \ge 0 \;\; \forall w \in \mathcal{C}. \tag{B.17}$$

Application to PDE-constrained optimization

Consider now an optimal control problem like that reported in (B.1), for which the state equation, $e(y, u) = 0$, is a PDE (e.g., 2D Navier-Stokes), which requires also $c(y) \in \mathcal{K}$ similarly to (B.11). Then:

$$\min_{(y,u) \in Y \times U} J(y, u) \quad \text{subject to} \quad e(y, u) = 0,\ c(y) \in \mathcal{K},\ u \in U_{ad} \subseteq U. \tag{B.18}$$

where $e : Y \times U \to Z$ and $c : Y \to R$ are continuously Fréchet differentiable, $\mathcal{K} \subset R$ is a closed convex cone and $U_{ad} \subset U$ is a closed convex set.

To keep a coherent notation we define

$$G : Y \times U \ni \begin{pmatrix} y \\ u \end{pmatrix} \mapsto \begin{pmatrix} e(y,u) \\ c(y) \end{pmatrix} \in Z \times R$$

$$\mathcal{K}_G = \{0\} \times \mathcal{K}, \qquad \mathcal{C} = Y \times U_{ad}$$

Let us now formulate the Lagrangian function, with the multiplier in the form $(\lambda, \nu) \in Z^* \times R^*$,

$$\begin{aligned} \mathcal{L}(y,u,\lambda,\nu) &= J(y,u) + \langle \lambda, e(y,u) \rangle_{Z^*,Z} + \langle \nu, c(y) \rangle_{R^*,R} = \\ &= L(y,u,\lambda) + \langle \nu, c(y) \rangle_{R^*,R} \end{aligned}$$

with the Lagrangian restricted at the equality constraints

$$L(y,u,\lambda) = J(y,u) + \langle \lambda, e(y,u) \rangle_{Z^*,Z}.$$

Since $\mathcal{K}_G = \{0\} \times \mathcal{K}$, we obtain $\mathcal{K}_G^\circ = Z^* \times \mathcal{K}^\circ$. Therefore, assuming the Robinson's regularity condition holds [15], the optimality necessary conditions of theorem B.5 are:

$$\begin{aligned} & e(\bar{y},\bar{u}) = 0, \qquad c(\bar{y}) \in \mathcal{K}, \\ & \bar{\nu} \in \mathcal{K}^\circ, \quad \langle \bar{\nu}, c(\bar{y}) \rangle_{R^*,R} = 0, \\ & \langle L_y(\bar{y},\bar{u},\bar{\lambda}) + c'(\bar{y})^* \bar{\nu}, y - \bar{y} \rangle_{Y^*,Y} \geq 0 \quad \forall y \in Y, \\ & \bar{u} \in U_{ad}, \quad \langle L_u(\bar{y},\bar{u},\bar{\lambda}), u - \bar{u} \rangle_{U^*,U} \geq 0 \quad \forall u \in U_{ad}. \end{aligned}$$

Finally, we have that the corresponding of the Karush-Kuhn-Tacker conditions for PDE constrained control problems are:

$$e(\bar{y},\bar{u}) = 0, \qquad c(\bar{y}) \in \mathcal{K}, \tag{B.19}$$

$$\bar{\nu} \in \mathcal{K}^{\circ}, \quad \langle \bar{\nu}, c(\bar{y}) \rangle_{R^*,R} = 0, \tag{B.20}$$

$$L_y(\bar{y},\bar{u},\bar{\lambda}) + c'(\bar{y})^*\bar{\nu} = 0, \tag{B.21}$$

$$\bar{u} \in U_{ad}, \quad \langle L_u(\bar{y},\bar{u},\bar{\lambda}), u - \bar{u} \rangle_{U^*,U} \geq 0 \quad \forall u \in U_{ad}. \tag{B.22}$$

Appendix C

The Functional Weights

Since, given two matrices A, B,

$$||A \pm B||^2 = ||A||^2 + ||B||^2 \pm 2A : B$$

3.10 reads

$$\begin{aligned}
\beta_S &= \frac{1}{2} \cdot \frac{||\nabla \mathbf{u}||^2 + ||\nabla \mathbf{u}^T||^2 - 2(\nabla \mathbf{u} : \nabla \mathbf{u}^T)}{||\nabla \mathbf{u}||^2 + ||\nabla \mathbf{u}^T||^2 + 2(\nabla \mathbf{u} : \nabla \mathbf{u}^T)} \cdot \beta_R = \\
&= \frac{1}{2} \cdot \Big(1 - \frac{4(\nabla \mathbf{u} : \nabla \mathbf{u}^T)}{||\nabla \mathbf{u}||^2 + ||\nabla \mathbf{u}^T||^2 + 2(\nabla \mathbf{u} : \nabla \mathbf{u}^T)}\Big) \cdot \beta_R = \\
&= \frac{1}{2} \cdot \Big(1 - \frac{2(\nabla \mathbf{u} : \nabla \mathbf{u}^T)}{||\nabla \mathbf{u}||^2 + \nabla \mathbf{u} : \nabla \mathbf{u}^T}\Big) \cdot \beta_R
\end{aligned}$$

Hence, an *a priori* estimate on the real contribution of the deformation and vorticity terms to the functional is not possible. In fact, they depend on the velocity tensor symmetric and antisymmetric parts for the considered problem.

The functional coefficients as introduces in 3.6 can be expressed in function of the β_R^* and β_p^* ratios:

$$\begin{aligned}
\beta_\alpha &= \frac{1}{2+\beta_R^*+\beta_p^*};\\
\beta_S &= \frac{1}{2+\beta_R^*+\beta_p^*};\\
\beta_R &= \frac{\beta_R^*}{2+\beta_R^*+\beta_p^*};\\
\beta_p &= \frac{\beta_p^*}{2+\beta_R^*+\beta_p^*}.
\end{aligned} \tag{C.1}$$

it can be observed that once the ratios β_R^*, β_p^* values are prescribed, the functional weights formulation is determined.

Bibliography

[1] Bellhouse B. and F. “Mechanism of closure of the aortic Valve”. In: *Nature* 217 (1968), pp. 86–87. DOI: `https://doi.org/10.1038/217086b0`.

[2] Reid K. “The anatomy of the sinus of Valsalva”. In: *Thorax* 25.1 (1970), pp. 79–85.

[3] Reul H. et al. “The geometry of the aortic root in health, at valve disease and after valve replacement”. In: *Journal of Biomechanics* 23.2 (1990), pp. 181–191. DOI: `https://doi.org/10.1016/0021-9290(90)90351-3`.

[4] Bäck T.M. et al. “Biomechanical factors in the biology of aortic wall and aortic valve diseases”. In: *Cardiovascular Research* 99.2 (2013), pp. 232–241. DOI: `https://doi.org/10.1093/cvr/cvt040`.

[5] Loukas M. et al. “The anatomy of the aortc Root”. In: *Clinical Anatomy* 35.20 (2014), p. 1344. DOI: `https://doi.org/10.1002/ca.22295`.

[6] Toninato R. et al. “Physiological vortices in the sinuses of Valsalva: An in vitro approach for bio-prosthetic valves”. In: *Journal of Biomechanics* 49.13 (2016), pp. 2635–2643. DOI: `https://doi.org/10.1016/j.jbiomech.2016.05.027`.

[7] Bertelsen L. et al. “Flow measurement at the aortic root-impact of location of through-plane phase contrast velocity mapping”. In: *Journal of Cardiovascular Magnetic Resonance* 18 (2016), pp. 1–8.

[8] Bissel M.M et al. “Flow vortices in the aortic root, in vivo 4DMRI confirms prdictions of Leonardo Da Vinci”. In: *European Hearth Journal* 27.5 (2014), pp. 748–756. DOI: `https://doi.org/10.1093/eurheartj/ehu011`.

[9] Kasel A.M. et al. “Standardized Imaging for Aortic Annular Sizing: Implications for Transcatheter Valve Selection”. In: *JACC: Cardiovascular Imaging* 6.2 (2013), pp. 249–262. DOI: `https://doi.org/10.1016/j.jcmg.2012.12.005`.

[10] Morinishi K. Fukui T. “Influence of Vortices in the Sinus of Valsalva on Local Wall Shear Stress Distribution”. In: *International Journal of Life Science and Medical Research* 3.3 (2013), pp. 94–102. DOI: `10.5963/LSMR0303002`.

[11] *Aortic Aneurysm*. URL: `https://www.bswhealth.com/conditions/aortic-aneurysm`.

[12] Bendsøe M.P. Sigmund O. *Topology Optimization. Theory, Methods and Applications*. 1st ed. Springer, 2003.

[13] Bendsøe M.P. “Optimal shape design as a material distribution problem”. In: *Structural Optimization* 1 (1989), pp. 193–202.

[14] Maute K. Sigmund O. “Topology optimization approaches”. In: *Structural and Multidisciplinary Optimization* 48 (2013), pp. 1031–1055. DOI: `https://doi.org/10.1007/s00158-013-0978-6`.

[15] Hinze M. et al. *Optimization with PDE Constraints*. Springer, 2009.

[16] Liu Z. Deng Y. Wu Y. *Topology Optimization Theory for Laminar Flow*. 1st ed. Springer, 2017.

[17] Dbouk T. “A review about the engineering design of optimal heat transfer systems using topology optimization”. In: *Applied Thermal Engineering* 112 (2017), pp. 841–854. DOI: `https://doi.org/10.1016/j.applthermaleng.2016.10.134`.

[18] Alexander J. et al. “A Review of Topology Optimisation for Fluid-Based Problems”. In: *Fluids* 5.1 (2020), p. 29. DOI: `https://doi.org/10.3390/fluids5010029`.

[19] Kikuchi N. Bendsøe M.P. “Generating optimal topologies in structural design using a homogenization method”. In: *Computer Methods in Applied Mechanics and Engineering* 71.2 (1988), pp. 197–224. DOI: `https://doi.org/10.1016/0045-7825(88)90086-2`.

[20] Grandhi R.V. Deaton J.D. “A survey of structural and multidisciplinary continuum topology optimization: post 2000”. In: *Structural and Multidisciplinary Optimization* 49 (2014), pp. 1–38. DOI: `https://doi.org/10.1007/s00158-013-0956-z`.

[21] SDC Verifier. *2022 v. R1*. SDCVerifier, Haarlem Zijlvest 25, 2011 VB, The Netherlands, 2022.

[22] Svanberg K. “The method of moving asymptotes—a new method for structural optimization”. In: *International Journal for Numerical Methods in Engineering* 24 (2017), pp. 359–373. DOI: `https://doi.org/10.1002/nme.1620240207`.

[23] N. H. et al. Kim. “Generalized Optimality Criteria Method for Topology Optimization”. In: *Applied Sciences* 11.7 (2021). DOI: `10.3390/app11073175`.

[24] Zymaris A.S. et al. “Continuous adjoint approach to the Spalart–Allmaras turbulence model for incompressible flows”. In: *Computers and Fluids* 38 (2009), pp. 1528–1538. DOI: `https://doi.org/10.1016/j.compfluid.2008.12.006`.

[25] Putti M. *Notes on Numerical Methods for Differential Equations*. Lecture Nortes of "Numerical Methods for Continuous Systems, 2021.

[26] Quarteroni A. *Numerical Models for Differential Problems*. Springer, 2014.

[27] Kurcyusz S. Zowe J. “Regularity and stability for the mathematical programming problem in Banach spaces”. In: *Applied Mathematics and Optimization* 5 (1979), pp. 49–62. DOI: `https://doi.org/10.1007/BF01442543`.

[28] Robinson S.M. “Stability Theory for Systems of Inequalities, Part II: Differentiable Nonlinear Systems”. In: *SIAM Journal on Numerical Analysis* 13.4 (1976), pp. 497–513. DOI: `10.1137/0713043`.

[29] Zeidler E. *Nonlinear Functional Analysis and its Applications. I, Fixed-Point Theorems*. Springer, 1986.

[30] Fischer M. et al. “Fréchet Differentiability of Unsteady Incompressible Navier–Stokes Flow with Respect to Domain Variations of Low Regularity by Using a General Analytical Framework”. In: *SIAM Journal on Control and Optimization* 55.5 (2017), pp. 3226–3257. DOI: `10.1137/16M1089563`.

[31] Arthur Stück. *Adjoint Navier–Stokes Methods for Hydrodynamic Shape Optimisation*. TUHH, 2011.

[32] Dowling D.R. Kundu P.K. Cohen I.M. *Fluid Mechanics*. 6th ed. 2016.

[33] Petersson J. Borrvall T. “Topology optimization of fluids in Stokes flow.” In: *International Journal for Numerical Methods in Fluids* 41 (2003), pp. 77–107. DOI: `https://doi.org/10.1002/fld.426`.

[34] Olesen L.H. et al. "A high-level programming-language implementation of topology optimization applied to steady-state Navier–Stokes flow". In: *International Journal for Numerical Methods in Engineering* 65.7 (2006), pp. 975–1001. DOI: `https://doi.org/10.1002/nme.1468`.

[35] Deng Y. et al. "Topology optimization of steady Navier–Stokes flow with body force". In: *Computer Methods in Applied Mechanics and Engineering* 255 (2013), pp. 306–321. DOI: `https://doi.org/10.1016/j.cma.2012.11.015`.

[36] COMSOL Multiphysics®. *v. 6.1*. COMSOL AB, Stockholm, Sweden, 2016.

[37] Fortin M. Boffi D. Brezzi F. *Mixed Finite Element Methods and Applications*. Springer, 2013.

[38] Sani R.L. Gresho P.M. "On pressure boundary conditions for the incompressible Navier-Stokes equations". In: *International Journal for Numerical Methods in Fluids* 7.10 (1987), pp. 1111–1145. DOI: `https://doi.org/10.1002/fld.1650071008`.

[39] Koch H. and Tataru D. "Well-posedness for the Navier–Stokes Equations". In: *Advances in Mathematics* 157.1 (2001), pp. 22–35. DOI: `https://doi.org/10.1006/aima.2000.1937`.

[40] TUREK S. Heywood J.G. Rannacer R. "Artificial Boundaries and flux and pressure conditions for the incompressible Navier-Stokes equatons". In: *International Journal for Numerical Methods in Fluids* 22.5 (1996), pp. 325–352. DOI: `https://doi.org/10.1002/`.

[41] Spalding D.B. Patankar S.V. "A calculation procedure for heat, mass and momentum transfer in three-dimensional parabolic flows". In: *International Journal of Heat and Mass Transfer* 15.10 (1972), pp. 1787–1806. DOI: `https://doi.org/10.1016/0017-9310(72)90054-3`.

[42] Elman H. et al. "A taxonomy and comparison of parallel block multi-level preconditioners for the incompressible Navier–Stokes equations". In: *Journal of Computational Physics* 227.3 (2008), pp. 1790–1808. DOI: `https://doi.org/10.1016/j.jcp.2007.09.026`.

[43] *OpenFoam®*. URL: `https://www.openfoam.com`.

[44] Wathen A.J. Elman H.C. DIlvester D.J. *Finite Elements and Fast Iterative Solvers with Applications in Incompressible Fluid Dynamics*. Oxford University Press, 2005.

[45] Hughes T.J.R. Brooks A.N. "Streamline upwind/Petrov-Galerkin formulations for convection dominated flows with particular emphasis on the incompressible Navier-Stokes equations". In: *Computer Methods in Applied Mechanics and Engineering* 32.1 (1982), pp. 199–259. DOI: `https://doi.org/10.1016/0045-7825(82)90071-8`.

[46] Misra A. Shukla A. and Kumar S. “Checkerboard problem in finite element based topology optimization”. In: *International Journal of Advances in Engineering & Technology* 6.4 (2013), p. 1769.

[47] Berggren M. “Numerical Solution of a Flow-Control Problem: Vorticity Reduction by Dynamic Boundary Action”. In: *SIAM Journal on Scientific Computing* 19.3 (1998), pp. 829–860. DOI: 10.1137/S1064827595294678.

[48] Rozza G. Quarteroni A. “Optimal Control and Shape Optimization of Aorto-Coronaric Bypass Anastomoses”. In: *Mathematical Models and Methods in Applied Sciences* 13.12 (2003), pp. 1801–1823. DOI: 10.1142/S0218202503003124.

[49] Abraham F. et al. “The effect of stabilization in finite element methods for the optimal boundary control of the Oseen equations”. In: *Finite Elements in Analysis and Design* 41.3 (2004), pp. 229–251. DOI: https://doi.org/10.1016/j.finel.2004.06.001.

[50] Sá L.F.N. et al. “Topology optimization applied to the development of small scale pump”. In: *Structural and Multidisciplinary Optimization* 57 (2018), pp. 2045–2059. DOI: https://doi.org/10.1007/s00158-018-1966-7.

[51] Aikawa E. *Calcific Aortic Valve Disease*. IntechOpen, June 2013. DOI: 10.5772/46239.

[52] Jansson N. Spühler J. H. Jansson J. and Hoffman J. “3D Fluid-Structure Interaction Simulation of Aortic Valves Using a Unified Continuum ALE FEM Model”. In: *Frontiers in Physiology* 9 (2018). DOI: 10.3389/fphys.2018.00363.

[53] AM Valsalva. “Arteria magnae sinus”. In: *Opera*. Vol. 1. Pitteri Venice, 1740.

[54] Clark R. E. Swanson W. M. “Dimensions and geometric relationships of the human aortic value as a function of pressure”. In: *Circulation Research* 35 (1974), pp. 871–882. DOI: 10.1161/01.RES.35.6.871.

[55] Ose V. P. Kasyanov V. A. Purinya B. A. “Structure and mechanical properties of the human aortic valve”. In: *Circulation Research* 20 (1985), pp. 637–647. DOI: 10.1161/01.RES.35.6.871.